

# Organic Redox-Active Flow Batteries Enabled by Aqueous Ionic Liquid Electrolytes



**UNIVERSITÄT  
DES  
SAARLANDES**

**Dissertation**

zur Erlangung des Grades

des Doktors der Naturwissenschaften

der Naturwissenschaftlich-Technischen Fakultät

der Universität des Saarlandes

von

**Zhifeng Huang**

Saarbrücken, 2020



Tage des Kolloquiums: 09. 09. 2020

Dekan: Prof. Dr. Guido Kickelbick

Berichterstatter: Prof. Dr. Dr. hc. Rolf Hempelmann

Prof. Dr. -Ing. Markus Gallei

Akad. Mitarbeiter: Dr. Haibin Gao

Vorsitz: Prof. Dr. Michael Springborg



---

## Abstract

The supporting electrolytes play a critical role in the electrochemical and thermal stability, solubility, and electrochemical reversibility of redox species. The utilization of aqueous electrolytes is promising for achieving techno-economic targets via advancement in energy density. Herein the attractive “Water-in-Ionic Liquid” aqueous electrolytes system using imidazolium chloride (EMImCl or BMImCl) are explored to extend the temperature stability window and the solubility of organic redox-active species. Water crystallization at subzero temperatures was effectively suppressed in the proposed aqueous electrolytes. The broadening of the electrochemical stability window of the supporting electrolytes enabled the studies of redox metal complexes over a broad temperature range. The organic redox-active species, such as nitroxyl radicals, bipyridinium, and quinones, achieved high solubility and enhanced electrochemical reversibility in the studied aqueous electrolytes with different molalities. The electrochemical performance has been studied with different concentrations of organic species, demonstrating good capacity retention and power density.

---

# Zusammenfassung

Die Leitelektrolyte spielen eine entscheidende Rolle für die elektrochemische und thermische Stabilität, Löslichkeit und elektrochemische Reversibilität von Redoxspezies. Die Verwendung von wässrigen Elektrolyten ist ein primärer Weg, um technoökonomische Ziele durch Verbesserung der Energiedichte zu erreichen. Hier werden attraktive wässrige Elektrolyte unter Verwendung von ionischen Imidazoliumchlorid (EMImCl oder BMImCl) Flüssigkeiten untersucht, um das Temperaturstabilitätsfenster und die Löslichkeit organischer redoxaktiver Spezies zu verbessern. Die Wasserkristallisation bei Temperaturen unter Null wurde in dem vorgeschlagenen wässrigen Elektrolyten wirksam unterdrückt. Die Verbreiterung des elektrochemischen Stabilitätsfensters der Leitelektrolyte ermöglichte die Untersuchung von Redoxmetallkomplexen über einen weiten Temperaturbereich. Die organischen redoxaktiven Spezies wie Nitroxylradikale, Bipyridinium und Chinone erreichten eine hohe Löslichkeit und eine verbesserte elektrochemische Reversibilität wässriger Elektrolyte mit unterschiedlicher Molalität. Die elektrochemische Leistung wurde bei verschiedenen Konzentrationen organischer Spezies untersucht.

---

# Acknowledgments

First and foremost, I would like to express my sincerest gratitude to my supervisor *Prof. Dr. Dr. h.c. Rolf Hempelmann* for giving me this opportunity and support me to perform this work under his supervision in a very active and open mind atmosphere at Universität des Saarlandes and Korea Institute of Science of Technology (KIST) Europe. I would like to also thank my scientific advisor *Prof. Dr. David Scheschkewitz* and *Prof. Dr. Markus Gallei* for their interest and the pleasant scientific discussion during the time of my Ph.D. studies.

I would like to specially thank *Dr. Ruiyong Chen* for his excellent and valuable scientific discussions in all of my works. In addition, I would like to take this opportunity to thank *Prof. Dr. Peng Zhang* (INM, Germany and Sun yat-sen University, China), *Dr. Björn Kuttich* (INM, Germany), *Prof. Dr. Tobias Kraus* (INM, Germany), *Prof. Dr. Christoper W. M. Kay* (Saarland University), *Dr. Daniel Rauber* (Saarland University), *Prof. Dr. Steffano Passerini* (HIU, Germany), *Dr. Xinpei Gao* (HIU, Germany), *Dr. Hongjiao Li* (KIT, Germany) and *Prof. Dr. Dirk Henkensmeier* (Korea University, Republic of Korea) for their great collaboration and contributions to the work in this dissertation.

I would like to express my thanks to *Dr. Sangwon Kim* for his kind and friendly

---

support. Thanks to all the past and current colleagues from Transfercenter Sustainable Electrochemistry (TSE) lab such as *Dr. Jaeho Lee, Sangjun Yoon, Galina Skorikova, Ammar Tatlisu, Dr. Jan Geiser, Dr. Dan Durneata* for all the fruitful discussions about science and life. Further thanks to my colleagues from the Korea Institute of Science and Technology (KIST) Europe.

I also would like to thank China Scholarship Council for providing me financial support.

Lastly but also the most important, I would like to thank the support from my parents. Very special gratitude to my dear wife (*Lu Yu*) and our lovely daughter (*Jiayu Huang*) for their great love, continuous support, and uncountable contribution to our small family.

---

“The scholar becomes proficient through deliberate thought, but suffers from causal imitation.”

—Han, Yu

---

## Table of contents

Abstract.....	I
Zusammenfassung.....	II
Acknowledgments.....	III
Table of contents .....	VI
1. Introduction .....	1
2. Fundamentals.....	4
2.1 Basic principles of redox flow batteries .....	4
2.1.1 Construction and components of RFBs .....	4
2.1.2 Thermodynamics and kinetics of batteries .....	6
2.1.3 Electrochemical thermodynamics.....	7
2.1.4 The assessment of electrochemical performance.....	10
2.2 Redox-active materials from metal ions to organic species .....	12
2.3 Electrolytes for organic redox-active RFBs .....	15
2.3.1 Conventional electrolytes in RFBs .....	15
2.3.2 Ionic liquids based electrolytes.....	20
2.4 Objectives and scope of the presented work .....	23
3. Experimental methods and operations .....	24
3.1 Materials characterization techniques .....	24
3.1.1 Differential scanning calorimetry (DSC).....	24
3.1.2 Small Angle X-ray Scattering (SAXS) .....	26
3.1.3 Electron paramagnetic resonance (EPR) spectroscopy .....	27
3.1.4 Ionic conductivity measurements .....	29
3.1.5 Rheological properties measurements .....	30
3.2 Electrochemical techniques .....	30

---

3.2.1	Cyclic voltammetry (CV) .....	30
3.2.2	Rotating disk electrode (RDE) technique .....	32
3.2.3	Electrochemical impedance spectroscopy (EIS) .....	33
3.2.4	Galvanostatic cycling.....	35
3.3	Electrolytes and cell preparation .....	37
3.3.1	Preparation of supporting electrolytes .....	37
3.3.2	Solubility test of redox-active species .....	37
3.3.3	Preparation of redox-active electrolytes .....	38
3.3.4	Pre-treatment of graphite felt.....	38
3.3.5	Pre-treatment of ion exchange membrane .....	38
3.3.6	Preparation of flow cell .....	39
4.	Results and discussions .....	40
4.1	Physicochemical properties of water-in-ionic liquids electrolytes.....	40
4.2	Aqueous ionic liquid electrolytes for all-climate RFB application.....	46
4.2.1	Motivations .....	46
4.2.2	Thermophysical properties of supporting electrolytes.....	47
4.2.3	Electrochemical stability at wide temperature ranges .....	54
4.2.4	Long-term performance of electrolytes at room temperature.....	58
4.2.5	Long term cycling performance at robust temperatures .....	63
4.3	Aqueous ionic liquid electrolytes for all organic RFB.....	69
4.3.1	Motivation.....	69
4.3.2	Solubility of redox-active electrolytes.....	70
4.3.3	EPR analysis of the interaction mechanism.....	74
4.3.4	Electrochemical properties of electrolytes.....	76
4.3.5	Long-term stability with multi-electron transition reaction.....	79
4.3.6	Long-term stability in high concentration .....	86

---

4.4	Aqueous ionic liquid electrolytes for quinone-based RFB .....	94
4.4.1	Motivations .....	94
4.4.2	Solubility of quinones in aqueous ionic liquid electrolytes .....	95
4.4.3	Electrochemical properties of quinones .....	96
4.4.4	Long-term performance of quinone-based redox electrolytes .....	103
5.	Conclusion and outlook .....	106
	Materials and chemicals .....	109
	Abbreviations .....	111
	Publications and conferences .....	113
	Patent .....	113
	Book Chapter .....	113
	Publications .....	113
	Conferences .....	114
	Erklärung .....	115
	Bibliography .....	116

---

# 1. Introduction

Owing to the increasing energy consumption of fossil fuels, a severe environmental deterioration and issues of limiting resource reserving have impelled human beings to develop more carbon-neutral renewable energy resources.<sup>1-2</sup> Natural resources such as solar power, wind power, and biofuels, have drawn sustainable attention as effective alternatives to fossil fuels. Nevertheless, the inherent fluctuation of nature is a great challenge for electric power operating. Naturally, the increasingly efficient use of renewable energy resources requires advanced energy storage systems to regulate electricity storage and distribution. Up to now, various types of technologies such as flywheels, pumped hydropower plants, and electrochemical energy storage devices are applied depending on the requirement of discharge time and power values (Figure 1.1).<sup>1-5</sup> Among them, electrochemical energy storage devices depending on repetitive conversion between electric and chemical energy are promising technologies for stabilizing renewable energy. In particular, battery technologies such as lead-acid, lithium-ion, and flow batteries have been rapidly developed and have reshaped our lives.

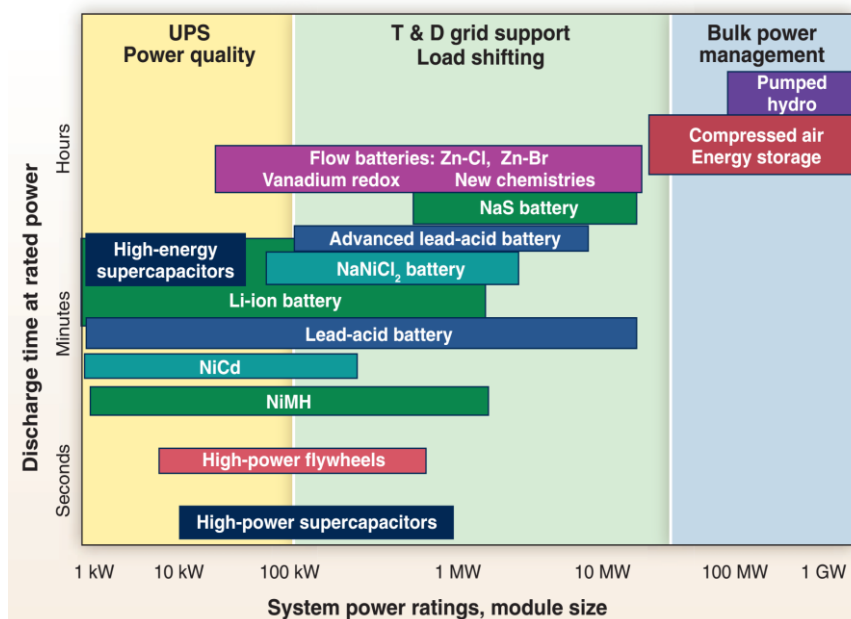


Figure 1.1 Comparison of discharge time and power rating for various electrical energy storage technologies. Reprinted with permission from reference [4]. Copyright 2011 Science publishing group.

Lead-acid batteries, invented in 1895, are the oldest and most widely used rechargeable electrochemical devices in our daily life.<sup>6</sup> Nevertheless, it suffers from short cycle life (500-1000 cycles) and low energy density ( $30\text{-}50\text{ Wh kg}^{-1}$ ) due to the gradual consumption of sulfuric acid and the inherent high-density lead. Since the first commercialization by Sony in the early 1990s, lithium-ion batteries (LIBs) have become a dominating power system for the portable electronic apparatus and vehicles because of their high energy densities ( $200\text{-}400\text{ Wh kg}^{-1}$ ) and long-term stability.<sup>7</sup> Notably, the Nobel Prize in Chemistry in 2019 was awarded to Prof. John B. Goodenough, Prof. M. Stanley Whittingham, and Prof. Akira Yoshino in recognition of their contributions “for the development of lithium-ion batteries”.<sup>8</sup> Despite the high energy densities, the intrinsic constrictions from the intercalation mechanism and safety

concerns from organic solvents explosion became a crucial defect for their comprehensive implementations.<sup>9-10</sup>

Unlike the use of solid-state materials in LIBs, the redox flow batteries (RFBs) mainly using redox-active liquids are considered as a reliable stationary technology that can compensate for the energy fluctuation in solar and wind power.<sup>2</sup> By storing dissolved electroactive materials in external tanks, the RFB decouples energy and power thus gaining merits such as flexible scalability, easy thermal management, and low environmental impact.<sup>11-12</sup> Thereby, the RFBs with low-cost, high energy densities, long life, and good climate adaptability should be explored. Apart from molecular engineering, in this thesis, the electrolyte optimization method based on aqueous ionic liquids supporting electrolytes was studied. The electrochemical performance of organic/organometallic species was investigated in the proposed electrolytes to broaden the operating temperature range and boost the energy density of aqueous RFBs.

---

## 2. Fundamentals

The rechargeable batteries are devices that can repeat the conversion between chemical and electrical energy for hundreds or even thousands of charging and discharging processes.<sup>13</sup> RFB, mainly using liquid redox couples, is a proper technique for large-scale stationary storage systems. In this section, the development and existing challenges of RFBs are briefly introduced.

### 2.1 Basic principles of redox flow batteries

#### 2.1.1 Construction and components of RFBs

A typical RFB configuration consists of three main components, including cell stack, exterior tanks, and circulating pipes, as shown in Figure 2.1a. The cell stack is the core part where the chemical reactions take place, once the electrolytes are pumped through the porous electrode (Figure 2.1b). During the fluids cycling, the oxidized and reduced redox couples on the electrode are recycled to the external tanks, and charge-balancing ions are transported through the membrane. The unique architecture enables independent power and energy output of RFB regarding the reactive area of cell stack and the size of the tanks, respectively.

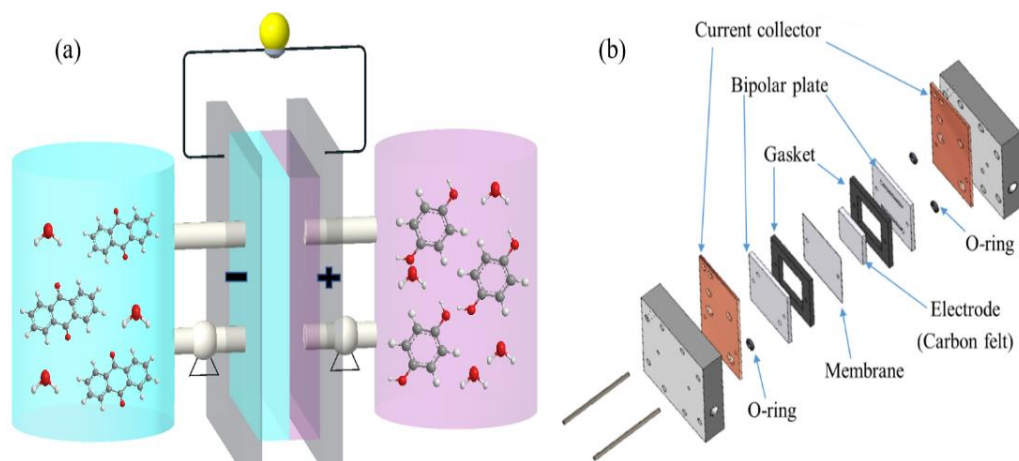


Figure 2.1 (a) Schematic illustration of redox flow battery configuration and (b) the corresponding construction of the reaction cell.

As illustrated in Figure 2.2, redox electrolytes play a pivotal role in regulating the performance of RFBs. Redox-active species with high solubility and working voltage are able to achieve high energy density. Supporting electrolytes consisting of the solvent and supporting salts or conductive ions enable ion transportation. The supporting electrolytes with wide electrochemical stability window (ESW) and high thermal stability can effectively enlarge the options of electroactive materials and the temperature adaptability of RFBs. In addition, a membrane possesses features of high selectivity, ionic conductivity, chemical stability that can not only promote the electrochemical performance but also prolong the cycle life of the cell. Given that the redox reactions of electroactive materials take place on the surface of electrodes, the performance is also affected by the structure of the electrode. Generally speaking, the electrodes maintaining high electrical conductivity and large surfaces are highly preferred.

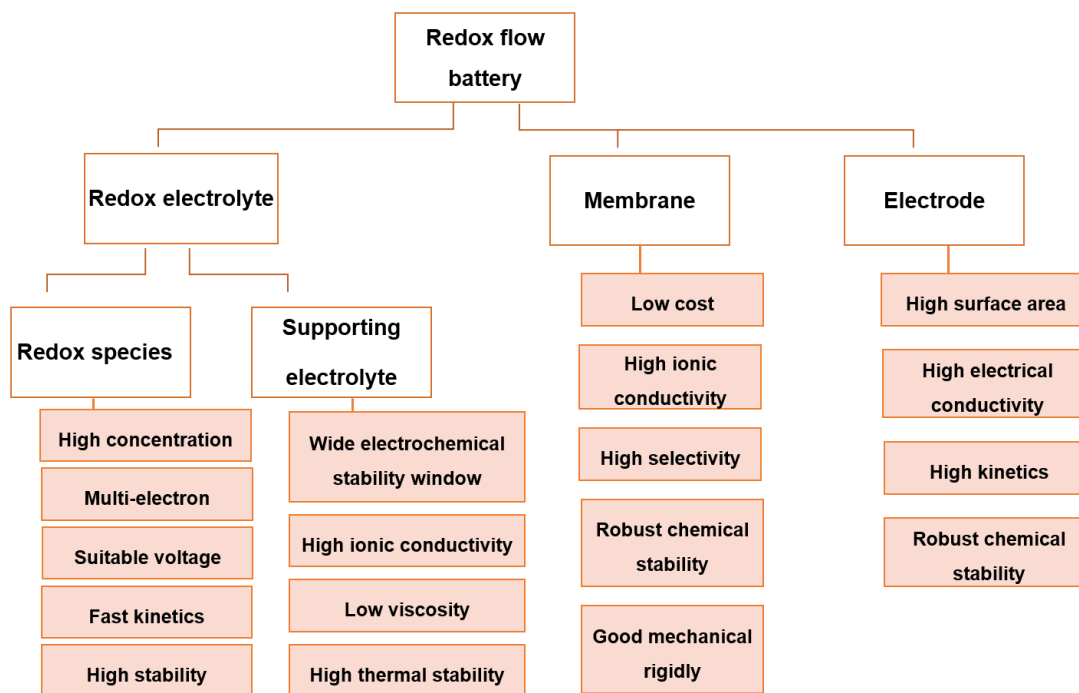
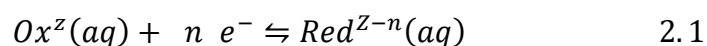


Figure 2.2 Design principle of flow battery in terms of different components, including redox electrolyte, membrane, and electrode.

### 2.1.2 Thermodynamics and kinetics of batteries

Herein, the fundamentals of electrochemistry are discussed to provide an interpretation of the electrochemical methods used in this thesis. For general electrochemical reaction, the following heterogeneous electron transfer at the electrode-solution interface is assumed in Equation 2.1,



where  $Ox^z$  and  $Red^{z-n}$  are the oxidized and reduced redox-active species in the solution.

### 2.1.3 Electrochemical thermodynamics

At standard temperature and pressure (298 K, 1 bar), the standard reduction potential ( $E^0$ ) for the cell reaction is associated with the standard Gibbs free energy, according to Equation 2.2,

$$-\Delta G^0 = nFE^0 \quad 2.2$$

where  $-\Delta G^0$  represents the change in Gibbs free energy under standard conditions,  $F$  is related to the Faraday constant (96485 C mol<sup>-1</sup>), and  $n$  is regarded as the stoichiometric number of transfer electrons in the reaction.

In consideration with the concentration changes of species in the practical electrolyte environment, the available relationship between overall potential ( $E$ ) of the electrochemical cell and concentrations of the redox-active species can be stated by the *Nernst equation* (Equation 2.3),

$$E = E^0 + \frac{RT}{nF} \ln \left( \frac{C_{Ox^z}}{C_{Red^{z-n}}} \right) \quad 2.3$$

where  $E^0$  is the formal standard electrode potential against the standard hydrogen electrode at the unity activity of redox-active species.

The *Nernst equation* describes the electrochemical thermodynamics of the system while it does not give insight into how fast these reactions occur. Figure 2.3 gives a schematic illustration of the mass transfer of reactants from the bulk solution to electrode and electron transfer behavior at the electrode-electrolyte interface. The diffusion coefficient ( $D_i$ ) relating to the mass transport limitation and electron transfer

rate constant ( $k_0$ ) representing the charge transfer reactions at the electrode interface are essential parameters to quantify the electrochemical kinetics of redox-active species in the reaction system.

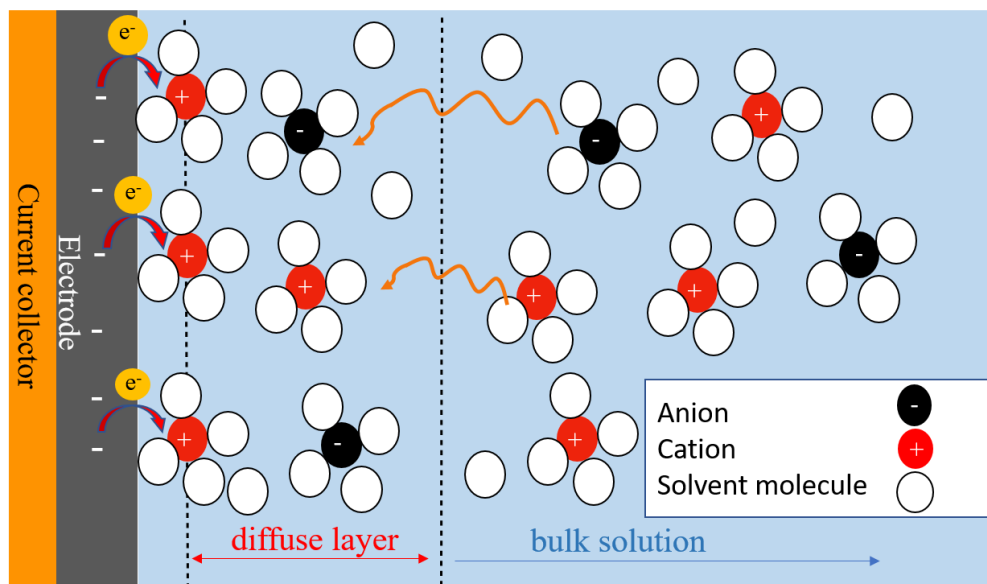


Figure 2.3 Schematic illustration of the mass transfer of reactants from the bulk solution to electrode and electron transfer behavior at the electrode-electrolyte interface.

In general, the simple case of a single-electron transfer reaction in Equation 2.1 is given to express the heterogeneous reactions at the electrode-electrolyte interface. The number of transfer charges can be expressed by Faraday's Law (Equation 2.4), wherein the reaction rate ( $v_r$ ) shows a proportional relationship with faradic current ( $I$ ) as described in Equation 2.5,

$$\frac{Q}{nF} = \frac{It}{nF} = N \quad 2.4$$

$$v_r = \frac{dN}{Adt} = \frac{I}{nFA} = \frac{j}{nF} \quad 2.5$$

where  $Q$  is the charge (C),  $F$  is Faraday constant,  $n$  is the stoichiometric number of

transfer electrons,  $N$  is the molar amount of the redox-active materials (mol),  $I$  is the current (A),  $t$  is the reaction time (s),  $v_r$  is the reaction rate ( $\text{mol s}^{-1} \text{cm}^{-2}$ ), and  $j$  is the current density ( $\text{A cm}^{-2}$ ) that commonly used to describe the flowing current at the electrode-electrolyte interface in electrochemistry.

Once the reactant species reach the electrode surface, the net reaction rate ( $v_{net}$ ) is determined by the rate difference for forward and backward reaction depending on the reaction rate constant ( $k_{ox}$ ,  $k_{red}$ ) and the surface concentration ( $C_{ox,0}$ ,  $C_{red,0}$ ) of the reactive species on the electrode surface, as expressed in Equation 2.6.

$$v_{net} = v_{ox} - v_{red} = \frac{j}{nF} = k_{ox,0}C_{ox,0} - k_{red,0}C_{red,0} \quad 2.6$$

According to the *Arrhenius equation* (Equation 2.7), the reaction rate constants ( $k_0$ ) is given by

$$k_0 = A_0 \cdot \exp \frac{-\Delta G_a}{RT} \quad 2.7$$

Where  $A_0$  represents a frequency factor,  $\Delta G_a$  is the standard Gibbs energy of activation for the reaction.

When an external potential ( $E'$ ) is applied to the electrode system, the electrochemical reaction will drive out of equilibrium state ( $E_{eq}$ ), leading to a change of the Gibbs free energy of activation. The difference between the electrode potential and the equilibrium potential is known as overpotential  $\eta$  (Equation 2.8):

$$\eta = E_{eq} - E' \quad 2.8$$

Accordingly, the rate constant is changed in each half-reaction. Therefore, the

expression in Equation 2.6 can be interpreted by the *Bulter-Volmer equation* (Equation 2.9), which describes how the current density depends on the electrode potentials.

$$j = j_0 \left[ \exp\left(\frac{-\alpha F \eta}{RT}\right) - \exp\left(\frac{(1-\alpha) F \eta}{RT}\right) \right] \quad 2.9$$

Where  $j_0$  is the exchange current density.

#### 2.1.4 The assessment of electrochemical performance

The electrochemical performance of the battery is affected by many factors and can be measured by the following benchmarks. The theoretical energy density of a full cell is the product of its voltage and its capacity (Equation 2.10). Thus, the energy density is dependent on the amount of redox-active materials, working potential, and the number of electrons that participate in the redox process.

$$\text{Energy density} = nCFE \quad 2.10$$

Where  $n$  is the electron transfer number in the cell reaction,  $C$  is the concentration of the redox-active species ( $\text{mol L}^{-1}$ ),  $F$  is the Faradic constant,  $E$  is the output voltage (V).

The areal power density represents how quickly the battery can deliver energy, as expressed in Equation 2.11. In the RFB system, it is mainly affected by the reaction kinetics of redox species, operating current densities, electrolyte conductivities, and flow rates.

$$\text{Power density} = \frac{I \cdot V}{A} \quad 2.11$$

The capacity utilization efficiency, Coulombic efficiency (CE), voltage efficiency (VE), and energy efficiency (EE) are essential criteria for the electrochemical quality of the RFB. Capacity utilization efficiency indicates how much capacity is realized as compared to theoretical capacity at a given testing concentration. CE relates to the charge transfer ratio in the same charge/discharge cycle (Equation 2.12). In practical tests, the CE is less than 100%, which may be caused by the undesirable crossover of solvent and electroactive species through the ion-exchange membrane, irreversible side reactions in solution, and degradation of various cell components.<sup>14</sup> The VE (Equation 2.13) is defined as the ratio of the averaged discharge voltage to charge voltage. At any particular current density, the voltage efficiency is affected by a variety of overpotentials, including kinetic, ohmic, and transport loss. The VE decreases as the current density increases.

$$CE = \frac{\int I_{dis} dt}{\int I_{ch} dt} \times 100\% = \frac{Q_D}{Q_C} \times 100\% \quad 2.12$$

$$VE = \frac{E_{dis}^{cell}}{E_{ch}^{cell}} \times 100\% \quad 2.13$$

$$EE = CE \times VE \quad 2.14$$

Where the  $I_{dis}$  and  $I_{ch}$  represent the applying current during discharging and charging, respectively.  $E_{dis}^{cell}$  and  $E_{ch}^{cell}$  represent the average cell voltage during discharging and charging, respectively. EE is expressed as a multiplication of columbic efficiency and voltage efficiency in Equation (2.14), representing the percentage of output and incoming energy. Typical EE values of RFBs are in the range of 50 to 90 %, depending on the applied current density and materials properties.

The State of Charge (SOC), in association with the change of ion concentration, is usually mentioned to evaluate cell performance. In the half-reaction system, as illustrated in Equation 2.1, the SOC can be defined by the changes of  $\text{Red}^{Z-n}$ , as given in Equation 2.15.

$$SOC = \frac{\text{Red}^{Z-n}}{O^{Z-n} + \text{Red}^{Z-n}} \times 100\% \quad 2.15$$

$$E = E^0 + \frac{2RT}{nF} \ln \frac{SOC}{1-SOC} \quad 2.16$$

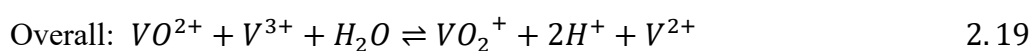
Thus, the open cell voltage (OCV) is equal to  $E^0$  when the cell is operated at 50% SOC according to the expression in Equation 2.16.

## 2.2 Redox-active materials from metal ions to organic species

The redox-active materials in a RFB are the most critical components because they are the principal redox materials, and their properties largely determine the overall battery performance and cost of RFBs system.

Currently, most of RFBs rely on inorganic metal-based materials. Since the first modern prototype concept of flow battery has been patented by Kangro in 1949<sup>15</sup>, metal-based redox couples such as Fe/Cr,<sup>16</sup> Fe/V,<sup>17</sup> and Zn/Br,<sup>18</sup> have been investigated in aqueous RFBs. However, the formation of metal dendrites, gas evolution of reactants, and cross-contamination of redox-active species resulted in poor cycle life, hindering their further commercialization. Vanadium redox flow battery (VRFB), using the same redox species, effectively mitigates the capacity decay from cross-mixing and yield high efficiency and long life calendar. The redox electrolyte is typically composed of

1.5-2.0 M vanadium ions in 2.0-4.0 M H<sub>2</sub>SO<sub>4</sub> solution, giving a volumetric energy density of 30-50 Wh L<sup>-1</sup>.<sup>12, 19-26</sup> The overall electrochemical reaction gives a cell voltage of 1.26 V vs. SHE at 25 °C via changes in the vanadium valence state through the reactions in Equation 2.17-2.19.



Nevertheless, the expensive components (ca. \$ 26 per kg vanadium raw materials, and \$ 500 per m<sup>2</sup> for Nafion membrane) results in a high system cost (300-500 \$ per kWh) of the cell,<sup>2, 27-29</sup> which are remaining critical challenges for their widespread penetration in electrochemical energy storage (EES) system.

Recently, RFBs using organic/organometallic redox-active compounds are mostly concerned with decreasing system costs and tunable properties based on the structure and electrochemical properties. Since many electroactive organic materials can be obtained from abundant natural resources, the capital costs approaching to \$150 per kWh has been claimed in a few organic RFBs, which is much lower than the cost of VRFB (Table 2-1).<sup>30-31</sup>

Table 2–1 The cost comparison of a 4 MWh/1 MW system for metal-based and the redox-active organics in RFBs. (MV: Methyl viologen, FcNCl: (ferrocenylmethyl)trimethylammonium chloride, 4-HO-TEMPO: 4-hydroxyl-2,2,6,6-tetramethylpiperidine 1-oxyl).

Redox species	Membrane	Supporting electrolyte	Total capital cost / \$ kWh <sup>-1</sup>
Department of Energy Office's target <sup>32</sup>			150
V/V <sup>27</sup>	Nafion	H <sub>2</sub> SO <sub>4</sub>	325
Fe/V <sup>27</sup>	Nafion	H <sub>2</sub> SO <sub>4</sub>	595
Anthraquinone / Br <sub>2</sub> <sup>30</sup>	Nafion 212	H <sub>2</sub> SO <sub>4</sub>	165
MV/FcNCl <sup>33</sup>	Selecion	NaCl	162
MV/4-HO-TEMPO <sup>31</sup>	Selecion	NaCl	178

On the hand, the chemical reaction based on redox-active organic materials shows a veritable variability of redox potential, electron-transfer number, and chemical stability depending on supporting electrolyte.<sup>34-37</sup> Innovative works have been demonstrated over the past years with the application of quinones,<sup>30, 38</sup> nitroxide radicals,<sup>39</sup> viologens,<sup>40</sup> and metallocenes,<sup>41-42</sup> for example (Figure 2.4). For instance, the benzoquinone undergoes a two-electron and two-proton process in the protic solution, (e. g. quinones in Figure 2.4). It delivers double electron concentration capability as compared to one-electron transition in most of the metal-based materials. Therefore, the organic molecules can not only enrich the diversity of electroactive

materials but also empower the electrochemical/chemical properties of redox electrolytes.

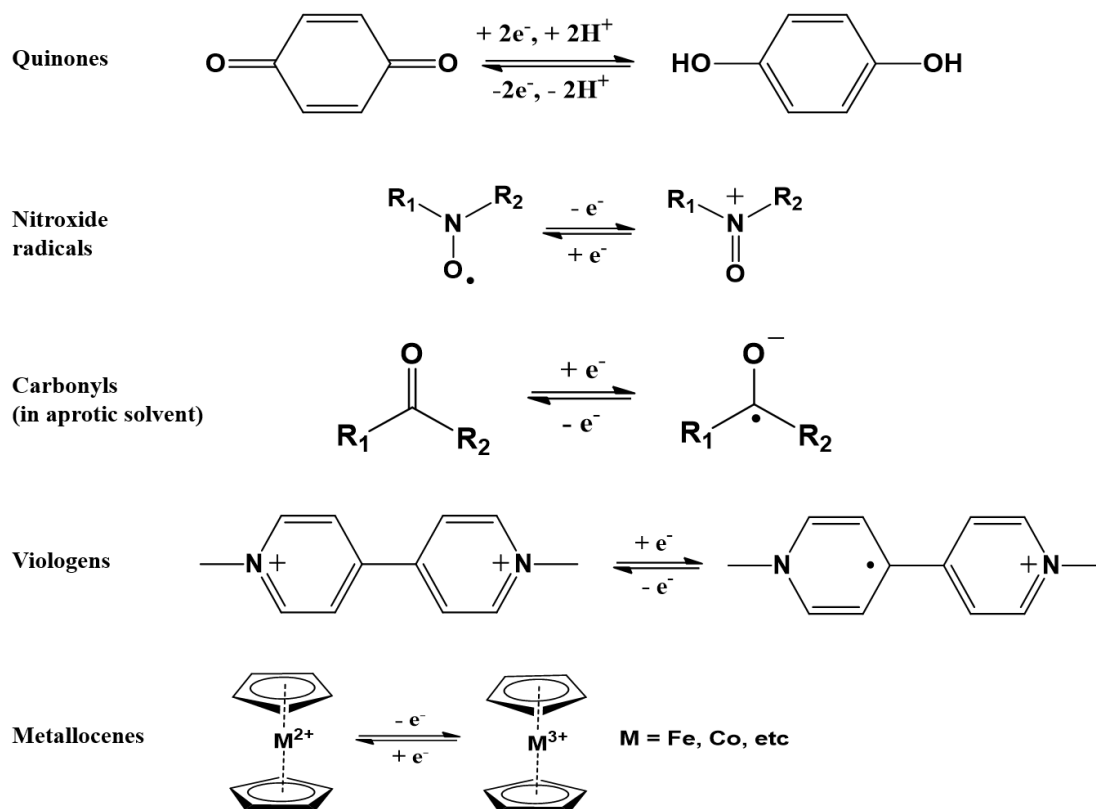


Figure 2.4 Electrochemical reactions mechanism of some representative redox-active organic materials used in RFBs.

## 2.3 Electrolytes for organic redox-active RFBs

### 2.3.1 Conventional electrolytes in RFBs

The most notable RFBs are dependent on aqueous electrolytes because of their advantages of high ionic conductivity, and highly safe operations. For instance, 1 M

NaCl, KOH, and H<sub>2</sub>SO<sub>4</sub> show a high ionic conductivity of 86, 209, and 395 mS cm<sup>-1</sup>, respectively.<sup>37</sup> The RFBs employing electrolytes with high ionic conductivity offer the possibility for realizing a high charge/discharge performance, high energy efficiencies, and high power densities.<sup>30, 38</sup> In neutral NaCl solution, N,N,N,N-2,2,6,6-heptatetramethylpiperidiny-1-oxyl (TEMPTMA)/4,4-dimethyl bipyridinium dichloride (MV) RFB was able to perform under high current densities between 20-200 mA cm<sup>-2</sup>,<sup>40</sup> which is one magnitude higher than that in non-aqueous electrolytes conditions.<sup>39, 43</sup> Meanwhile, the 9,10-anthraquinone-2,7-disulphonic acid (AQDS) and Br<sub>2</sub>/Br<sup>-</sup> redox couple yielded a high peak power density of 0.6 W cm<sup>-2</sup> at 90% state-of-charge owing to rapid electron transfer kinetics, high ionic conductivity of H<sub>2</sub>SO<sub>4</sub> supporting electrolytes and a highly conducting ion exchange membrane.<sup>30</sup> Despite the remarkable achievements of water-based RFBs, the final energy density are limited by the narrow operation potential (< 1.5 V) with respect to hydrogen and oxygen evolution.

In order to expand the potential range, organic solvents with a wide potential window (> 4.0 V) have been adapted to potentially enlarge the energy density of RFBs.<sup>44-45</sup> Since the first investigation on the electrochemical behavior of Tris(bipyridine)ruthenium(II) ([Ru(bpy)<sub>3</sub>]<sup>2+</sup>) in 1988,<sup>46</sup> high open-circuit voltage approaching 3.5 V have been achieved in symmetric and hybrid cells.<sup>39, 46-49</sup> However, a sluggish kinetic was experienced in non-aqueous electrolytes due to the relatively low ionic conductivity.<sup>44</sup> More seriously, the metallic (e.g. lithium, zinc) dendrites were inevitably formed over charging/discharging cycles, leading to shorter cycling life and possible explosion of the flammable organic solvents by short-circuiting.<sup>39, 50</sup>

For the use of organic materials, one of the main concerns remains the solubility

of organic species in the supporting electrolytes. The low solubility of redox organic materials dramatically affect the total energy density of RFBs. As shown in Figure 2.5, quinones derivatives (i.g. benzoquinones and anthraquinone), which are widely studied as electroactive materials, generally have low solubility (c.a. 0.1 M) in water.<sup>51</sup> In non-aqueous solvents, most of the organic molecules show a solubility lower than 1.0 M. Up to now, Methyl viologen and 4-OH-TEMPO have high solubility (2-3 M) in water, while such high solubility decreases with increasing supporting salts. With the increased concentration of NaCl from 0.3 to 3 M, the solubility of an ammonium-grafted TEMPO decreases from 3.2 M to 1.2 M (right green bar in Figure 2.5)<sup>40</sup>.

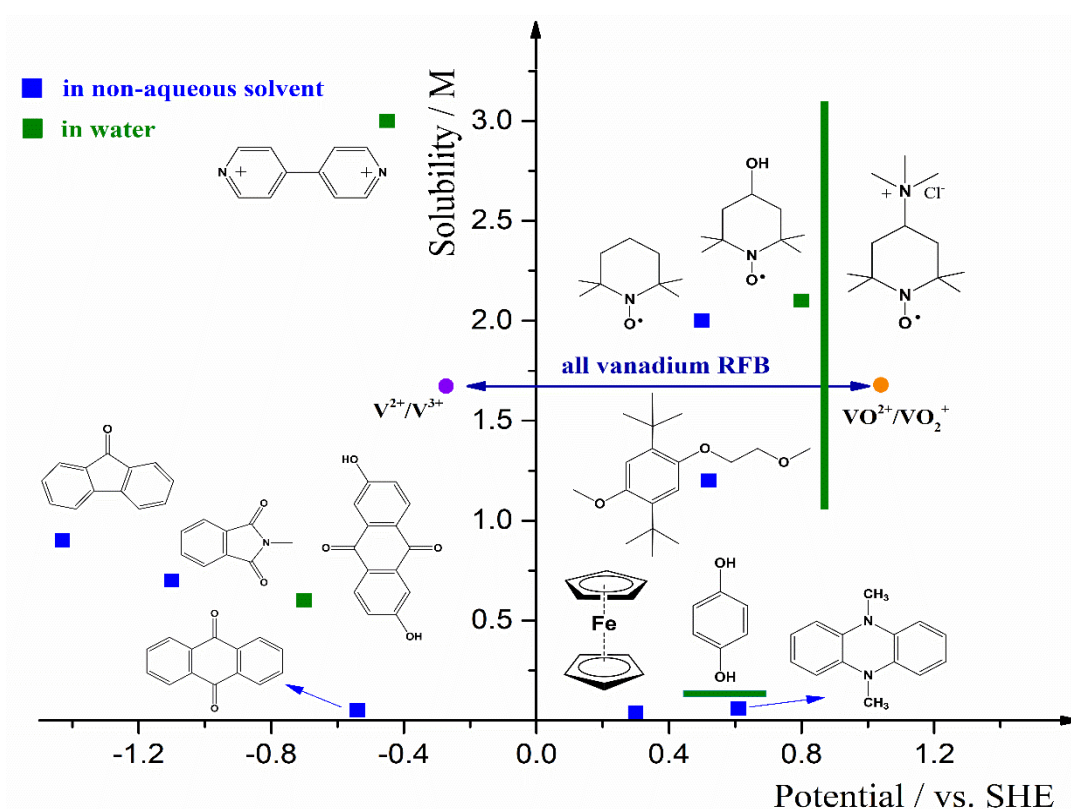
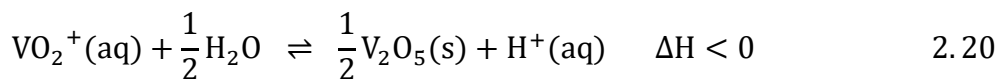


Figure 2.5 Redox potential and solubility of representative organometallic/organic materials in aqueous and non-aqueous supporting electrolytes for flow batteries. Data obtained from ref. [42,

51-56].

Apart from the solubility of the organic compounds, their reduced or oxidized counterparts need also be examined. It is noteworthy that the reported RFB tests were mostly carried out with low concentrations of  $MV^{2+}$ . The second electron transfer from  $MV^{+•}$  to neutral hydrophilic MV may cause precipitation and hydrogen evolution at higher concentrations.<sup>57</sup> Although higher concentration electrolytes have been prepared via molecular engineering or novel electrolyte design (such as semi-solid,<sup>58</sup> polymers,<sup>36</sup> and eutectic liquid<sup>59</sup>), the high viscous electrolyte results in high overpotential and low energy efficiency (<60%).<sup>39, 60</sup> Therefore, proper design of redox-active materials and optimization of supporting electrolytes are recommended to boost the energy and power density of RFBs.

Another important issue for RFB applications is the temperature range at which they are liquid. Water electrolytes typically exhibit undesirable bulk behavior (i.g. icing) at temperature below 0 °C.<sup>61</sup> To expand the operational temperature range of batteries, many efforts have been studied on modifying the electrolyte formulations, such as the utilization of mixed electrolyte,<sup>62</sup> concentrated electrolytes,<sup>63-64</sup> and electrolytes additives.<sup>65-67</sup> But the temperature is still not enough for the operation of RFBs in cold regions. Although 2 M  $H_2SO_4$  has a freezing point of about -13 °C,<sup>68</sup> it can hardly inhibit the precipitations of  $V^{3+}$  and  $V^{2+}$  at a temperature below -5 °C.<sup>21</sup> On the other hand, the  $VO_2^+$  catholyte can also easily precipitate out at temperatures above 40 °C (Equation 2.20).<sup>23, 66, 69</sup> Accordingly, the electrolyte temperature should be controlled and monitored in a narrow range between 10 and 40 °C during operation.<sup>23</sup>



In contrast, non-aqueous electrolytes normally possess a low freezing point and an elevated boiling point. Recently, the battery using the electrolyte such as LiTFSI/EA,<sup>70</sup> LiFSI/EA/DCM,<sup>71</sup> and TBAPClO<sub>4</sub>/DCM<sup>72</sup> showed excellent thermal stability, which is free of crystallization at low temperature (Figure 2.6). More interestingly, a LiTFSI-methoxy-TEMPO mixture showed a supercooled liquid feature even at low temperature of -70 °C,<sup>73</sup> which is lower than the melting point (*T<sub>m</sub>*) of the individual component due to the decreased lattice energy.<sup>74</sup> However, the newly reported organic flow battery operating at temperatures below -40 °C showed poor energy efficiency of below 30% at low current density of 1 mA cm<sup>-2</sup> due to the low ionic conductivity of the electrolyte.<sup>72</sup> In addition, the solvate mixture possessed a high viscosity, thus additional diluting solvents were required to facilitate the mobility of the ions while reducing the effective molar concentration of active materials.<sup>73, 75</sup>

Since for the conventional redox electrolytes it is difficult to combine optimal energy and power density and the requirements for wide range of temperature applications, novel electrolytes that can simultaneously overcome those bottlenecks are highly demanded.

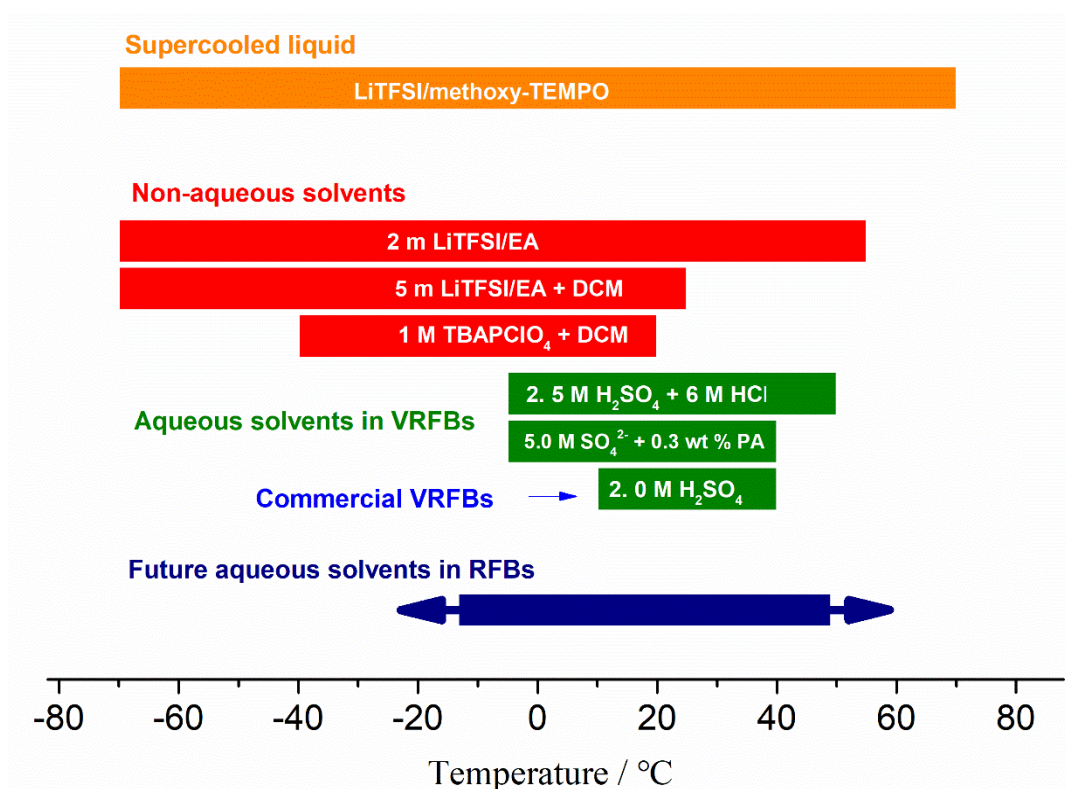


Figure 2.6 Thermal stability of representative electrolytes studied for wide-temperature conditions. EA: Ethyl acetate, DCM: Dichloromethane, and PA: polyacrylic acid.

### 2.3.2 Ionic liquids based electrolytes

Considering the strong dissolving capability, for instance to the conventional insoluble lignocellulose (~30-40 wt%),<sup>76-78</sup> the wide ESW (up to 6.0 V vs. SHE<sup>79</sup>), and the excellent thermal stability,<sup>80</sup> using ionic liquid-based electrolytes are considered as an alternative approach to elevate the electrochemical performance of organic RFBs.<sup>79,</sup>

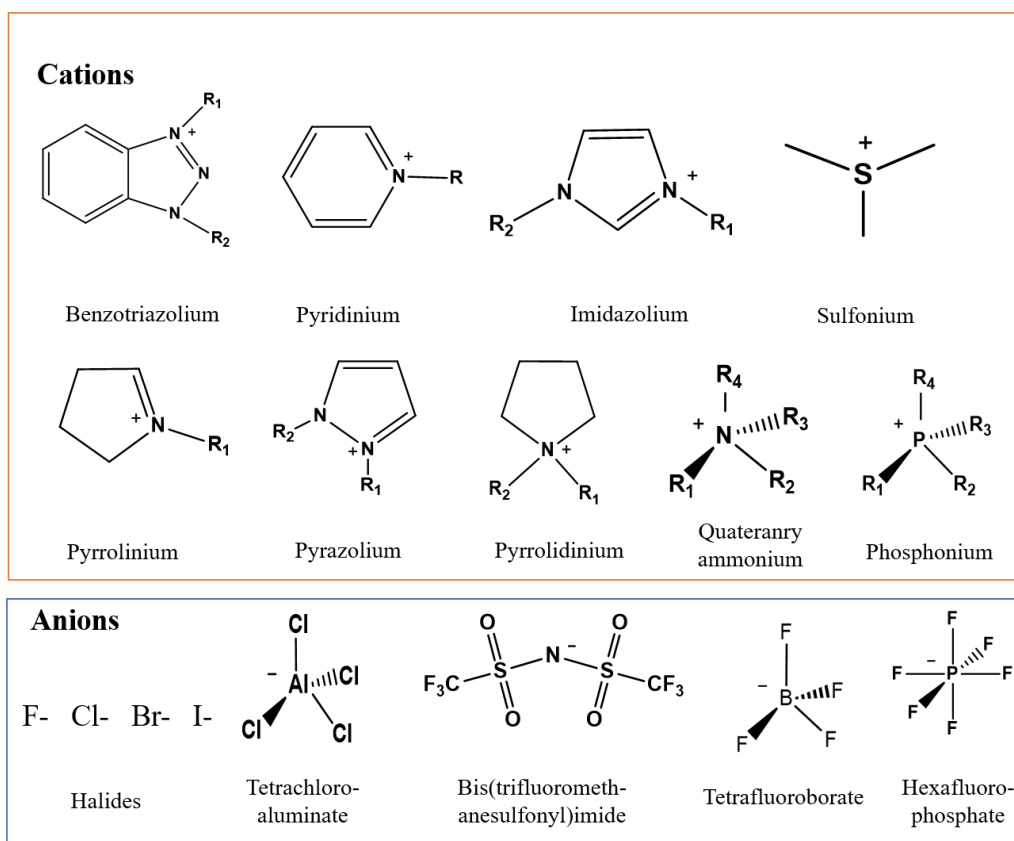


Figure 2.7 Chemical structures of some representative ionic liquids.

Ionic liquids, recognized as molten salts with melting points below 100 °C, possess low volatility, high thermal stability, and often non-flammability.<sup>82, 84-86</sup> By modifying the chemical structure of constituent ions (Figure 2.7), the ionic liquids exhibit versatile physicochemical and electrochemical properties for given applications.

In RFB research, the use of ionic liquids has been studied as either redox-active materials<sup>87-88</sup> or solvate liquids.<sup>75, 80, 89-94</sup> Owing to the comparative high viscosities (30-50 mPas<sup>95</sup>) as compared to conventional solvents like water (0.890 mPas, at 25 °C) and ethylene glycol (16.1 mPas) at room temperature, additional solvents (e.g. water or acetonitrile) are suggested to improve the viscosity and thereof save the pump energy consumptions<sup>95-96</sup> Interestingly, the concept of “water-in-salts” electrolytes with around

17 wt %-25 wt % water achieved a wide ESW ( $\sim 3.0$ - $5.0$  V), which is an extraordinary breakthrough for aqueous electrolytes.<sup>97-99</sup> Especially, an aqueous mixture of LiTFSI-methoxy-TEMPO mixture and water (17 wt %) maintains a stable supercooled liquid phase down to  $-50$  °C.<sup>73, 100</sup> Although the inhibition of water crystallization at such a low temperature provides a favorable potential for designing temperature-adaptive aqueous electrolytes, the climate-adaptive organic redox-active flow battery based on aqueous electrolytes have not been reported yet.

Concerning the operation priority of energy and power densities, the development of novel ionic liquid-based aqueous electrolytes to circumvent the temperature limitations and increase the energy density of organic flow batteries is highly anticipated (Figure 2.8).

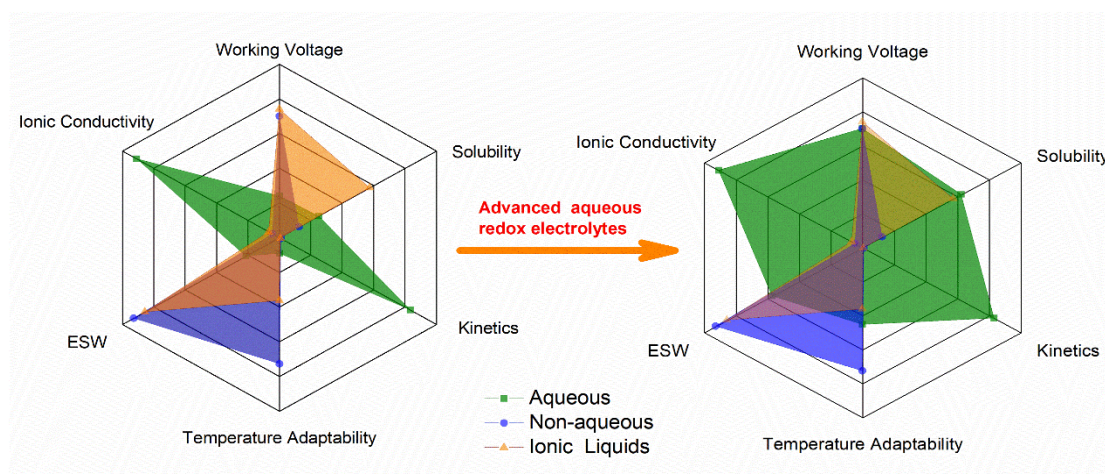


Figure 2.8 Spider chart comparison of redox electrolytes for flow battery. Future aqueous redox electrolytes with high solubility and temperature adaptability (green section) are suggested.

## 2.4 Objectives and scope of the presented work

The objective of the present work was to study and optimize proper aqueous electrolytes for climate-independent and energy-rich organic redox-active flow batteries. Specifically, imidazolium chloride-based “Water-in-Ionic Liquids” (aq-ILs) were searched. Therefore, the crucial criteria of electrolytes in terms of thermal and electrochemical stability, as well as dissolving capability of redox species, were examined to assess the feasibility. The electrochemical performance of redox organic species was tested under realistic battery experiments in aq-ILs. A set of electrochemical cell design was developed for conducting battery studies at wide temperature ranges in Chapter 4.2. In Chapter 4.3, the organic species with enhanced solubility and electrochemical reversibility were identified and characterized. At last, quinones derivatives were targeted in Chapter 4.4 due to the demonstrated high solubility in the studied aq-ILs.

---

## 3. Experimental methods and operations

In this section, the working principles of some typical techniques that are used to realize this work are briefly explained. Those existing experimental methods manifest properties of materials ranging from physicochemical to electrochemical features.

### 3.1 Materials characterization techniques

#### 3.1.1 Differential scanning calorimetry (DSC)

The differential scanning calorimetry (DSC) is one of the most effective methods for measuring the transition temperature correlated to the enthalpy of phase transitions. The thermodynamic characterizations such as glass-transition, crystallization, melting, and freezing temperatures are commonly displayed in the DSC curve. As illustrated with the example of EMIMCl in Figure 3.1, the  $T_m$  is regarded as the onset of an endothermic peak on heating, whereas the doubled melting peaks may be affected by impurity components of the purified ionic liquids. The  $T_g$  is the midpoint of a small heat capacity change on the heating from the amorphous glass state to a liquid state. During cooling from 100 °C down to -120 °C, it is characterized by no freezing phase transition but only the formation of an amorphous glass. The  $T_c$  temperature is defined as the onset

of an exothermic peak on heating from a sub-cooled liquid state to a crystalline solid-state.<sup>101</sup>

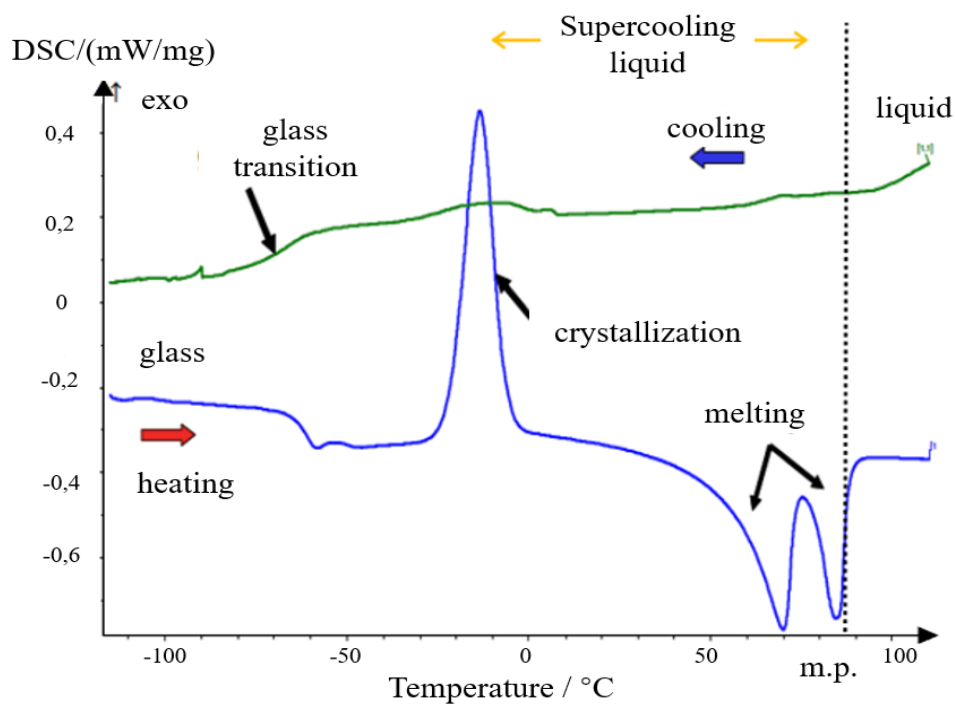


Figure 3.1 Schematic illustration of the DSC curve tracking from the example of purified EMImCl. Reproduced from the reference of [102]. Copyright 2008 Elsevier Ltd.

The DSC measurement was carried out by using a TA Instruments Q2000 with liquid N<sub>2</sub> cooling. The samples were hermetically sealed in Al pans. An empty Al pan was used as the reference. The thermal treatment included cycling from -80 to 80 °C at a rate of 5 °C min<sup>-1</sup> with a sub-ambient annealing procedure to promote any possible crystallization. The measurements were carried out at Helmholtz Institute Ulm (HIU), Germany.

## 3.1.2 Small Angle X-ray Scattering (SAXS)

Small-angle X-ray scattering (SAXS) is an analytical technique primarily employed for the determination of sizes and shapes of supermolecular structures, colloidal particles, and other types of heterogeneous agglomerates without disturbing their natural environment.<sup>103</sup> More importantly, it can also be applied directly to the nanoparticles in suspension without extensive sample preparation. As illustrated in Figure 3.2, the parallel and monochromatic X-ray beam impinge on the suspensions, and a small fraction of the radiation is scattered off the materials in forwarding direction under small angles ( $2-5^\circ$ ) around the transmitted direct beam. The scattering pattern is independent of the azimuthal angle; thus the scattering image can be circularly integrated to obtain the scattered intensity as a function of the scattering angle.

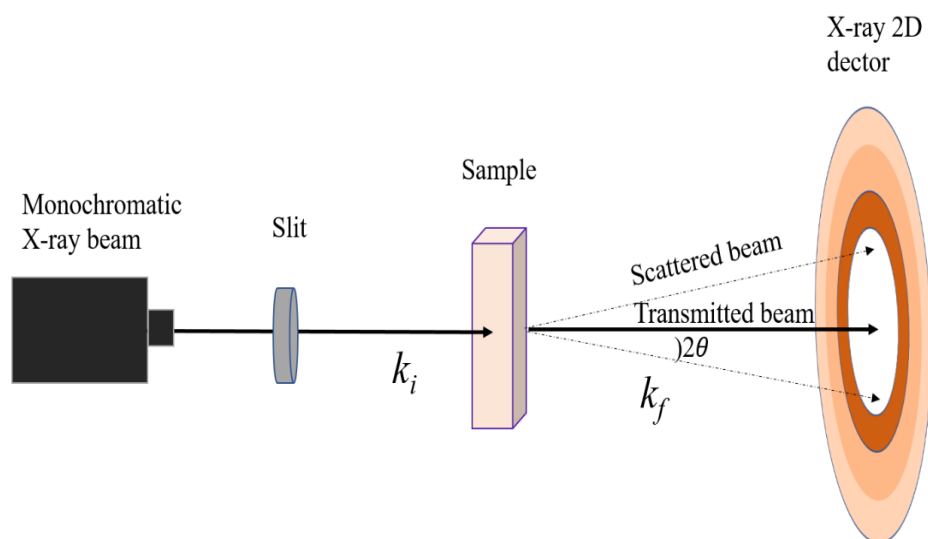


Figure 3.2 Schematic principle of a SAXS measurement on nanoparticles in suspension.<sup>104</sup>

In a scattering experiment, the scattered intensity is usually analyzed as a function of the momentum transfer ( $q$ ), which is given by Equation 3.1,

$$q(\theta) = \frac{4\pi \sin \theta}{\lambda} \quad 3.1$$

where  $\lambda$  is the wavelength of the incident X-ray beam, and  $\theta$  is half of the scattering angle. For sufficiently monodisperse particle suspensions, the scattering curves  $I(q)$  show pronounced oscillations depending on the particle diameter and can be evaluated by fitting the scattered intensity with a model.

In this work, Small-angle X-ray scattering (SAXS) experiments were performed with a Xenocs XEUS 2.0 set-up, equipped with a Cu  $K_\alpha$  source (wavelength,  $\lambda = 1.54 \text{ \AA}$ ) and a Pilatus 1M detector (Dectris, Switzerland). The samples were sealed in the thin-walled (wall thickness 0.01 mm), quartz capillaries (Hilgenberg GmbH, Mansfeld, Germany) with epoxy resin or paraffin oil, and all samples were measured in the vacuum chamber attached to the X-ray set-up. The measurements were carried out at the Leibniz Institute for New Materials (INM), Germany.

### 3.1.3 Electron paramagnetic resonance (EPR) spectroscopy

Electron paramagnetic resonance (EPR), also known as electron spin resonance (ESR) is a powerful spectroscopic technique to detect detailed information about structure and bonding of unpaired electrons in the molecules, including radicals, transition metal ions, and crystalline defects.<sup>105-106</sup> In an applied magnetic field ( $B_0$ ), two spinning states are labeled by the projection of the electron spin quantum number ( $M_s$ ) due to the Zeeman effect. In the direction of the magnetic field,  $M_s = -1/2$  is the

parallel state, and  $M_s = 1/2$  is the antiparallel state.

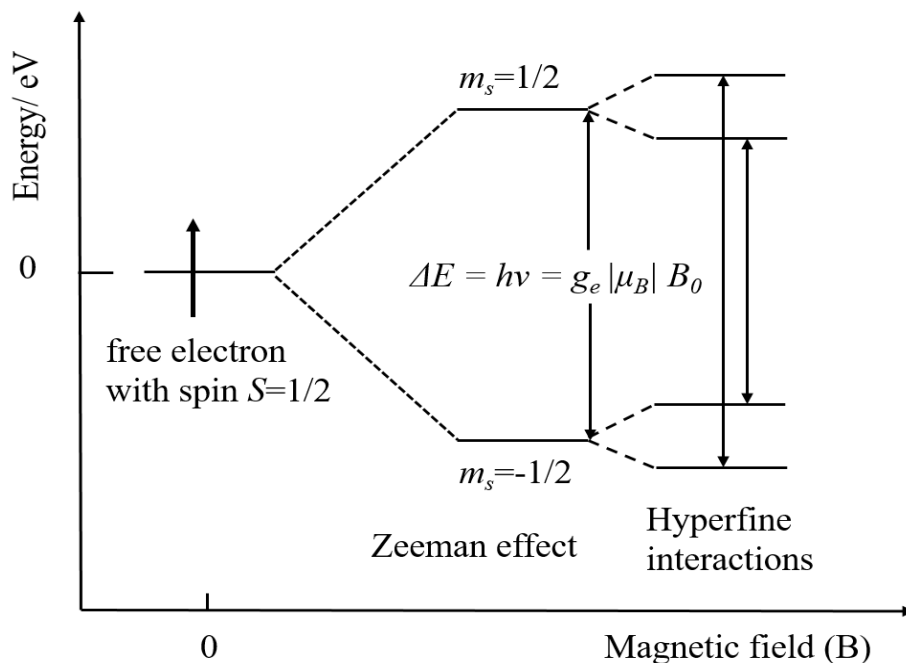


Figure 3.3 Illustration of a spin system with one electron  $S=1/2$  and a nucleus  $I=1/2$  with isotropic electron Zeeman splitting and hyperfine interactions.

The energy state of the unpaired electron can be defined in Equation 3.2,

$$E = g_e \mu_B B_0 M_s \quad 3.2$$

where  $g_e$  is a dimensionless constant,  $\mu_B$  is the Bohr magneton,  $B_0$  is the magnetic field, and  $M_s$  is the electron spin quantum number.

In addition to the applied magnetic field, unpaired electrons are also sensitive to their local environments. Frequently, the nuclei of the atoms in a molecule or complex have a magnetic moment, which produces a local magnetic field to the electron. Therefore, a hyperfine interaction between the electron and the nuclei is generated as

illustrated in Figure 3.3. Hyperfine interactions are used to provide some essential information about the sample such as the number and type of nuclei in a complex as well as their distance from the unpaired electron.<sup>106</sup>

The electron paramagnetic response (EPR) measurements were performed at room temperature using a Magnettech MS5000 Desktop spectrometer operating at ~9.49 GHz (X band), 0.3 mW microwave power with 0.1 mT modulation amplitude at 100 kHz. The EPR samples were collected from different states of charge/discharge of a flow cell. The solutions were filled in 50  $\mu$ L micropipettes (Blaubrand<sup>®</sup> intraMARK), and the two ends of the tubes were sealed with paraffin oil. All operations prior to recording the EPR spectra were carried out in an argon-filled glovebox. The measurements were carried out at Saarland University, Germany

#### 3.1.4 Ionic conductivity measurements

The ionic conductivities of electrolytes in wide temperature ranges were determined by an automatic conduct meter equipped with a frequency analyzer and a thermostatic bath (MMates Italia). The samples were housed in sealed glass conductivity cells (mounted in an argon-filled glove box) equipped with two platinized platinum electrodes. The cell constants were determined using a 0.01 M KCl standard solution. The measurements were run in the temperature range from -40 to 70 °C, the equilibration time at each temperature is 1 h.

At room temperature, the ionic conductivity of a set of “water in-ionic-liquids” electrolytes at different molalities was recorded on a WTW Cond 3110 portable

conductivity meter (Xylem, Germany).

### 3.1.5 Rheological properties measurements

The rheological behavior of the solutions was measured on a MCR 301 (Anton Paar GmbH, Graz, Austria) rheometer using a cone-plate (50 mm diameter) measuring system by applying shear rates from 0 to 1500 s<sup>-1</sup> at different temperatures from 25 to 80 °C. The measurements were carried out at Saarland University, Germany.

## 3.2 Electrochemical techniques

### 3.2.1 Cyclic voltammetry (CV)

Cyclic voltammetry is a very powerful technique for acquiring qualitative information about the redox processes on an electrode surface, such as reaction mechanism, the stability of reaction intermediates, and kinetics of heterogeneous electron transfer reactions.<sup>103</sup> In particular, it offers a rapid localization of the redox potentials of electroactive species and favorable evaluation of the effect of solution media on the redox process.

Cyclic voltammetry is a potentiodynamic electrochemical measurement in which the working electrode's potential switches between potential limits  $E_{\max}$  and  $E_{\min}$  at a known sweep rate in repeated cycles (Figure 3.4a). Cyclic voltammogram gives the plot of current density ( $j$ ) versus applied potential ( $E$ ) (Figure 3.4b). The electroactive species loses an electron at the electrode giving rise to an anodic peak current ( $i_{pa}$ ), and an oxidation peak at a given potential ( $E_{pa}$ ). When the potential is applied in the negative

direction, the cathodic peak current ( $i_{pa}$ ) and potential ( $E_{pa}$ ) is observed on the reduction

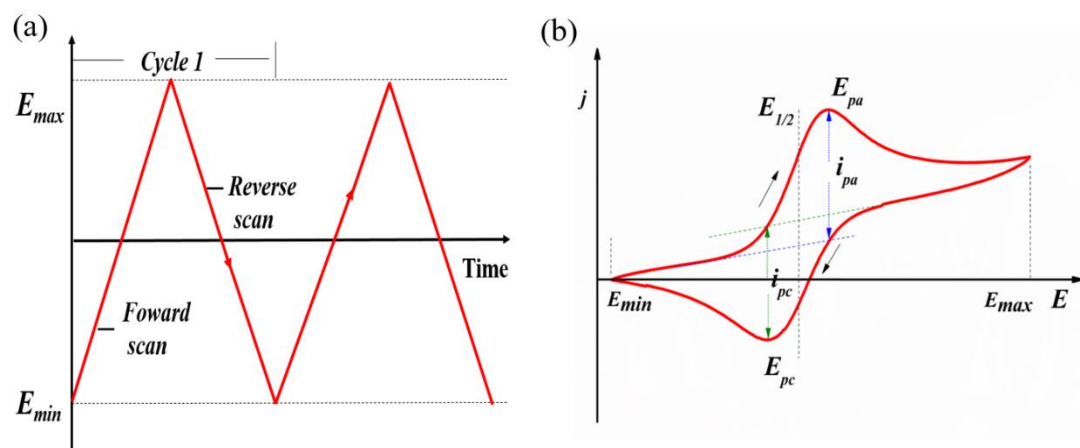


Figure 3.4 (a) The triangular potential sweep waveform used for the CV measurement. (b) The typical cyclic voltammogram recorded corresponding to the potential sweep.

process. For an electrochemically ideal reversible electron transfer process, the recorded CV has certain well-defined characteristics: (i) the potential separation ( $\Delta E$ ) between the anodic and cathodic peaks potential is  $59 \text{ mV}/n$ ; (ii) the peak current ratio of cathodic ( $i_{pc}$ ) and anodic ( $i_{pa}$ ) reaction is equal to one; (iii) the peak current shows a linear relationship with the square root of sweep rates.

In this work, the CV measurements were conducted on a BioLogic SP150 potentiostat/galvanostat via EC-Lab software. Three-electrode CV tests were performed using a glassy carbon working electrode (1.0 mm diameter), a platinum foil counter electrode, and a silver wire quasi-reference electrode (0.197 V vs. SHE<sup>103</sup>). The immersion height of the glassy carbon is around 0.3 cm in the measured solution, which offers a contacting surface area of  $0.102 \text{ cm}^2$ . The argon gas was bubbled for 10 min to

eliminate the dissolved oxygen in the solution prior to each measurement.

### 3.2.2 Rotating disk electrode (RDE) technique

The rotating disk electrode is a classic hydrodynamic electroanalytical technique used to elucidate the kinetics of heterogeneous reactions and mass transport characteristics. Figure 3.5a illustrates the employed three-electrode setup, in which the RDE consists of a disc of the electrode material imbedded in a rod of insulating material. Laminar flow is formed on the surface of electrodes following the working electrode rotation by a motor. Therefore, a steady migration/diffusion is attained very quickly and the effect from the double-layer charging current is mitigated due to the exponential decay of the double layer charging current with time.

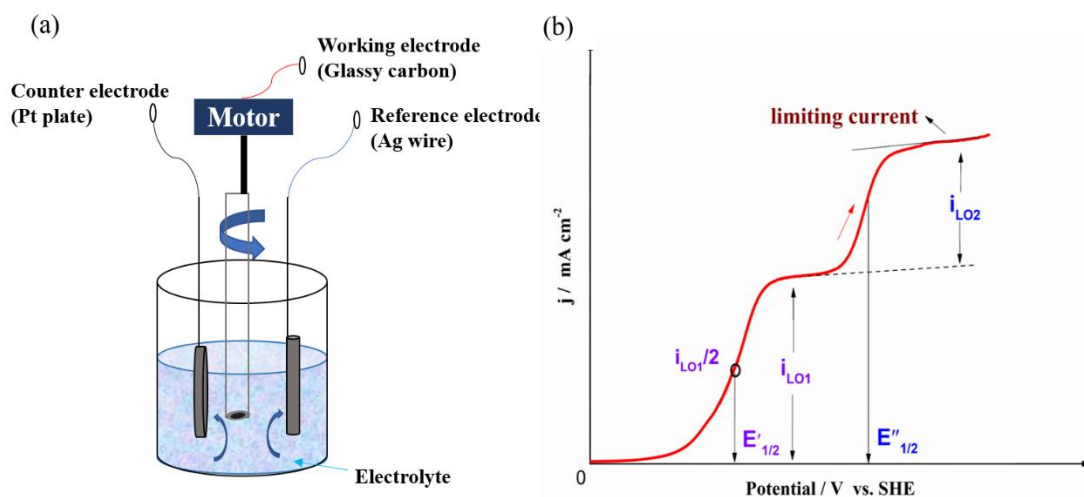


Figure 3.5 (a) Scheme of a three-electrode system for RDE measurements. (b) The typical linear-scan voltammogram for multi-electron reduction under stirred condition.

The linear sweep voltammetry (LSV), similar to the cyclic voltammetry technique,

is commonly used for quantitative analysis in RFBs. In this experiment, the current on a working electrode is recorded while the electrode potential is changed linearly with time from an initial potential to an end potential (Figure 3.5b). The limiting currents as a function of rotation rates are given by the *Levich equation* in Equation 3.3,

$$i_l = 0.62 nFACv^{-1/6}\omega^{1/2}D_i^{2/3} \quad 3.3$$

where  $i_l$  is the limit current,  $D_i$  is the diffusion coefficient ( $\text{cm}^2 \text{s}^{-2}$ ), and  $\nu$  is the kinematic viscosity ( $\text{cm}^2 \text{s}^{-1}$ ).

For the RDE tests, the electrolyte characterization was conducted using a Pine Instruments with a 5 mm diameter ( $0.196 \text{ cm}^2$ ) glassy carbon working electrode, a platinum plate counter electrode, and an Ag wire reference electrode. Electrochemical measurements were carried out using a Bio-logic VMP-300 multichannel potentiostat controlled by EC-lab<sup>®</sup> software. Prior to the data collection, the electrolytes were purged with Ar gas for 20 min; each measurement was repeated three times to acquire averaged limit currents.

### 3.2.3 Electrochemical impedance spectroscopy (EIS)

Electrochemical impedance spectroscopy is established as a powerful tool for investigating the component resistances in a circuit. It is essentially determined by applying an AC potential (current) to an electrochemical cell and then measuring the evolving current (potential) at different frequencies. As illustrated in Figure 2.3, electrons transportation includes mass transport and a kinetically controlled process. The data were usually displayed in form of Nyquist-plots, imaginary resistance ( $-Z''$ )

versus real resistance ( $Z'$ ), with a depressed semicircle from which the component resistances can be extracted (Figure 3.6).

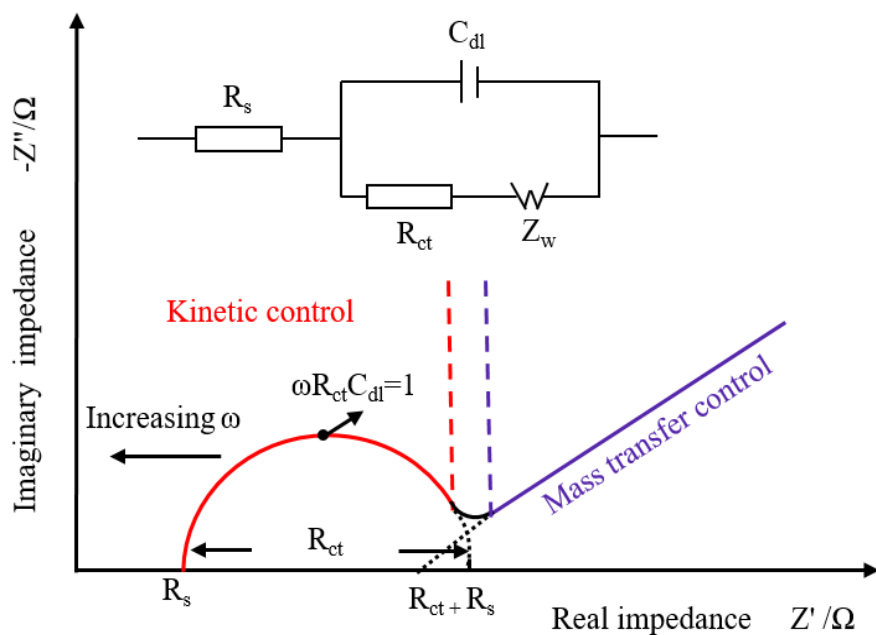


Figure 3.6 The Nyquist plot of the electrolyte resistance and the representative Randle equivalent circuit.

The first intercept at the high-frequency region represents the bulk solution resistance ( $R_s$ ), including the electrolyte resistance, the electrode resistance, and the contact resistance. The semicircle (red curve) in the medium frequency region is called the kinetic control region. It represents the double-layer capacitance ( $C_{dl}$ ) and the charges transfer resistance ( $R_{ct}$ ). The low frequency describes the diffusion process from the diffuse layer to the electrode surface, which is defined as a Warburg impedance with a slope angle of  $45^\circ$ . All the elements related to the Nyquist plot can be modeled

to a Randles equivalent circuit (inset in Figure 3.6). Herein,  $R_s$  correlates to the system resistance,  $C_{dl}$  models the capacitive behavior of the electrical double layer. The series of  $R_{ct}$  and Warburg diffusion element ( $W$ ) are placed in parallel to the electric double layer.<sup>107</sup>

To determine the internal cell resistance, EIS was performed at open circuit potential after assembling the cell with a sine voltage waveform of the amplitude of 10 mV at frequencies ranging between 200 kHz and 100 mHz using an EC-lab potentiostat station. Each measurement was conducted at different temperatures depending on the requirements

#### 3.2.4 Galvanostatic cycling

The galvanostatic cycling technique is used for characterizing the capability and cyclability of electroactive species. In the galvanostatic method, a current pulse is applied to the working electrode, and the resulting potential is measured against a reference electrode as a function of time. When the current is applied in the initial state, the measured potential abruptly changes due to the internal resistance loss. After that, it gradually changes because concentration overpotential is developed across the electrode as the concentration of the reactants is depleted at the electrode surface. The capacity ( $Q$ ) is quantified based on the running time ( $t$ ) at a specific flux current ( $i$ ), as given in Equation 3.4.

$$Q = \int_0^t i dt \quad 3.4$$

In this thesis, the flow cells were conducted in the specific potential ranges under

constant charge/discharge current densities using a Biologic SP150 potentiostat or Biologic VMP-300 multichannel potentiostat. The detailed operating parameters of each measurement will be described in Chapter 4.

### 3.3 Electrolytes and cell preparation

#### 3.3.1 Preparation of supporting electrolytes

The ionic liquids like BMImCl ( $\geq 98.0\%$ , Sigma Aldrich) and EMImCl (97%, Acros Organics) were used as received without further purification. The aqueous solutions with different molalities ( $m = \text{mol kg}^{-1}_{\text{water}}$ , differing from  $M = \text{mol L}^{-1}_{\text{solution}}$ ) of imidazolium chlorides were prepared by mixing the ionic liquids with a particular volume of distilled water. For instance, to obtain a 3 m BMImCl/H<sub>2</sub>O, 0.524 g (i.e., 3 mmol) BMImCl was added into 1 g distilled water.

#### 3.3.2 Solubility test of redox-active species

Solubility is the maximum concentration of a redox molecule in a solvent or a supporting electrolyte, which is proportional to the theoretical capacity and energy density of an RFB. Moreover, the solubility significantly affects the installation cost of RFBs. The solubility limits of investigated active species were measured by dissolving the solid powders into the BMImCl/H<sub>2</sub>O or EMImCl/H<sub>2</sub>O solutions until no further solid could be dissolved. Note that the amounts of active species and the final volume of the solutions were recorded to calculate the final concentration ( $M, \text{mol L}^{-1}_{\text{solution}}$ ) of the active materials. All the tests were conducted at room temperature.

## 3.3.3 Preparation of redox-active electrolytes

Anolyte and catholyte with different concentrations were prepared by dissolving a specific amount of redox-active species into the supporting electrolytes with balanced mole electrons. The volumetric energy density was calculated based on the volume of the catholyte compartment.

## 3.3.4 Pre-treatment of graphite felt

The graphite felt (GFD4.6 EA, Sigracell<sup>®</sup> Carbon) with an uncompressed thickness of 4.6 mm, and compression of 20% was first immersed in 3 M H<sub>2</sub>SO<sub>4</sub> for 24 h and then thermally treated at 400 °C for 24 h in static air atmosphere. Two pieces of graphite felts were used for the cathode and anode.

## 3.3.5 Pre-treatment of ion exchange membrane

In Chapter 4.2 and Chapter 4.4, a cross-linked methylated polybenzimidazole (PBI) anion exchange membrane (Figure 3.7) with 10% crosslinker and 45 μm in thickness were pretreated in 1 M NaCl for 12 h prior to the usage.

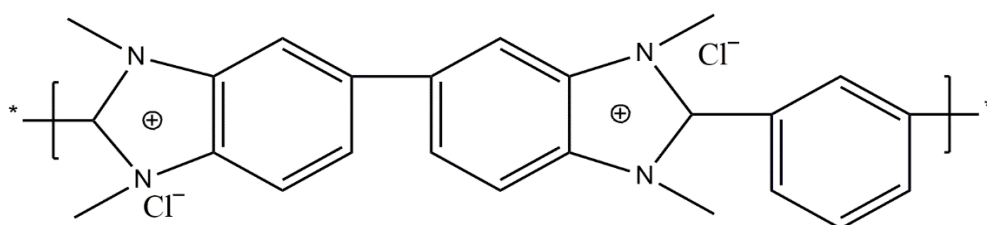


Figure 3.7 Structure of a crosslinked and methylated meta-PBI membrane.

In Chapter 4.3, the commercial fumasep<sup>®</sup> FAA-3-30 anion exchange membrane (thickness: 30  $\mu\text{m}$ , non-reinforced, dry membrane delivered in bromine form, Fumatech BWT GmbH, Germany) was soaked in 1 M KOH at 60 °C for 30 min and then immersed in 1 M NaCl for 24 h. Accordingly, the membrane was exchanged into OH<sup>-</sup> form, then into chloride form. The dimensional change of swelling in length is about 5 % after soaking step; the membrane size remained constant afterward. The pretreated membranes were stored in aqueous imidazolium solutions at room temperature before use, and assembled in a cell in wet form.

#### 3.3.6 Preparation of flow cell

The home-made flow cell comprising endplates, copper current collectors, graphite felt electrodes, and the ion-exchange membrane was step-by-step symmetrically assembled. The electrolytes stored in the exterior tanks were flowed through the electrochemical cell using a peristaltic pump (ShenChen Pump, China) at a constant flow rate. Prior to the measurements, the electrolytes were bubbled with Ar gas for 10 min to reduce the concentration of dissolved oxygen and then sealed with paraffin oil (Roth, Germany) on the top layer. The detailed preparations based on the measuring requirements of the conducting cell were described in Chapter 4.

---

## 4. Results and discussions

### 4.1 Physicochemical properties of water-in-ionic liquids electrolytes

To demonstrate our concept, the binary mixtures of water-in-ionic liquids (aq-ILs) supporting electrolytes were prepared by mixing water with 1-ethyl-3-methylimidazolium chloride (EMImCl) and 1-butyl-3-methylimidazolium chloride (BMImCl) for a required molality (Figure 4.1a). All investigated samples are completely miscible at room temperature. For a series of supporting electrolytes with variable amount of water, it was observed that the final volume expanded with increasing content of ionic liquid (Figure 4.1b). The water proportion in the liquid mixture decreases correspondingly from more than 65% to a low value of about 18% at the molality of 3 and 30 m, respectively. (Table 4–1). The higher weight density of EMImCl is attributed to the shorter alkyl chain length in the cations.<sup>108</sup>

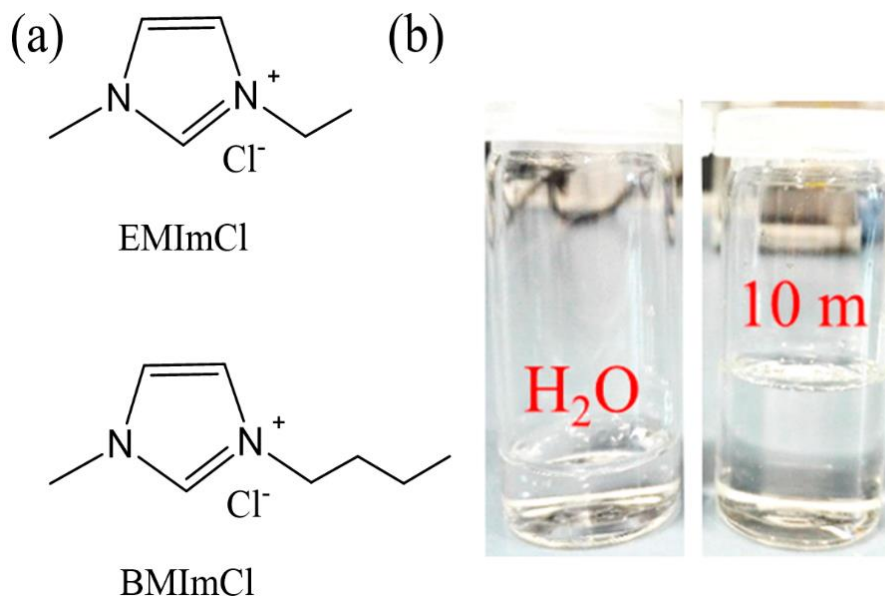


Figure 4.1 (a) Molecular structure of the employed imidazolium-based ionic liquids. (b) The photos show 1 mL H<sub>2</sub>O and a solution of 10 m BMImCl/H<sub>2</sub>O in glass vials.

Table 4–1 Summary of the physicochemical properties of the imidazolium-based electrolytes at different molalities.

Molality (mol kg <sup>-1</sup> )	EMImCl (Mw = 146.62 g mol <sup>-1</sup> )				BMImCl (Mw = 174.67 g mol <sup>-1</sup> )			
	Volume expansion (mL)	Water ratio (wt%)	Water ratio (vol%)	Mass density (g cm <sup>-3</sup> )	Volume expansion (mL)	Water ratio (wt%)	Water ratio (vol%)	Mass density (g cm <sup>-3</sup> )
3 m	0.39	69.5%	71.9%	1.0608	0.48	65.6%	67.6%	1.0519
5 m	0.65	57.7%	60.6%	1.0860	0.80	53.4%	55.6%	1.0613
10 m	1.30	40.5%	43.5%	1.1152	1.61	36.4%	38.3%	1.0903
20 m	2.60	25.4%	20.4%	1.1302	3.23	22.3%	23.6%	1.1022
30 m	3.89	18.5%	17.8%	1.1506	4.85	16.0%	17.1%	1.1196

Note: The initial volume of 1 mL distilled water was measured with a micropipette. Mass density EMImCl=1.13 g cm<sup>-3</sup> [109], BMImCl=1.08 g cm<sup>-3</sup> [110].

The transport and rheological properties of the supporting electrolytes play a critical role, thus would affect the capacity utilization and power density of the battery. Figure 4.2 shows that the liquids of EMImCl/H<sub>2</sub>O have a higher ionic conductivity than that of BMImCl samples owing to their shorter alkyl chain on the imidazolium cation. The dependence of the conductivity on the IL concentration follows the typical pattern of concentrated electrolyte solutions. After a rapid initial rise at low IL fraction due to the increasing number of charge carriers, then, conductivity passes through a pronounced peak due to the counter-balancing effect of the rapidly rising viscosity on the ion mobility.<sup>111</sup> The maximum of 58.5 mS cm<sup>-1</sup> at 3 m for the BMImCl/H<sub>2</sub>O, and a maximum of 83.9 mS cm<sup>-1</sup> at about 3.5 m for the EMImCl/H<sub>2</sub>O were observed.

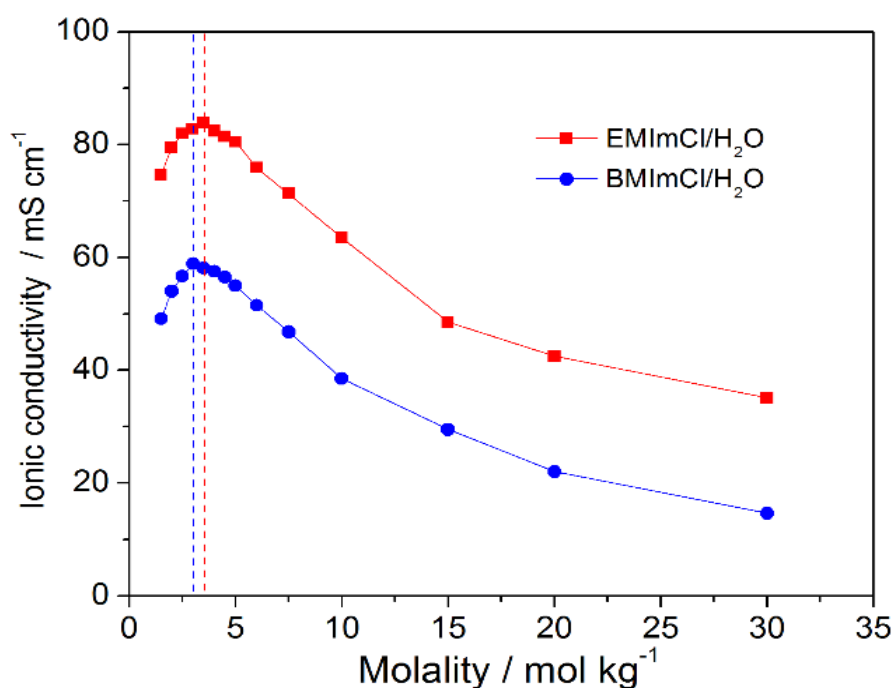


Figure 4.2 Ionic conductivity of BMImCl/H<sub>2</sub>O and EMImCl/H<sub>2</sub>O solutions in different molalities.

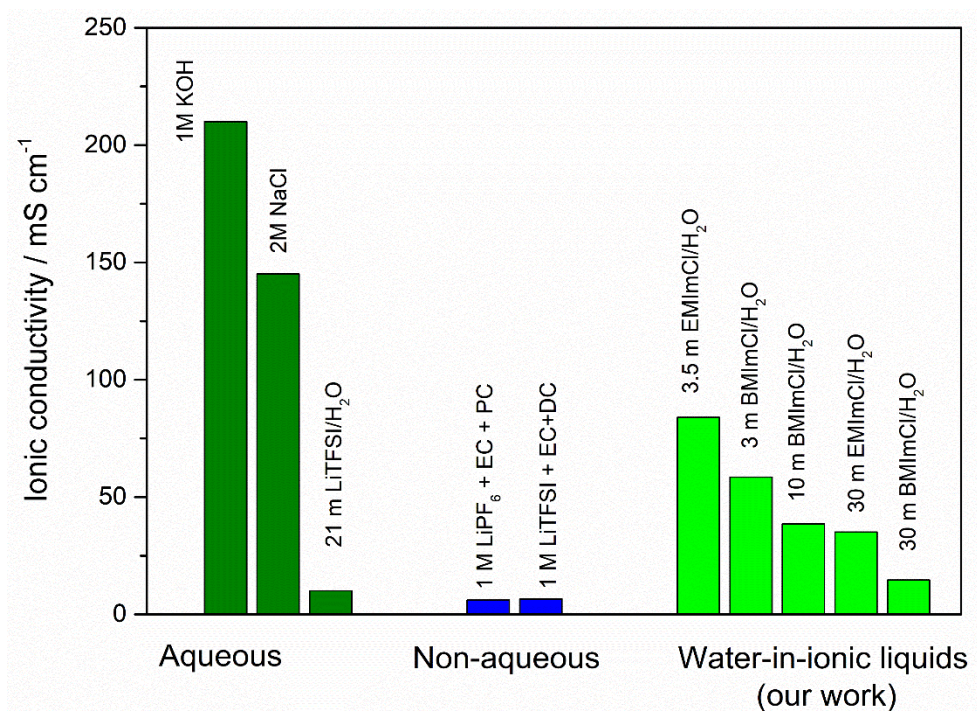


Figure 4.3 Comparison of the ionic conductivity between the obtained Water-ion-ionic liquids electrolytes and conventional electrolytes in batteries.

As shown in Figure 4.3, these values are approaching that (85.7 mS cm<sup>-1</sup>) of 1 M aqueous NaCl.<sup>52</sup> Even for the higher concentration of 30 m solutions, the ionic conductivity of 14.6 mS cm<sup>-1</sup> is still higher than the commercial non-aqueous electrolytes for lithium-ion batteries,<sup>44</sup> and the reported “water-in-lithium-salt electrolyte” (~10 mS cm<sup>-1</sup> at 21 m).<sup>97</sup>

Next, the plot of viscosity as a function of the applied shear rate is shown in Figure 4.4. All solutions exhibited Newtonian fluid behavior. As shown in Figure 4.4a, the viscosities increased from 1.8 mPa s (3 m EMImCl/H<sub>2</sub>O, compared to 1 mPa s for pure water) to 9.8 mPa s (10 m BMImCl/H<sub>2</sub>O). The higher viscosity of BMImCl/H<sub>2</sub>O is in accordance with the results in ionic conductivity caused by the long alkyl chain structure. Interestingly, these values are close to those of typical aqueous solutions of

$\text{H}_2\text{SO}_4$ ,<sup>12</sup> and  $\text{NaCl}$ .<sup>40</sup> In addition, the viscosity of the 30 m BMImCl/ $\text{H}_2\text{O}$  reduces from about 43 to 13 mPa s by increasing the temperature from 25 to 80 °C (Figure 4.4b).

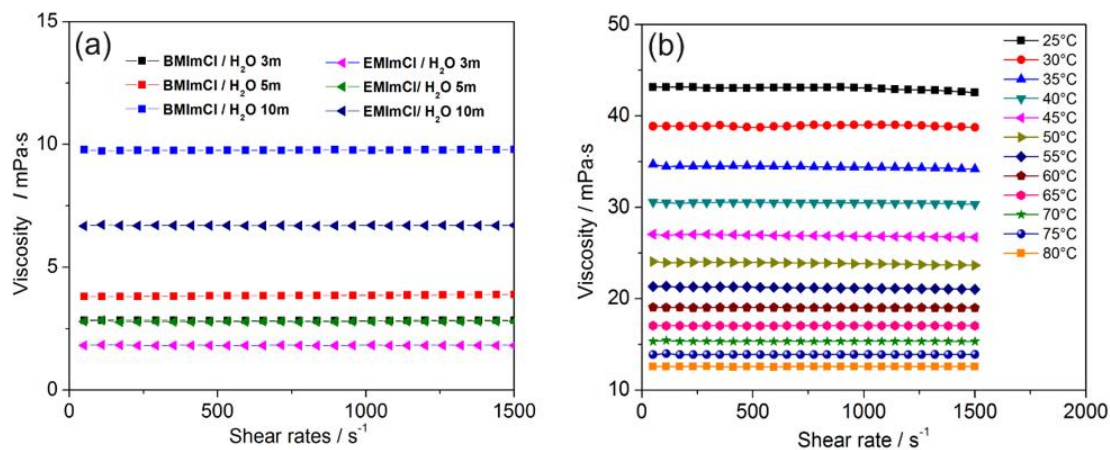


Figure 4.4 Rheological properties of BMImCl/ $\text{H}_2\text{O}$  and EMImCl/ $\text{H}_2\text{O}$  solutions. (a) viscosity at different molalities from 3 to 10 m at shear rates of 0–1500  $\text{s}^{-1}$  at room temperature, (b) 30 m BMImCl/ $\text{H}_2\text{O}$  at different temperatures from 25 to 80 °C.

Table 4–2 Summary of ionic conductivity and viscosity of supporting electrolytes at 25 °C.

Molality (mol kg <sup>-1</sup> )	EMImCl/ $\text{H}_2\text{O}$		BMImCl/ $\text{H}_2\text{O}$	
	Ionic conductivity (mS cm <sup>-1</sup> )	Viscosity (mPa s)	Ionic conductivity (mS cm <sup>-1</sup> )	Viscosity (mPa s)
3 m	82.8	1.82	58.9	2.84
5 m	80.5	2.78	55	3.84
10 m	63.5	6.70	38.5	9.76
20 m	42.5	/	22	/
30 m	35.1	/	14.64	43.1

According to the results in Table 4–2, a Walden plot of the BMImCl/ $\text{H}_2\text{O}$  and

EMImCl/H<sub>2</sub>O with molalities from 3 to 30 m is depicted in Figure 4.5. Both aqueous solutions showed good ionic properties. For flow cell tests aiming at a high operating current density, the optional concentration of imidazolium chloride electrolytes was therefore chosen as an alternative supporting electrolyte with respect to ionic conductivity and viscosity.

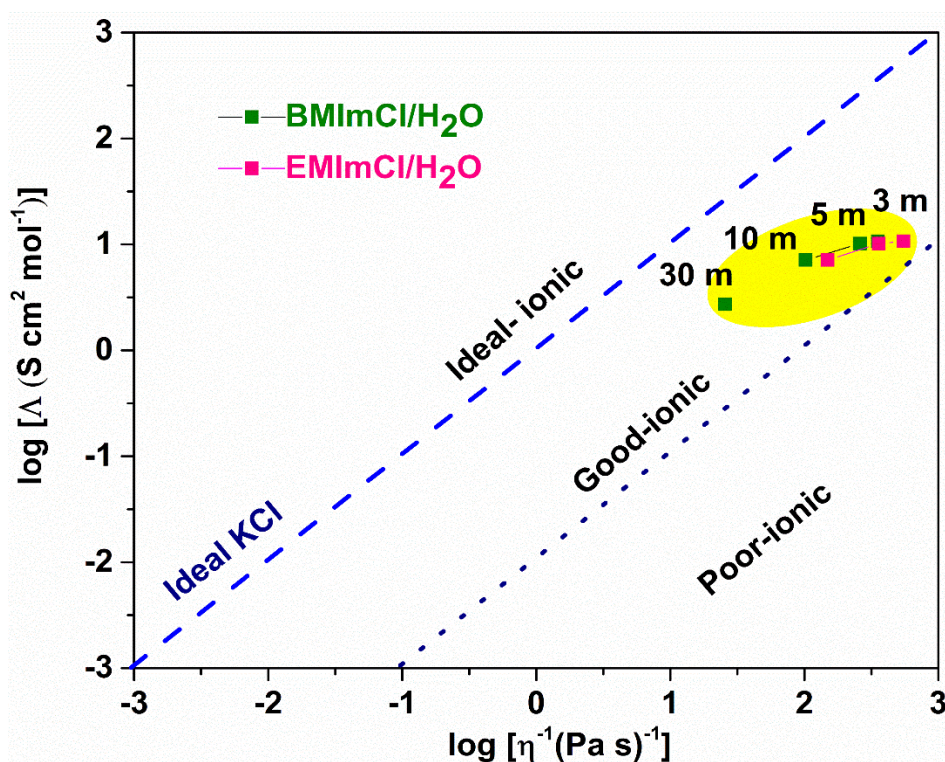


Figure 4.5 Walden plot of the aqueous imidazolium chlorides with different molalities.

---

## 4.2 Aqueous ionic liquid electrolytes for all-climate RFB application

This chapter is predominantly based on the publication:

**Z. Huang**<sup>†</sup>, P. Zhang<sup>†</sup>, X. Gao, D. Henkensmeier, S. Passerini, R. Chen, Unlocking Simultaneously the Temperature and Electrochemical Windows of Aqueous Phthalocyanine Electrolytes, *ACS Appl. Energy Mater.* **2**, 3773-3779 (2019), (<sup>†</sup>equal contribution), Copyright 2019 American Chemical Society. [Dol: 10.1021/acsaem.9b00467](https://doi.org/10.1021/acsaem.9b00467)

### 4.2.1 Motivations

The change from organic solvents to aqueous solvents for safe battery electrolytes is desirable for the ever-increasing demands of electrochemical energy storage. However, the traditional water-based electrolytes possess a narrow electrochemical stability window (1.23 V) and tend to freeze at sufficiently low temperatures, thermodynamically. Such properties clearly restrict high-voltage applications and temperature adaptability. All-climate battery electrolytes can hardly be realized simultaneously in the conventional aqueous solvents. Ionic liquids are thermally stable and potentially wide at room temperature.<sup>95</sup> So it is possible to design novel ionic liquids contained electrolytes for all-climate RFBs.

In this chapter, we report a reliable aqueous supporting electrolyte containing imidazolium chloride having unprecedented properties of largely widened electrochemical and temperature windows. The electroactive electrolytes consisting of inexpensive metal phthalocyanine tetrasulphonic acid ( $[\text{Me}^{\text{II}}\text{TsPc}]^{4-}$ ) were investigated, which has multi-electron transfer reactions at low negative potentials that are not accessible in conventional aqueous electrolytes. The application of such electrolyte in a phthalocyanine/Fe redox flow battery demonstrated a negligible dependence on the

operating temperature.

#### 4.2.2 Thermophysical properties of supporting electrolytes

The water-soluble organometallic compound  $[\text{Me}^{\text{II}}\text{TsPc}]^{4-}$ , a class of macrocyclic planar aromatic compounds in which the central metal of the metal phthalocyanine is coordinated to four N atoms while the crystal consists in ring-stacked columns, was studied as electroactive materials (Figure 4.6).<sup>112</sup> Upon reduction, electrons can be added to the ligand orbital or the metal center, governed by the electronic configuration. For  $\text{Me} = \text{Cu}$  and  $\text{Ni}$ , the ligand rings undergo successive reduction, while the central metals remain electrochemically silent.

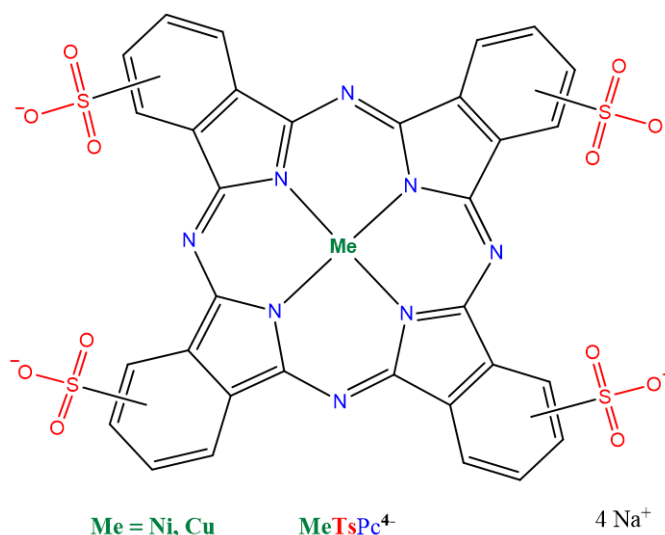


Figure 4.6 Chemical structure of  $\text{Na}_4[\text{MeTsPc}]$ ,  $\text{Me} = \text{Ni}, \text{Cu}$ .

Small-angle X-ray scattering (SAXS), as a sensitive technique to characterize the bulk crystallization of water, phase separation and formation of agglomerate structures in a solution,<sup>113</sup> was recorded for the NiTsPc solutions (0.05 M) in neat water and the 10 m BMImCl/H<sub>2</sub>O. The studies of thermal stability of the pure supporting electrolyte and redox-active electrolytes were conducted in the heating stage with the XEUSS 2.0 set-up. The structural changes as a function of temperature were characterized in the

range of  $-20$  to  $20$  °C (with the stability of  $\pm 1$ °C) at an interval of  $2$  °C per step, and the radial integration of the primary data was undertaken with the Foxtrot software (version 3.2.7, SOLEIL, France). The 2D scattering images are shown in Figure 4.7 in  $[2\theta, \Psi]$  polar coordinates. At  $20$  °C, no scattering ring was observed for both samples (left images in Figure 4.7a, b).

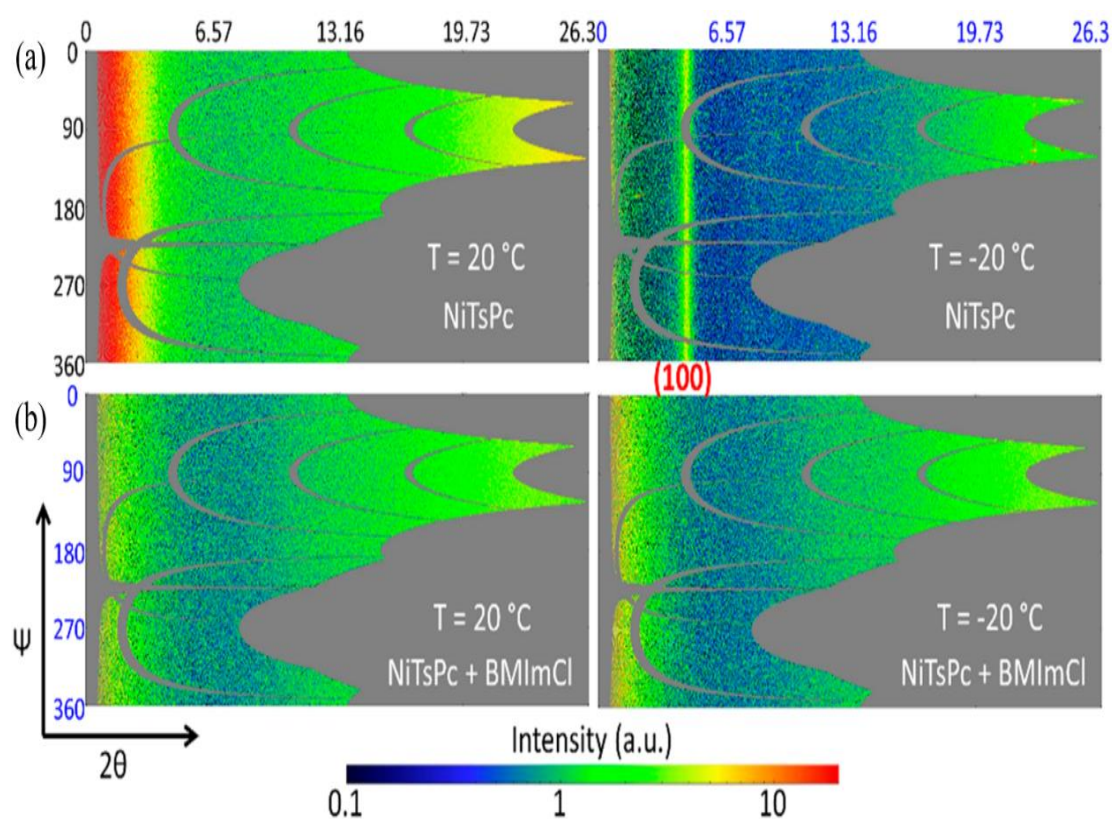


Figure 4.7 Influence of BMImCl on the X-ray scattering profiles and temperature-response behavior of aqueous NiTsPc samples (0.05 M). Typical 2D  $[2\theta, \Psi]$  polar patterns of aqueous NiTsPc (a) and NiTsPc/BMImCl (b) samples collected at  $20$  and  $-20$  °C. The grey area indicates positions of the beam stop, Pilatus detector modular gaps and flight tube shadows were masked off for data integration.

However, at  $-20$  °C, a new scattering ring can be seen for the neat aqueous NiTsPc sample (top-right in Figure 4.7a), indicating the presence of crystallized species at such a low temperature. In contrast, there is no scattering peak for the sample containing BMImCl, implying that the NiTsPc material is well dispersed in water and the absence

of bulk water behavior at  $-20\text{ }^{\circ}\text{C}$  (down-right in Figure 4.7b).

To trace the structural changes with temperature, in situ SAXS experiments of the two samples were carried out by first cooling the samples from  $20$  to  $-20\text{ }^{\circ}\text{C}$  (left panels in Figure 4.8), and then heating to  $20\text{ }^{\circ}\text{C}$  (right panels in Figure 4.8). The patterns were recorded at an interval of  $2\text{ }^{\circ}\text{C}$  per step.

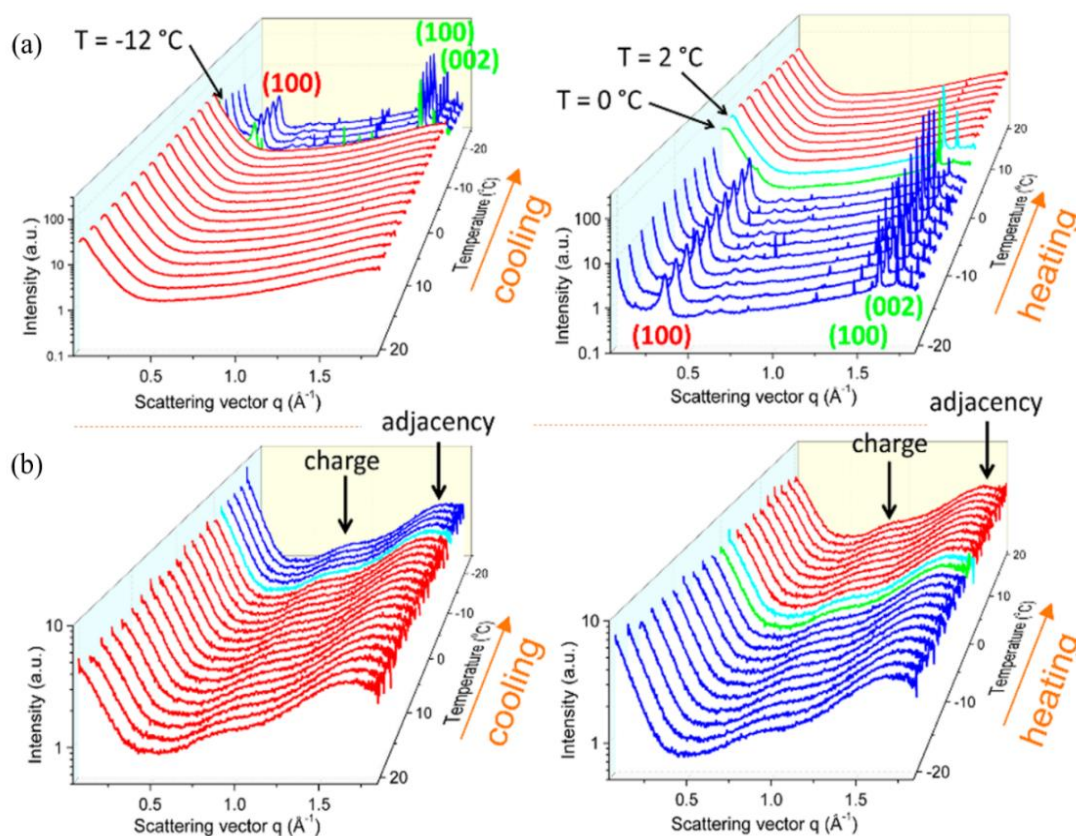


Figure 4.8 Evolution of the SAXS patterns during the in situ cooling/heating experiments between  $20$  to  $-20\text{ }^{\circ}\text{C}$  for (a) aqueous NiTsPc sample, and (b) aqueous NiTsPc/BMImCl sample, respectively.

In Figure 4.8a, upon cooling a peak at  $q = 0.32\text{ }^{\circ}\text{Å}^{-1}$ , corresponding to a real space of  $19.6\text{ }^{\circ}\text{Å}$  calculated by  $2\pi/q$ , appeared at temperatures below  $-12\text{ }^{\circ}\text{C}$ . This peak can be attributed to the (100) reflection of the NiTsPc crystals.<sup>114-115</sup> Meanwhile, peaks in the high  $q$  values of  $1.6$  and  $1.72\text{ }^{\circ}\text{Å}^{-1}$  were observed below  $-12\text{ }^{\circ}\text{C}$  in Figure 4.8a, which can be attributed to (100) and (002) reflections of ice. Such crystallization behavior

depends on the thermodynamic Gibbs energy of mixing.<sup>116</sup> During the reverse heating process, these crystallization peaks disappeared at above 2 °C. In strong contrast, the aqueous sample containing BMImCl showed a distinct X-ray scattering profile without any crystalline feature corresponding to ice and NiTsPc crystals over the whole temperature loop, as shown in Figure 4.8b.

The scattering features are characterized by weak and broad humps centered at around  $q = 0.85, 1.65 \text{ \AA}^{-1}$ , as also found in the aqueous BMImCl solution (Figure 4.9), corresponding to the charge alternation of the ionic domains and adjacency order (intra- and intermolecular packing of adjacent atoms), respectively.<sup>117-118</sup> The overlapped profiles between the neat BMImCl sample (which contains a trace amount of moisture because it is highly hygroscopic) and 10 m BMImCl/H<sub>2</sub>O (imidazolium chloride-rich mixture with about 64% in volume, Table 4–1) indicates that water does not change much the arrangement of ions in BMImCl. These results confirm that the BMImCl can stabilize water molecules at low temperatures against their crystallization. It is considered that in the “water-in-imidazolium chloride” regime, the imidazolium cations can coordinate with the water molecules, creating an energy barrier for ice nucleation. In addition, a strong interaction between the imidazolium cation and the organic ligand unit of the metal phthalocyanines is expected, leading to thermodynamic stabilization.<sup>116</sup>

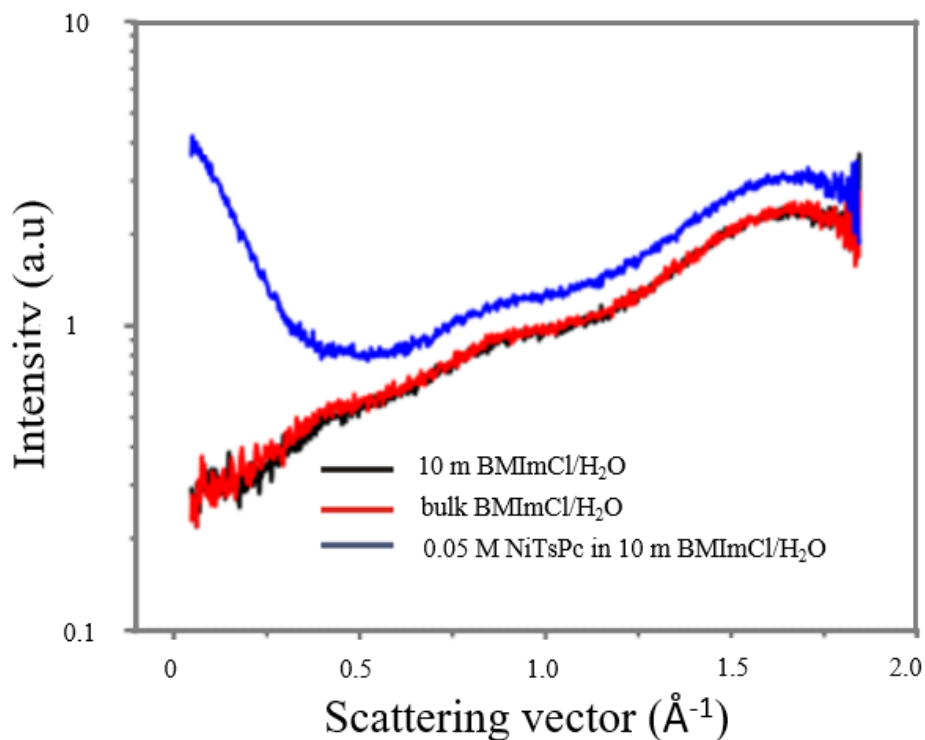


Figure 4.9 Integrated SAXS patterns collected at 20 °C for the neat BMImCl, 10 m BMImCl/H<sub>2</sub>O solution and 0.05 M NiTsPc in 10 m BMImCl/H<sub>2</sub>O solution ( $M = \text{mol L}^{-1}_{\text{solution}}$  and  $m = \text{mol L}^{-1}_{\text{solvent}}$ ).

The thermal liquidity of the aqueous supporting electrolytes (10, 20, and 30 m BMImCl/H<sub>2</sub>O) was investigated by placing electrolytes in the freezer over 24 h with an upright position at the low temperature of -32 °C. It is worth noting that those aqueous electrolytes remained at a good flowability when they were laid on the dish, as shown in Figure 4.10a. By using differential scanning calorimetry (DSC), the temperature stability window of the 10 m BMImCl/H<sub>2</sub>O supporting electrolyte was further studied in a broad temperature range from -80 to 80 °C. Figure 4.10 shows the normalized heat flow during cooling/heating. Remarkably, no resolvable endothermic and exothermic peaks can be seen over the studied temperature ranges. Such a broad temperature stability window of aqueous electrolytes has not been reported before. This is superior to that from a recent observation of aqueous saturated lithium salt solutions (about -40°C),<sup>119</sup> and also superior to those of many organic solvents (such as -43°C for diethyl carbonate,<sup>120</sup> -44°C for acetonitrile, -49°C for propylene carbonate).<sup>44</sup> The suppression

of water freezing for aqueous battery electrolytes at such a substantially low temperature can fulfill versatile purposes including aeronautics applications, defense, and transportation systems.<sup>121</sup> In addition, high-temperature operation of aqueous electrolytes is potentially safer than that of electrolytes based on organic solvents with low boiling points and high vapor pressures. Such broad temperature adaptability is favorable for practical applications with low risk of operation failure under extreme temperature conditions.<sup>122</sup>

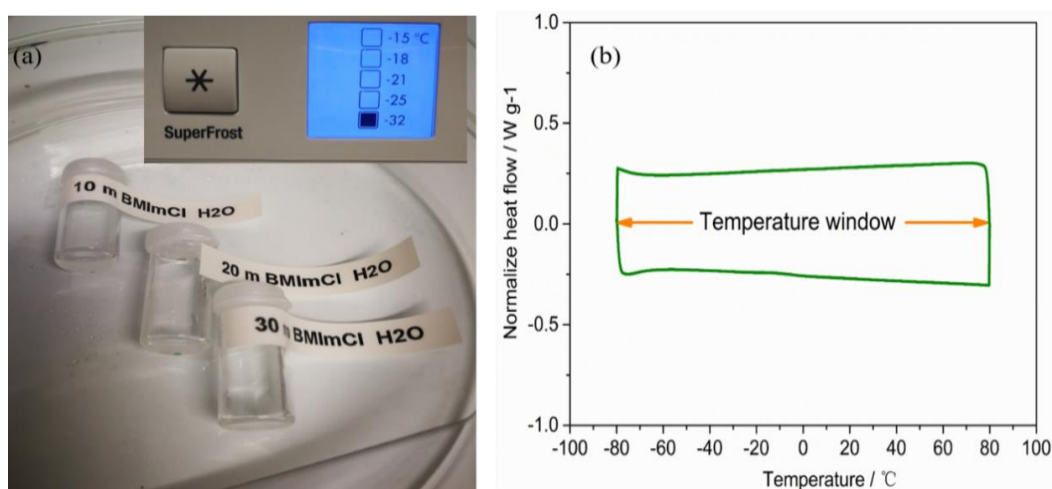


Figure 4.10 (a) Image of aqueous electrolytes laid on the dish after preserving at -32 °C over 24 h at an upright position. (b) DSC thermograms of the 10 m BMImCl/H<sub>2</sub>O aqueous electrolytes between -80 and 80 °C.

The ionic conductivity of the BMImCl/H<sub>2</sub>O mixture was measured to evaluate its suitability as supporting electrolyte from -40 to 70 °C. As shown in Figure 4.11, the ionic conductivity decreases with decreasing temperature from 114.5 mS cm<sup>-1</sup> at 70 °C to 40 mS cm<sup>-1</sup> at room temperature and then to 0.7 mS cm<sup>-1</sup> at -40 °C. These results are in accordance with the empirical law by Vogel-Fulcher-Tammann (VFT) relation (Equation 5.1).<sup>79</sup>

$$\sigma_i = \sigma_0 \exp\left(\frac{-B}{T-T_0}\right) \quad 4.1$$

Where  $\sigma_i$  ( $\text{S cm}^{-1}$ ),  $B$  (K), and  $T_0$  (K) are adjustable parameters.

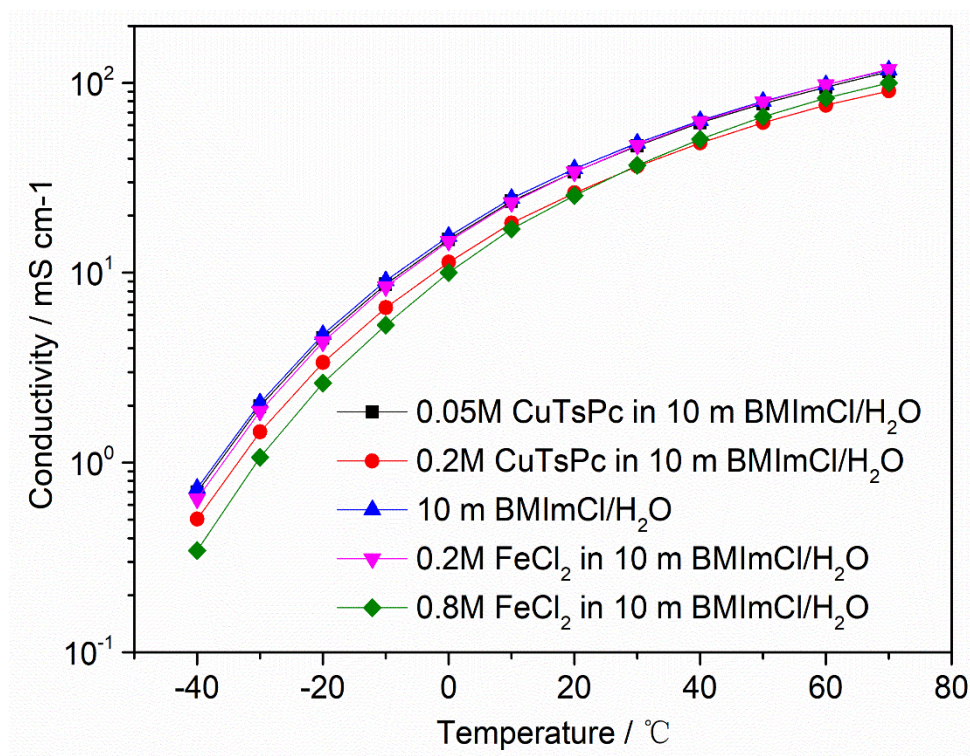


Figure 4.11 Ionic conductivity of the 10 m BMImCl/H<sub>2</sub>O solution and in the presence of active materials with different concentrations between -40 and 70°C.

Moreover, these ionic conductivity values are still much higher than those of carbonate-based electrolytes (about  $10 \text{ mS cm}^{-1}$  at room temperature, and  $0.01 \text{ mS cm}^{-1}$  at  $-40 \text{ }^\circ\text{C}$ ).<sup>44, 123</sup> After adding the active species into the 10 m BMImCl/H<sub>2</sub>O mixture, there was a slight decrease in the ionic conductivity due to the increased coulombic interactions between the electroactive materials and supporting electrolytes. At  $-40^\circ\text{C}$ , ionic conductivities of about  $0.5$  and  $0.34 \text{ mS cm}^{-1}$  can be still maintained for the  $0.2 \text{ M}$  CuTsPc anolyte and the  $0.8 \text{ M}$  FeCl<sub>2</sub> catholyte, respectively.

## 4.2.3 Electrochemical stability at wide temperature ranges

CV measurements were performed between  $-32$  and  $65$  °C using a BioLogic SP150 potentiostat/galvanostat via EC-Lab software. Figure 4.12 shows the cyclic voltammogram (CV) curves recorded at room temperature upon potentiodynamic sweeping for the 10 m BMImCl/H<sub>2</sub>O supporting electrolyte, also in the presence of the active species NiTsPc, CuTsPc and FeCl<sub>2</sub>. The supporting electrolyte of 10 m BMImCl/H<sub>2</sub>O shows an electrochemical stability window (ESW) of about 3.0 V, in which the oxidation and reduction reaction occurs nearby 1.20 V and -1.70 V vs. Ag/AgCl, respectively. Noticeably, the wide ESW effectively expand the result of conventional aqueous solutions which normally have a narrow potential window

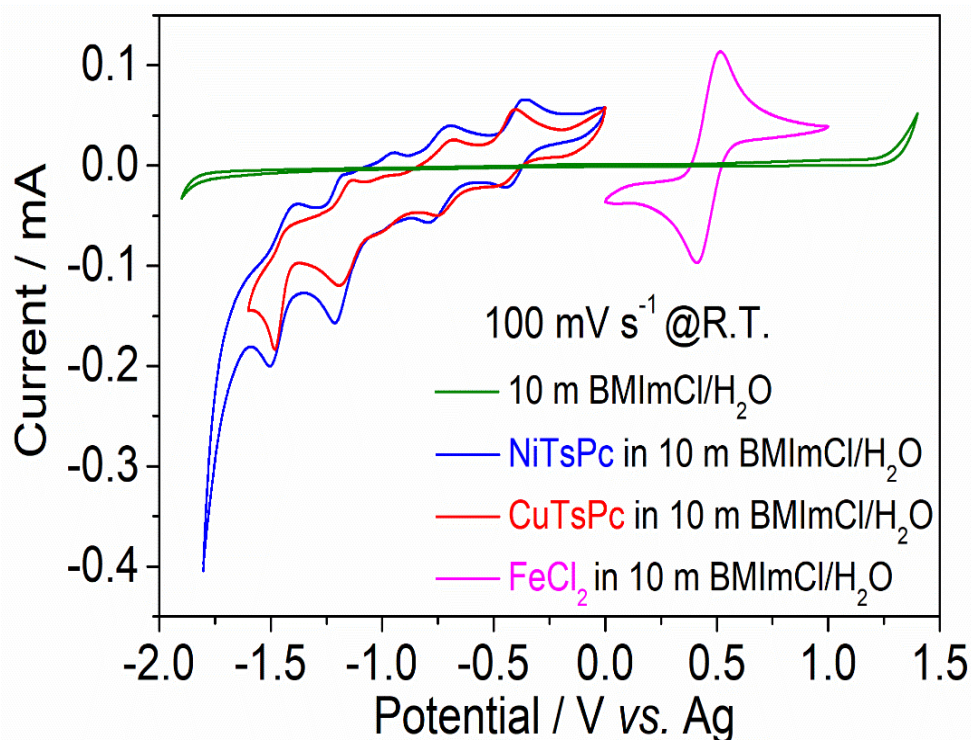


Figure 4.12 CV curves of the 10 m BMImCl/H<sub>2</sub>O, and in the presence of 10 mm NiTsPc, CuTsPc, and FeCl<sub>2</sub>, measured at room temperature and 100 mV s<sup>-1</sup>.

(1.3-1.4 V) due to the electrolysis of water.<sup>44</sup> FeCl<sub>2</sub>, which may form complex ions,

showed excellent reaction kinetics in the supporting electrolyte, with a reversible redox potential at around 0.42/0.52 V vs. Ag. The electrochemical activity of the Ni and Cu phthalocyanines is shown by a series of multiple reduction/oxidation pairs from 0 to -1.8 V vs. Ag (Figure 4.12), corresponding to the four-electron transfer reactions.

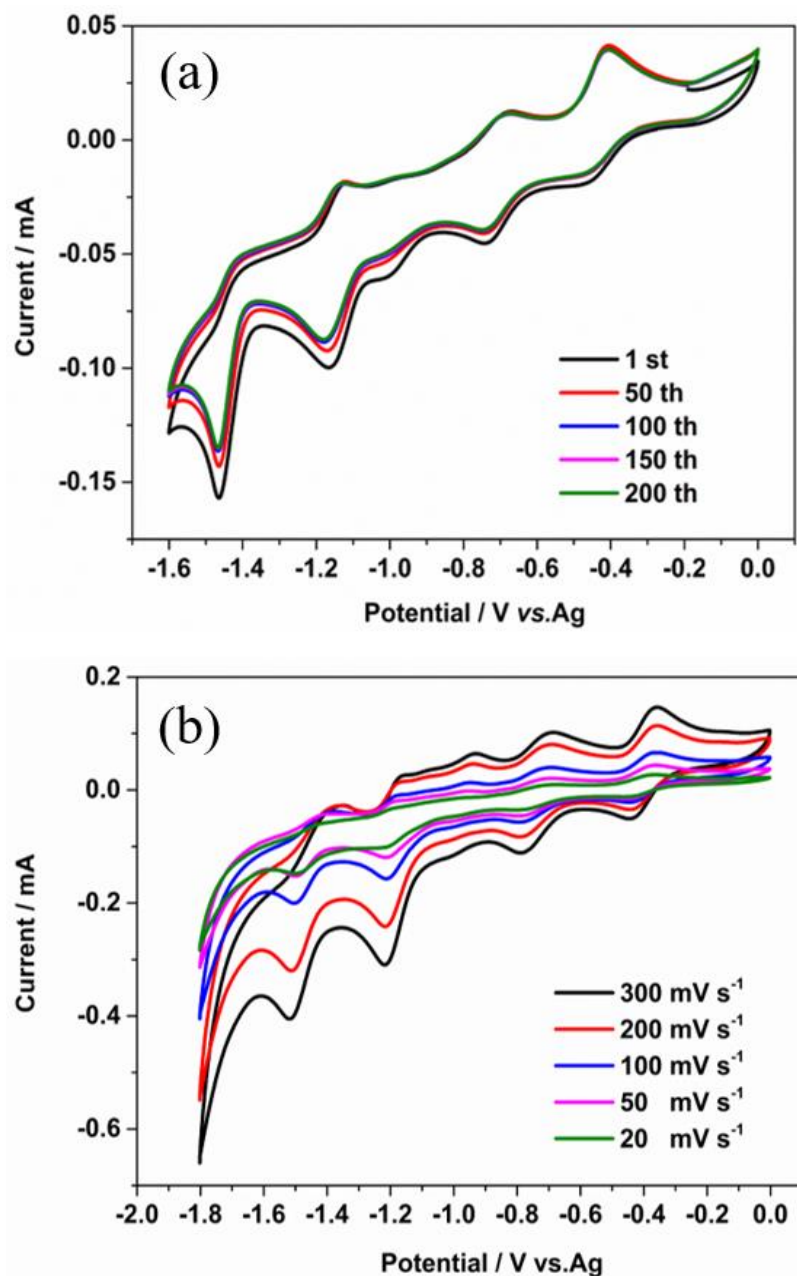


Figure 4.13 CV curves of redox species in 10 m BMImCl/H<sub>2</sub>O at room temperature. (a) 0.01 M CuTsPc for the 1<sup>st</sup>, 50<sup>th</sup>, 100<sup>th</sup>, 150<sup>th</sup>, 200<sup>th</sup> cycles at a potential sweep rate of 50 mV s<sup>-1</sup>, (b) 0.01 M NiTsPc with different scan rates.

As can be seen, these reactions occur within the electrochemical stability window of the supporting electrolyte. In addition, the CV curves of CuTsPc remained almost unchanged over 200 scans (Figure 4.13a), and NiTsPc obtained at scanning rates ranging from 20 to 300  $\text{mV s}^{-1}$  and showed well-defined oxidation and reduction peaks in the potential range of 0 V and -1.0 V (Figure 4.13b). Those observations highlight the excellent redox stability and reversibility of the employed organometallic materials.

However, such electrochemical redox peaks cannot be observed in other common aqueous solutions, such as  $\text{H}_2\text{SO}_4$ , KOH, and NaCl (Figure 4.14), exhibiting huge irreversibility.<sup>112</sup>

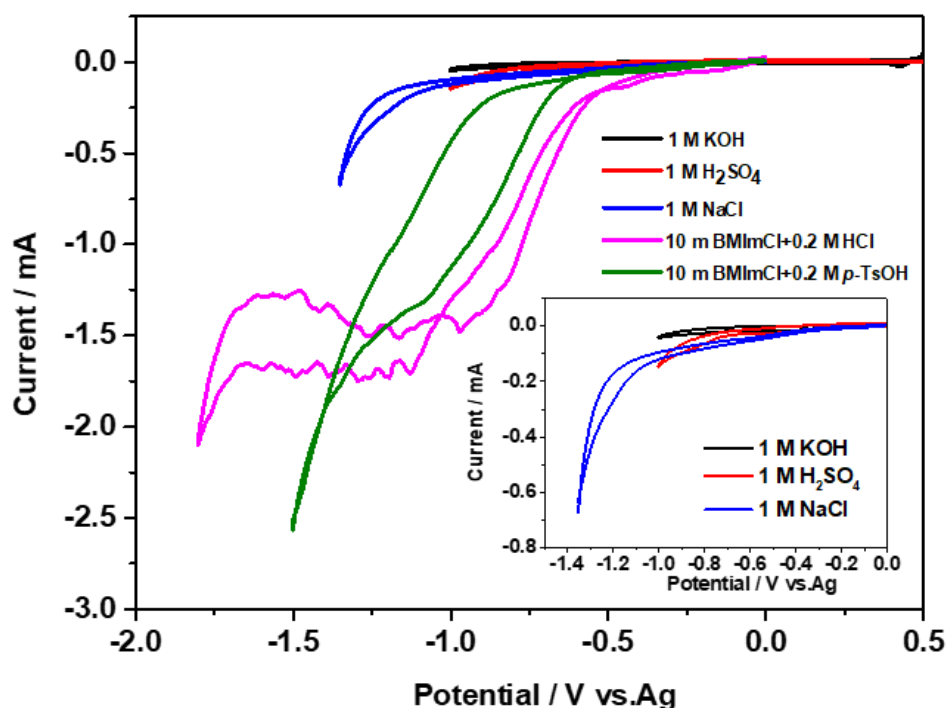


Figure 4.14 CV curves of 0.01 M NiTsPc at room temperature in common supporting electrolytes with a scan rate of 20  $\text{mV s}^{-1}$ .

In addition, the pH conditions (in the presence of minimal HCl or p-Toluenesulfonic

acid) also showed an obvious effect on the electrochemical behaviors. Hence, the aqueous ionic liquids electrolytes demonstrated the significant possibility to facilitate the electrochemical properties of the applied metal complex.

CV measurements in the broad temperature range from -32 to 65 °C were carried out for the supporting electrolyte (Figure 4.15). With decreasing temperature, the electrochemical stability window of the 10 m BMImCl/H<sub>2</sub>O widened from 2.8 V at 65 °C to 3.2 V at -32 °C (Inset in Figure 4.15). Notably, the low voltage boundary is more sensitive to the temperature decrease with a shift of about 0.3 V towards lower potentials, arising from the improved kinetic inhibition of hydrogen evolution reaction or the reduction of the BMIm<sup>+</sup> cations.

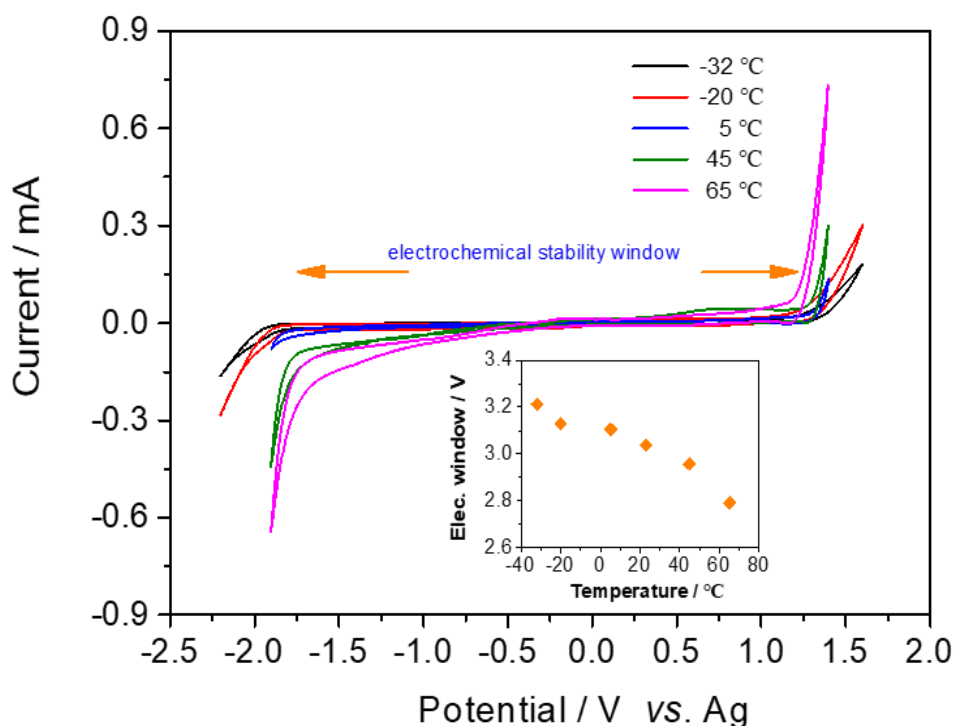


Figure 4.15 Electrochemical stability window of the 10 m BMImCl/H<sub>2</sub>O solution tested from -32 to 65 °C at 20 mV s<sup>-1</sup>. The inset shows the electrochemical stability window as a function of temperature.

In addition, the electrolytes with the electroactive materials were further studied

by CV measurements in the broad temperature range from -32 to 65 °C (Figure 4.16). Interestingly, the supporting electrolyte can still ensure the redox reactions of the catholyte and anolyte couples at various temperatures. Remarkably, the peak separations ( $\Delta E$ ) for the iron-based catholyte redox couple and the marked redox reactions of  $O_1/R_1$  and  $O_2/R_2$  for the CuTsPc anolyte are less sensitive to the temperature at a fast potential sweep rate of 100 mV s<sup>-1</sup> (inset in Figure 4.16), implying little dependence of intrinsic reaction kinetics on temperature.

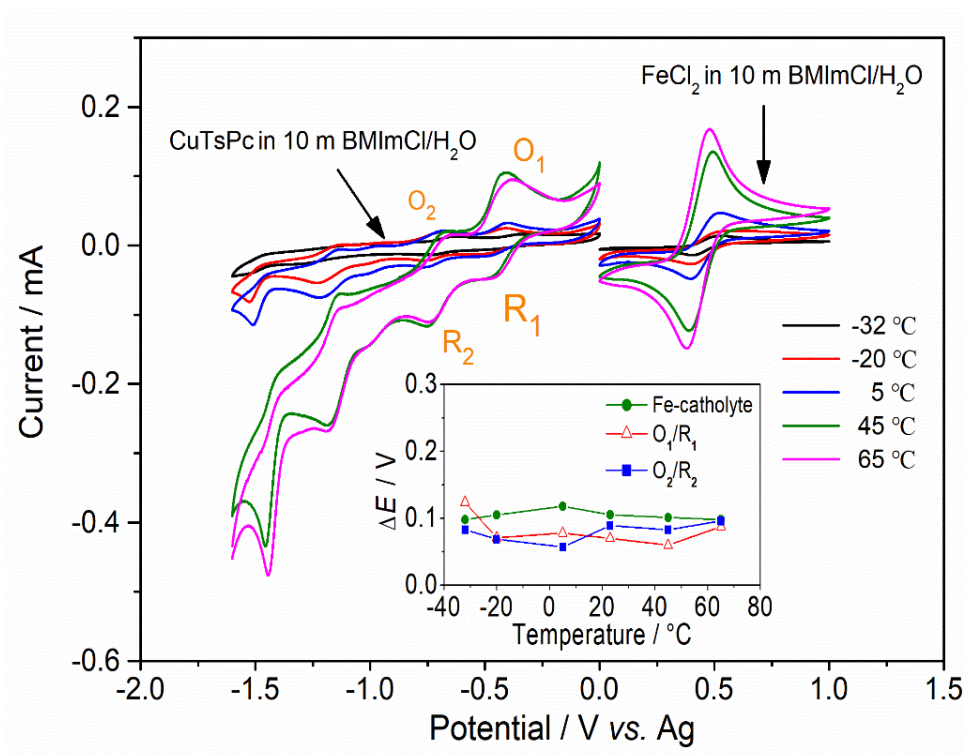


Figure 4.16 Temperature-dependent CV curves of the 10 mM active CuTsPc and FeCl<sub>2</sub> in the 10 mM BMImCl/H<sub>2</sub>O supporting electrolyte measured at 100 mV s<sup>-1</sup>. Inset shows  $\Delta E$  as a function of temperature

#### 4.2.4 Long-term performance of electrolytes at room temperature

Catholyte and anolyte in different operating temperatures were studied, as

summarized in Table 4–3. The volumetric energy density was calculated based on the volume of the catholyte compartment. The electrolytes (8 mL on each side) were circulated into the cell with an active surface area of 4 cm<sup>2</sup> by using a peristaltic pump with flow rates of 30 mL min<sup>-1</sup>. The low-temperature experiments were carried out by placing the reaction cell and electrolytes containers in a freezer. Similarly, the high-temperature experiments were performed in a temperature chamber.

As shown in Figure 4.12 and Figure 4.16, the first two-electron transfer reactions for NiTsPc and CuTsPc at around -0.45/-0.39 V and -0.77/-0.67 V are highly reversible, corresponding to the  $\text{Me}^{\text{II}}\text{TsPc}^{4-} \rightleftharpoons \text{Me}^{\text{II}}\text{TsPc}^{5-} \rightleftharpoons \text{Me}^{\text{II}}\text{TsPc}^{6-}$ .<sup>124</sup> Nevertheless, further reduction of these compounds to -1.2 and -1.48 V showed poor reversibility.

Table 4–3 Properties of studied electrolytes for flow cell tests

	cells	Catholyte			Anolyte		
		concentration of redox-active materials	supporting electrolyte	volume	concentration of redox-active materials	supporting electrolyte	volume
Room temperature	(i)	0.03 M FeCl <sub>2</sub>	10 m BMImCl/H <sub>2</sub> O	8 mL	7.5 mM CuTsPc	10 m BMImCl/H <sub>2</sub> O	8 mL
	(ii)	0.2 M FeCl <sub>2</sub>			50 mM NiTsPc		
		0.8 M FeCl <sub>2</sub>			200 mM CuTsPc		
Robust temperatures	(i)	0.2 M FeCl <sub>2</sub>	10 m BMImCl/H <sub>2</sub> O	8 mL	50 mM NiTsPc	10 m BMImCl/H <sub>2</sub> O	8 mL

In order to establish a suitable operating voltage range for these positive and negative redox materials, flow cell tests were carried out using two different cutoff charge voltages of 1.85 and 1.4 V, and a cross-linked methylated polybenzimidazole (PBI) based Cl<sup>-</sup>-exchange membrane (Figure 4.17a).<sup>125</sup> With a cutoff of 1.85 V, the

charge/discharge plateaus can be clearly seen, in consistence with the CV data. However, the fast capacity fade was observed (Figure 4.17b). Therefore, the four-electron utilization measurements were abandoned. Other complexes with better electrochemical reversibility and membranes with better ionic conductivities should be surveyed in the future.

Interestingly, by setting the cutoff to 1.4 V, thus utilizing the two-electron reaction of the anolyte (7.5 mM CuTsPc in 10 m BMImCl/H<sub>2</sub>O), the flow cell showed stable capacity retention over 100 cycles (with a fading rate of 0.09% per cycle) at room temperature and 2.5 mA cm<sup>-2</sup>. The Coulombic, voltage, and energy efficiencies were about 96%, 88% and 84%, respectively (Figure 4.17c). The dependence of the CE on the cut off voltages indicates a poor electrochemical reversibility at deep reduction of the MeTsPc species. The used anolyte and catholyte after 100 cycles were collected for CV measurements in a broad potential range (Figure 4.17d). No redox peaks from Fe and CuTsPc were seen in the anolyte and catholyte, respectively, indicating that the PBI membrane can effectively prevent the cross-mixing of these active species.

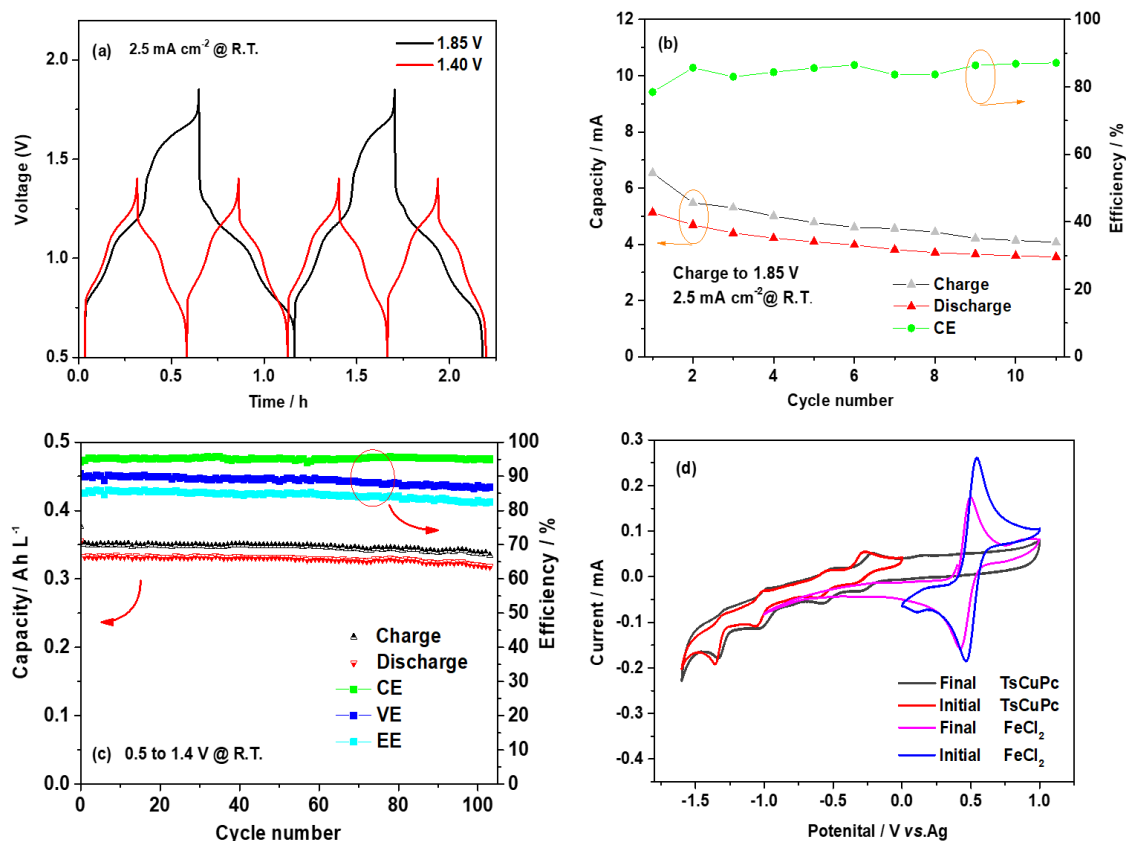


Figure 4.17 Electrochemical performance of flow cells using 10 m BMImCl/H<sub>2</sub>O supporting electrolyte. (a) Voltage profiles of a CuTsPc (7.5 mM)/FeCl<sub>2</sub> (0.03 M) flow cell measured at room temperature and 2.5 mA cm<sup>-2</sup> with different cutoff charge voltages and (b) Capacity fading of the flow cell with a cutoff charge voltage of 1.85 V at 2.5 mA cm<sup>-2</sup> and room temperature. (c) The corresponding cycling stability over 100 cycles tested between 0.5 and 1.4 V. (c) CV curves of the used anolyte and catholyte after 100 charge/discharge cycles at scan rate of 100 mV s<sup>-1</sup>.

When using a 50 mM NiTsPc anolyte (theoretical capacity of 2.68 Ah L<sup>-1</sup>, based on a two-electron reaction), steady Coulombic, voltage, and energy efficiencies of 95.8%, 91.9%, and 88.0%, respectively, were observed at 5 mA cm<sup>-2</sup> (Figure 4.18a). An electrolyte utilization ratio of 76.8% was observed, compared to that of 82.1% with 7.5 mM CuTsPc anolyte at 2.5 mA cm<sup>-2</sup>. In addition, it was observed that the capacity

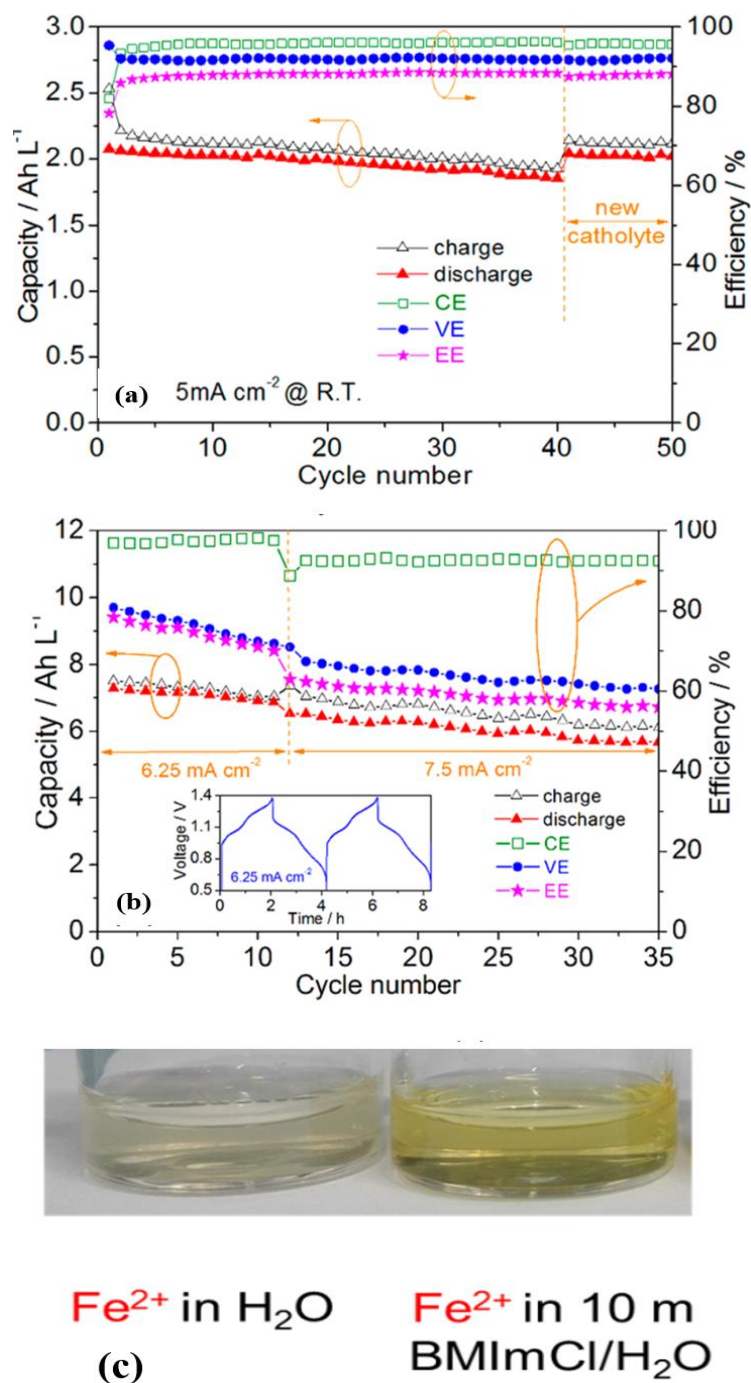


Figure 4.18 (a) Cycling performance of NiTsPc (50 mM)/FeCl<sub>2</sub> (0.2 M) flow cell measured between 0.5 and 1.4 V at 5.0 mA cm<sup>-2</sup>; after 40 cycles, the catholyte was replaced with fresh electrolyte containing 0.2 M HCl. (b) Cycling performance of a CuTsPc (0.2 M)/FeCl<sub>2</sub> (0.8 M) flow cell at room temperature. Inset shows the voltage profile at 6.5 mA cm<sup>-2</sup>. (c) Photos of 0.1 M FeCl<sub>2</sub>·4H<sub>2</sub>O in pure water, and 10 m BMImCl/H<sub>2</sub>O

decays over the first 40 cycles (0.27% per cycle) was connected with the development

of turbidity in the catholyte, which can be however recovered upon replacing the catholyte with a fresh solution containing 0.2 M HCl. Nevertheless, we have found that the iron species can be better stabilized in the 10 m BMImCl/H<sub>2</sub>O (Figure 4.18c) than in neat water. Hence, it is considered that parasitic side reactions of the iron species occurred,<sup>126</sup> leading to an inevitable loss of the active species. For the flow cell with a relatively high concentration of 0.2 M CuTsPc, an initial discharge capacity of about 7.2 Ah L<sup>-1</sup> and a high CE of about 96% have been observed (Figure 4.18b). Such an easily accessible high capacity of the metal complex in aqueous electrolytes is superior to that in typical nonaqueous electrolyte systems.

#### 4.2.5 Long term cycling performance at robust temperatures

At -20 and -32 °C, the flow cell showed steady cycling efficiencies (Figure 4.19a). At these low temperatures, a Coulombic efficiency of about 95% was observed, which is close to that tested at room temperature. However, voltage efficiencies of about 73.0% and 72.1% can be still observed at -20 and -32 °C, respectively, compared to that of about 92% at room temperature. In addition, the electrolyte utilization at -20 and -32 °C remains about 59% and 51%, respectively, in comparison to about 82% at room temperature. Such a temperature dependence of capacity retention is much better than that for non-aqueous electrolytes-based RFBs.<sup>72</sup> At -32°C, a relatively fast capacity fade of about 0.8% per cycle was observed. When operating at sub-zero temperatures, a change in the ion channels, swelling and mechanical properties of the employed membrane could occur, and eventually causes an increase in cross-mixing level.

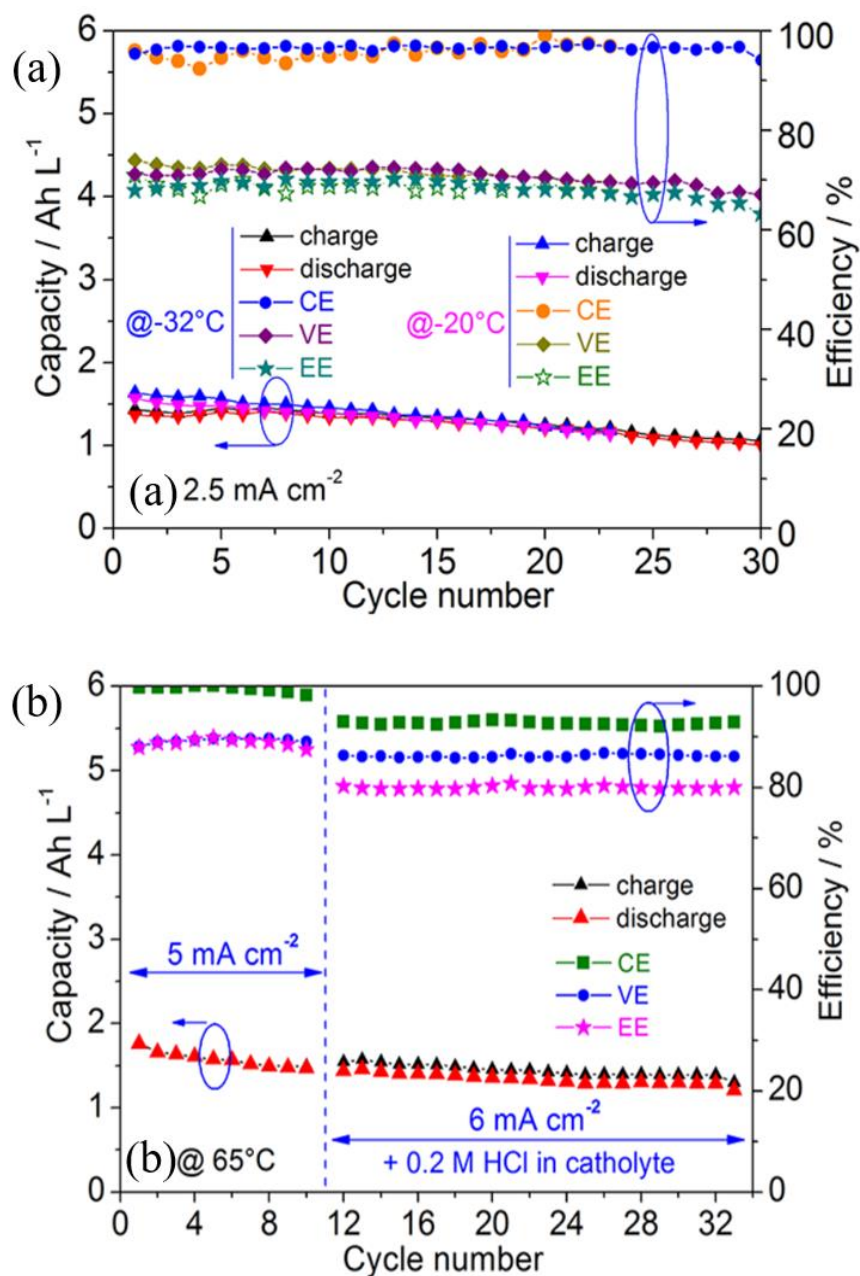


Figure 4.19 Cycling performance of a NiTsPc (0.05 M)/FeCl<sub>2</sub> (0.2 M) flow cell measured: (a) at -32 and -20 °C , 2.5 mA cm<sup>-2</sup> , and (b) at 65 °C and increased current densities. After 10 cycles, 0.2 M HCl was added into the catholyte in the cycling solution.

When tested at 65 °C, a high Coulombic efficiency of 99.6% was observed (Figure 4.19b). After 10 cycles, the addition of HCl into the catholyte leads to a decrease in the subsequent Coulombic and voltage efficiencies. In addition, the capacity fading can be hindered. It is well known that the PBI membrane is capable of absorbing acid molecules upon exposure to the HCl additive,<sup>127</sup> which will induce a change in the ion transport channel, and thereby the Coulombic efficiency. Since the PBI-based membrane used in this work is not fully methylated, it still has some repeat units with basic nitrogen groups which should actively interact with HCl, inducing some slight pH dependence of the membrane. Nevertheless, these steady operating efficiencies observed at both low and high temperatures verify the excellent temperature adaptability of the system.

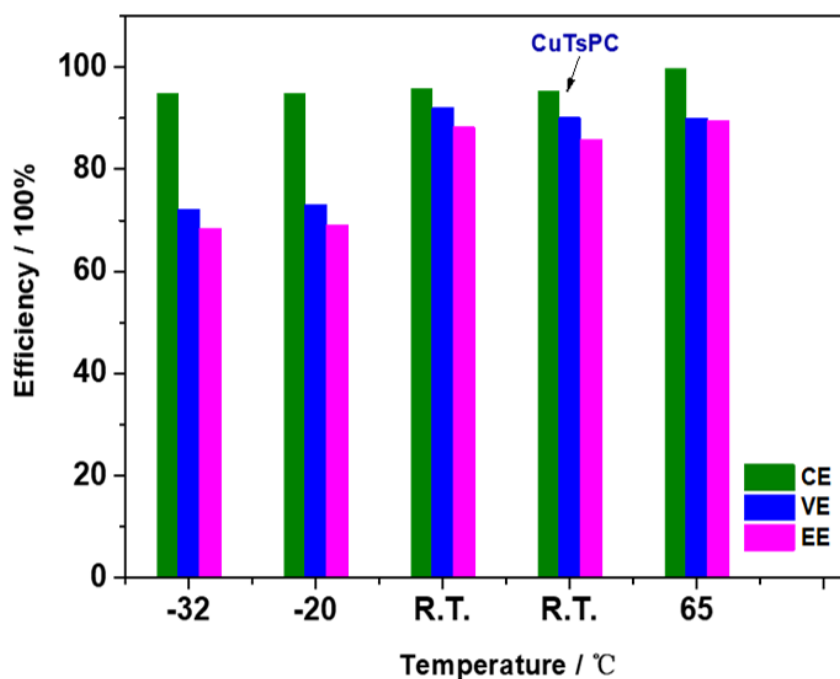


Figure 4.20 Comparison of the electrochemical efficiencies of NiTsPc and CuTsPc (arrow marked) at different temperatures.

Table 4–4 Summary of the electrochemical efficiencies at different temperatures.

Electroactive materials	Temperature	CE / %	VE / %	EE / %
NiTsPc	-32 °C	94.9	72.1	68.4
	-20 °C	94.8	73.0	69.2
	R.T.	95.8	92	88.3
	65 °C	99.6	90	89.6
CuTsPc	R.T.	95.2	90.1	85.8

Figure 4.20 and Table 4–4 compares the electrochemical efficiencies of the assembled flow cell under different operating temperatures. As the temperature increasing from -32 to R.T., the flow cells showed steady Columbic efficiency of around 95%, demonstrating good reaction kinetics of active species against low temperatures. The higher temperature is beneficial for facilitating the reaction rates, which showed a Columbic efficiency of around 99.6% at 65 °C. The comparative lower VE at temperatures of -32 and -20 °C may be attributed to the decreasing ionic conductivities of the membrane.

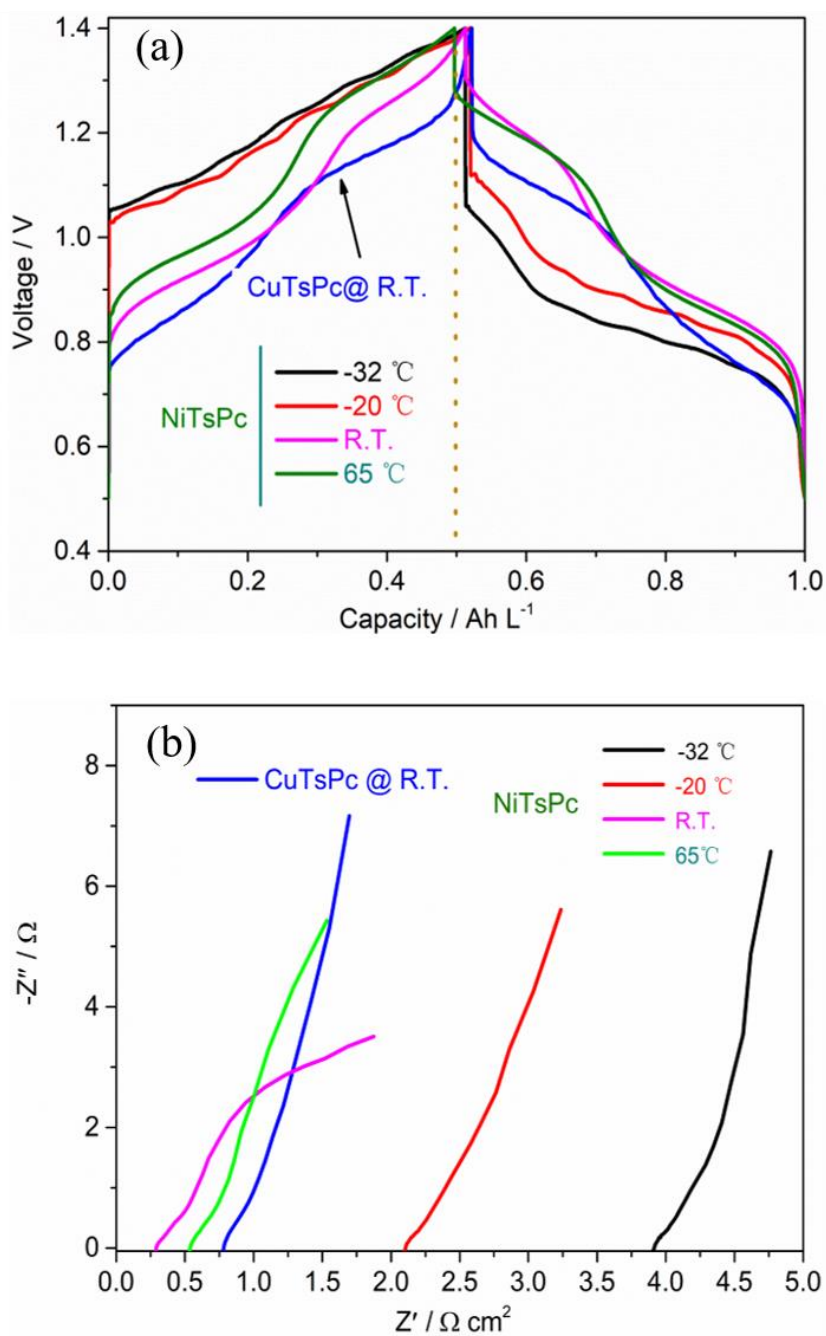


Figure 4.21 (a) Normalized temperature-dependent voltage-capacity profiles, and (b) the electrochemical impedance spectrum of the flow cell using with PBI membrane at different temperature.

Figure 4.21a shows the normalized voltage profiles of the NiTsPc and CuTsPc analytes against the iron cathodic couple tested from -32 to 65 °C. As the temperature decreased, the two-step slopes in the charge/discharge curves are less resolved with an

increase in polarization, which may arise from the reduced ion conductivity of the membrane. For the Ni species, the two charge/discharge slopes appeared at slightly higher voltages compared to the Cu counterpart. The difference in the redox potential of the active sites of the phthalocyanine ring is related to the identity of the central metal, and the length and the strength of the metal-ligand bonding.<sup>128</sup>

The Nyquist plot of the flow cell at different temperatures is shown in Figure 4.21b. The internal cell resistance ( $R_s$ ), observed from electrochemical impedance spectroscopy, was increased from about  $0.3 \Omega \text{ cm}^2$  at room temperature to  $3.8 \Omega \text{ cm}^2$  at  $-32 \text{ }^\circ\text{C}$  due to the loss of activity of the electrolytes and the reduced ionic conductivity of membrane, which is in accordance with the cycling test results. The result is similar to a previous observation using saturated aqueous LiCl,<sup>119</sup> but less severe compared to organic solvent-based electrolytes.<sup>120</sup>

---

### 4.3 Aqueous ionic liquid electrolytes for all organic RFB

This chapter is predominantly based on the following publication:

**Z. Huang**, C. Kay, B. Kuttich, D. Rauber, T. Kraus, H. Li, S. Kim, R. Chen, An “interaction-mediating” strategy towards enhanced solubility and redox properties of organics for aqueous flow batteries. *Nano Energy*, 69, 104464 (2020), Copyright 2020 Elsevier Ltd. DoI: [10.1016/j.nanoen.2020.104464](https://doi.org/10.1016/j.nanoen.2020.104464).

#### 4.3.1 Motivation

Aqueous redox flow batteries using electroactive organic materials are currently attracting significant attention. However, the commonly used conducting ions in aqueous electrolytes, such as  $H^+$ ,  $Na^+$ ,  $K^+$ ,  $OH^-$  and  $Cl^-$  etc. hardly affect the solubility and especially the electrochemical properties of organic materials. To date, a rational selection of pH-neutral supporting electrolytes for promoting the physiochemical and electrochemical performance of organic materials has only rarely been explored. An ideal conducting ionic species in electrolytes should have high ionic conductivity, low viscosity, and importantly impose strong interactions on the organic solutes.<sup>34</sup> Therefore, the influence of supporting electrolytes on aqueous solubility, electrochemical reversibility, and chemical stability of the organic components has to be addressed. Inspired by the powerful dissolution capability of imidazolium chlorides to organic compounds and polymers,<sup>52</sup> and our previous work for using “water-in-ionic liquids” to obtain broad electrochemical and temperature stability of aqueous electrolytes,<sup>83, 89, 129</sup> herein a new electrolyte design strategy towards enhanced solubility and chemical stability of active materials is proposed which utilizes interaction-mediating species.

In this chapter, two well established commercial organic materials, 4-hydroxy-2,2,6,6-tetramethylpiperidine 1-oxyl (4-OH-TEMPO) and methyl viologen dichloride (MV), were selected as model compounds without further chemical modification. A 3 molality aqueous imidazolium chloride, with high ionic conductivity and water like flowability, enables a record aqueous solubility of 4.3 M for 4-OH-TEMPO and reversible two-electron reaction of unmodified MV at moderate concentrations. The all-organic 4-OH-TEMPO/MV flow cell shows two pairs of well-defined charge/discharge plateaus with good Columbic efficiency. At the higher concentration measurements, the flow cell shows remarkable chemical stability of the nitroxyl radical, i.e., excellent cycling stability over long cycles. Furthermore, the 4-OH-TEMPO catholyte with a concentration of 3 M is tested in a flow cell, which maintains impressive steady energy efficiency.

#### 4.3.2 Solubility of redox-active electrolytes

As studied in previous works, the energy density of an RFB is proportional to the concentration of the redox-active materials. Nevertheless, most of the pristine organics exhibit only low solubility in the supporting electrolytes. Up to now, novel electrolyte designs for the improvement of concentration of electroactive materials mainly rely on the rational molecular engineering method. Functional groups such as sulfonic acid,<sup>30</sup> hydroxyls,<sup>38</sup> and quaternary ammonium were generally attached to the molecular chain, thus increasing the intermolecular interactions between solutes and the polar solvents. Figure 4.22 compares the equivalent electron concentration, namely, the maximum concentration of organic molecules multiplied by the number of electrons transferred, of several representative organic compounds that have been studied in aqueous RFBs (Table 4–5).

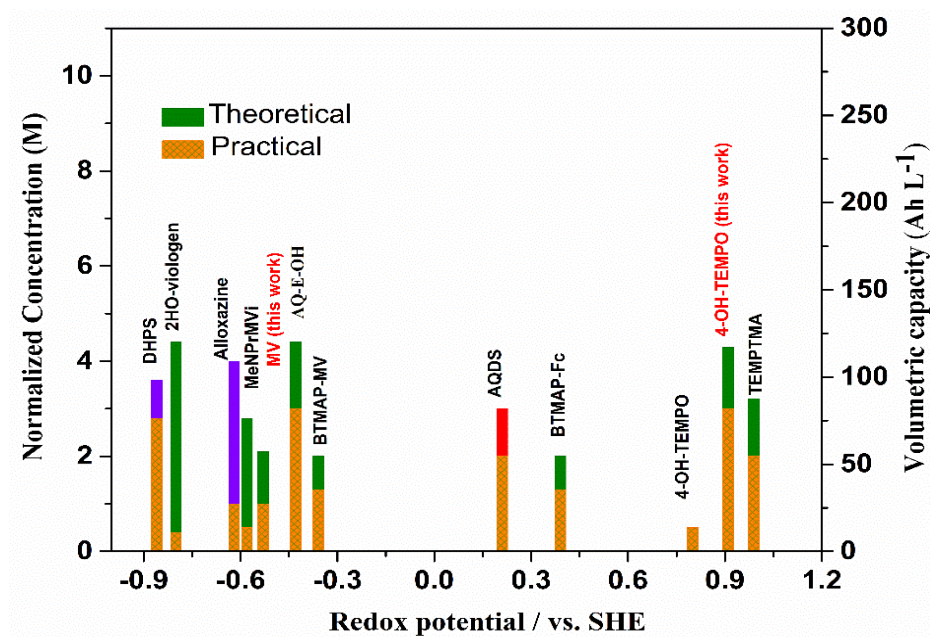
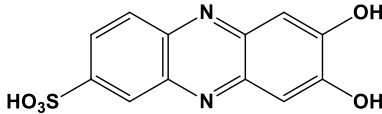
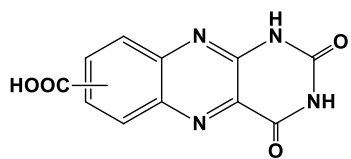
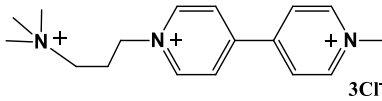
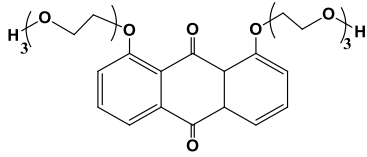
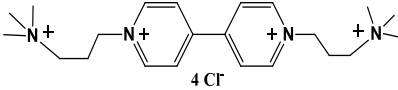
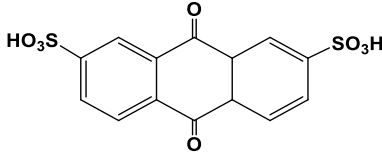
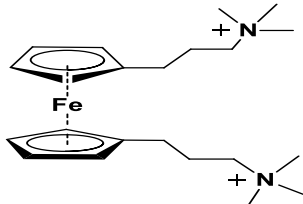
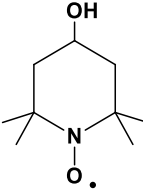
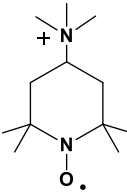


Figure 4.22 Comparison of the equivalent electron concentration and volumetric capacity of representative organic molecules for aqueous RFBs. The color of red, green, and purple represents acidic, neutral, and basic media, respectively.

Table 4-5 Lists of the corresponding results of the organic materials in aqueous RFBs.

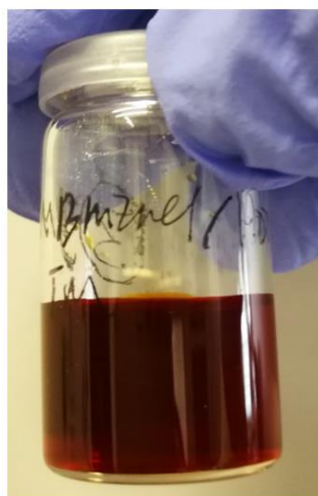
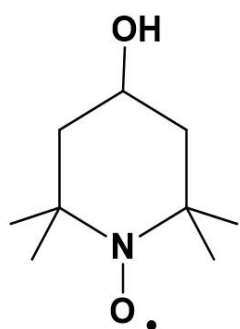
Selected organic species	Abbreviation	Supporting electrolyte	Redox potential / V	Practical / Theoretical maximum concentration	Ref.
	DHPS	1 M NaOH	-0.86	1.4 M / 1.8 M	34
	2HO-viologen	1.0 M NaCl	-0.80	0.2 M / 2.0 M	130
	Alloxazine	1.0 M KOH	-0.62	0.5 M / 2.0 M	35

### 4.3 Aqueous ionic liquid electrolytes for all organic RFB

	MeNPrMV	2.0 M NaCl	-0.58	0.25 M / 1.4 M	131
	AQ-E-OH	2.0 M NaCl	-0.84	0.2 M / 2.0 M	132
	BTMAP-MV	2.0 M NaCl	-0.36	1.3 M / 2.0 M	133
	AQDS	1.0 M H <sub>2</sub> SO <sub>4</sub>	0.21	1.0 M / 1.5 M	30
	BTMAP-Fc	2.0 M NaCl	0.39	1.3 M / 1.9 M	133
	4-OH- TEMPO	1.5 M NaCl	0.79	0.5 M / 0.5 M	31
	TEMPMA	1.5 M NaCl	0.99	2.0 M / 3.2 M	40

For the first time, we apply ionic liquid containing supporting electrolyte for tailoring the properties of redox-active organic materials. In our proposed aqueous ionic

liquid supporting electrolytes, the MV and 4-OH-TEMPO showed extremely high solubility of 2.2 M (which is about 2 M in 2 M NaCl) and 4.3 M in 3 m aqueous imidazolium chloride (Figure 4.23), respectively. Two imidazolium groups with a slightly different side-chain length of 1-butyl-3-methylimidazolium chloride (BMImCl) and 1-ethyl-3-methylimidazolium chloride (EMImCl) were used for comparative purposes.



### 4.3 M 4-OH-TEMPO

Figure 4.23 Molecular structure of studied 4-OH-TEMPO and photograph of a solution containing 4.3 M 4-OH-TEMPO in 3 m BMImCl/H<sub>2</sub>O at room temperature.

As compared to the results in Table 4–5, the aqueous solubility of 4.3 M for 4-OH-TEMPO is among the best of all the aqueous catholytes reported for RFBs. This leads to a theoretical volumetric capacity of 115 Ah L<sup>-1</sup> with a one-electron transfer reaction, which is about eight times more than that in aqueous NaCl supporting electrolyte (a solubility of only 0.5 M in 1.5 M NaCl).<sup>134</sup> Note that in pure water, 4-OH-TEMPO has a solubility of 2.1 M.<sup>31</sup> Our approach is distinct from previous work that solubility enhancement is exclusively achieved by chemically grafting functional groups to organic motifs.

### 4.3.3 EPR analysis of the interaction mechanism

To obtain a deeper understanding of the intermolecular interaction between the imidazolium ring from the ionic liquids and the organic solutes, we performed electron paramagnetic resonance (EPR) spectroscopy experiments on two series of solutions containing different radical concentrations in 3 and 10 m BMImCl/H<sub>2</sub>O (Figure 4.24). EPR is sensitive to probe the averaged magnetic interactions and the motion of radicals in solution, and therefore can be used to clarify the concentration-dependent molecular dynamics and the molecular environment in the ternary water/imidazolium/nitroxyl radical system. At lower concentrations (< 0.1 M), three reasonably narrow hyperfine lines were observed, indicating that the radicals are highly mobile and not aggregated. As the concentration increases the three lines initially coalesce into a single broad line, which then narrows at the highest concentration. This behavior is typical of enhanced magnetic interactions, e.g. exchange interaction at high concentrations of paramagnetic species. The 10 m series is slightly narrower than the 3 m series, illustrating how the increasing amount of BMImCl keeps the 4-OH-TEMPO radicals apart.

We conclude that the interaction between the constituent ions of the ionic liquid and the organic radicals (as illustrated in Figure 4.25) is stronger than the lattice energy of 4-OH-TEMPO itself, thereby increasing its solubility in electrolytes. In addition, by isolating the 4-OH-TEMPO molecules from each other, the imidazolium cations may also help to stabilize them from collision-caused structural decomposition.<sup>133, 135</sup>

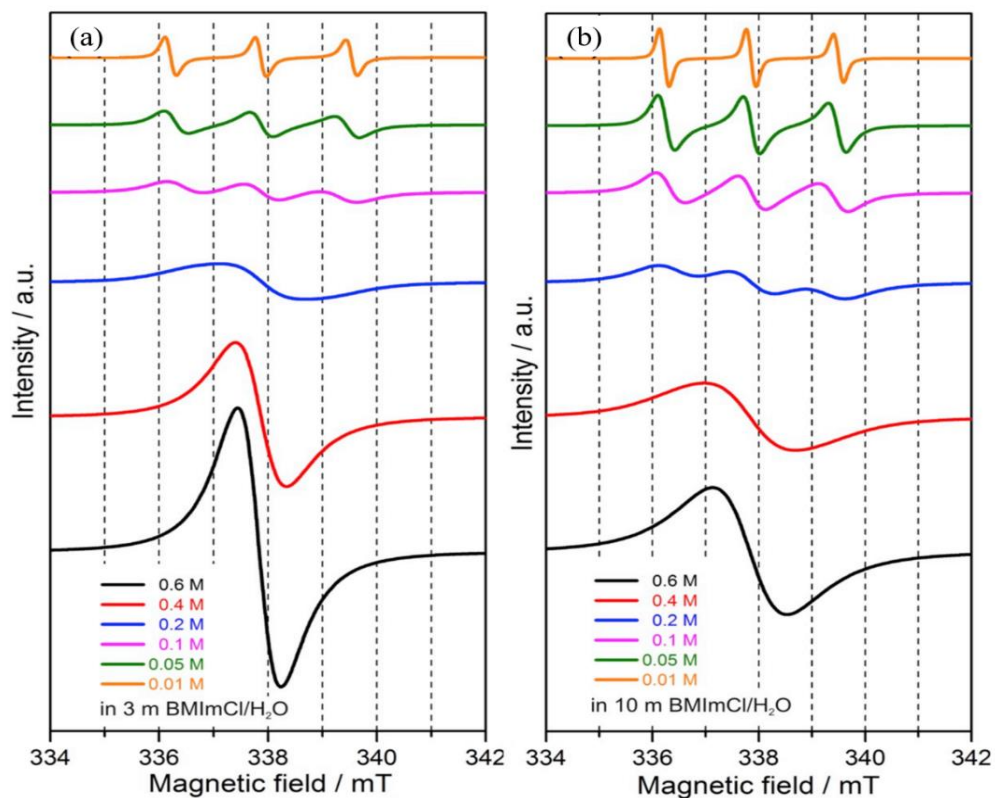


Figure 4.24 EPR spectra of 4-OH-TEMPO with different concentrations in (a) 3 m and (b) 10 m BMImCl/H<sub>2</sub>O.

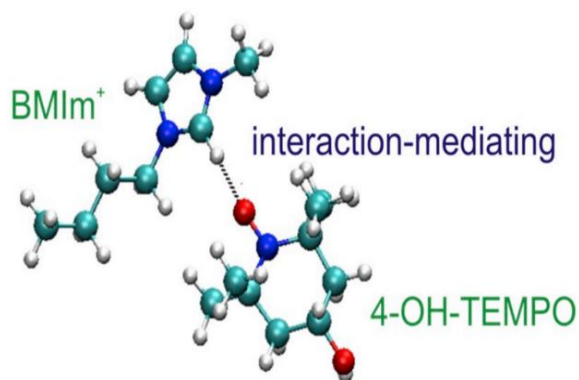


Figure 4.25 Schematic illustration of the interactions between the imidazolium group and the organic solute.

## 4.3.4 Electrochemical properties of electrolytes

The influence of the supporting electrolytes on the electrochemical redox properties of 4-OH-TEMPO and MV was studied by cyclic voltammetry (CV) experiments (Figure 4.26). By using conventional aqueous NaCl for comparison, a distinct electrochemical behavior of both organic compounds was observed when tested in our supporting electrolytes. In aqueous NaCl (Figure 4.26, dashed line), 4-OH-TEMPO exhibited a pair of redox peaks at half-wave redox potential ( $E_{1/2}$ ) of 0.58 V vs. Ag. On the other hand, MV exhibited a redox reaction at -0.71 V vs. Ag corresponding to the  $MV^{2+}/MV^{+}$  couple. However, the second reduction process of  $MV^{+}/MV^0$  showed poor reversibility, consistent with previous observations.<sup>31, 42, 134</sup> In contrast, in 3 m BMImCl/H<sub>2</sub>O (Figure 4.26, solid line), 4-OH-TEMPO showed a higher  $E_{1/2}$  of 0.71 V vs. Ag, corresponding to a positive shift of the redox potential of +0.13 V for the oxoammonium /nitroxyl radical couple (Figure 4.26), which is beneficial for a higher overall cell voltage. Interestingly, the MV underwent two consecutive and reversible electron transfer reductions in 3 m BMImCl/H<sub>2</sub>O at redox potentials of -0.54 V vs. Ag ( $MV^{2+}/MV^{+}$ ) and -0.90 V vs. Ag ( $MV^{+}/MV^0$ ). Figure 4.26b shows the reaction mechanism of the redox-active materials in the supporting electrolytes. Note that the two-electron utilization of MV in aqueous electrolytes has been only recently obtained by introducing ammonium functional end groups.<sup>131</sup>

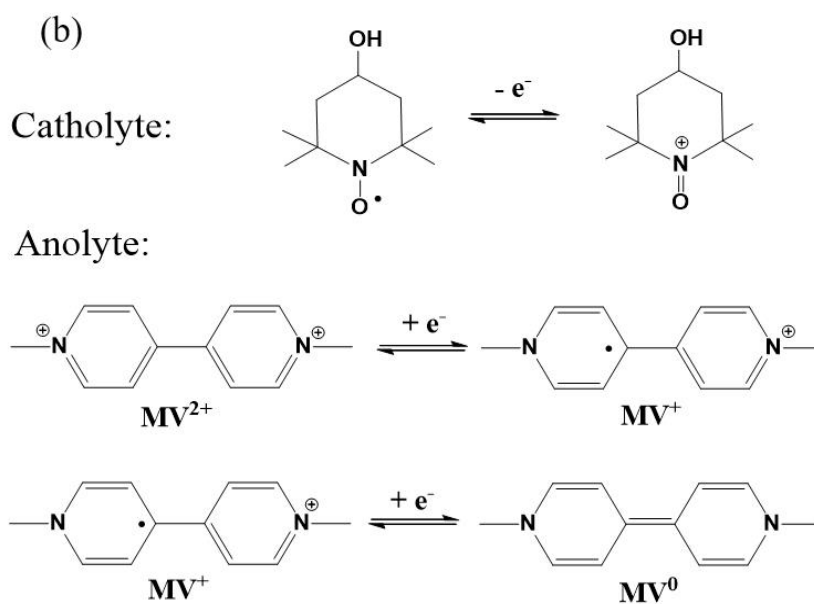
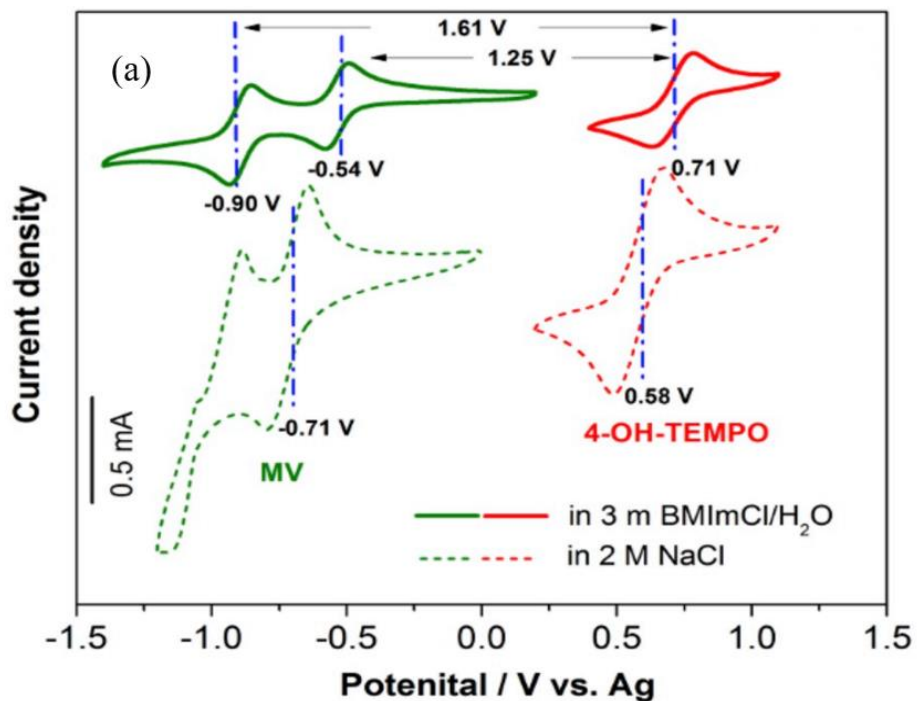


Figure 4.26 (a) CV curves of MV and 4-OH-TEMPO (7 mM for both) in different supporting electrolytes of 3 m BMImCl/H<sub>2</sub>O (solid line) and 2 M NaCl (dashed line) at 100 mV s<sup>-1</sup>. (b) redox reaction mechanism of 4-OH-TEMPO and MV.

Furthermore, CV experiments with variable potential scan rates were performed to study the electrochemical response of both organic materials in 3 m BMImCl/H<sub>2</sub>O

(Figure 4.27). From 10 to 300  $\text{mV s}^{-1}$ , both materials showed reversible redox peaks and narrow peak separation, indicating a fast reaction rate. A linear relationship between the peak current and the square root of the scan rate was observed for the one-electron reaction of 4-OH-TEMPO and the two-electron reaction of MV, suggesting diffusion-controlled processes.

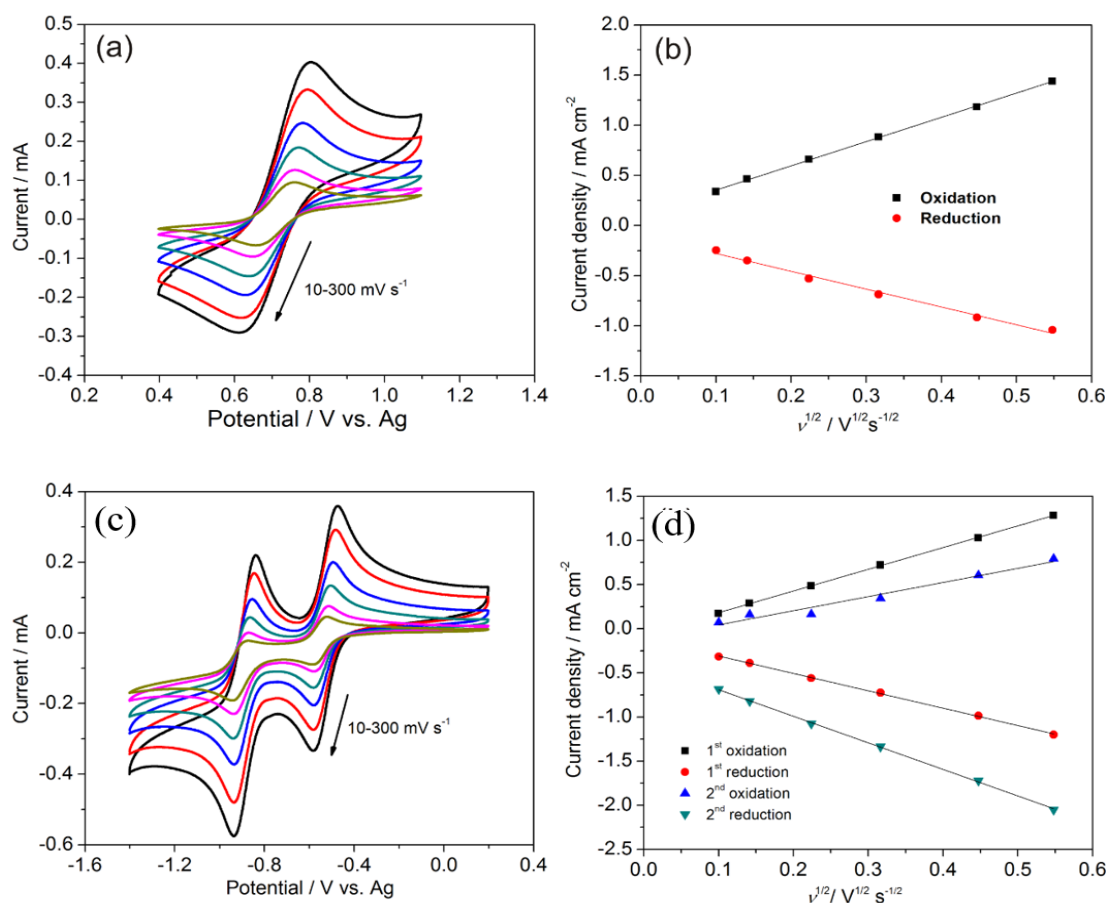


Figure 4.27 CV of 7.5 mM 4-OH-TEMPO (a) and 7.5 mM MV (c) in 3 m BMImCl/H<sub>2</sub>O at potential sweep rates of 10, 20, 50, 100, 200, and 300  $\text{mV s}^{-1}$ . (b) and (d) the corresponding linear relationship between the peak current density and the square root of the potential sweep rates.

In order to determine the chemical diffusion coefficients for both materials, linear sweep voltammetry (LSV) with a rotating disk electrode (RDE) with rotation rates ranging from 300 to 2100 rpm was carried out (Figure 4.28). MV underwent two-step redox reactions and 4-OH-TEMPO showed a one-electron redox reaction, in agreement

with the CV results. The diffusion coefficient of 4-OH-TEMPO was calculated as  $5.31 \times 10^{-6} \text{ cm}^2 \text{ s}^{-1}$  from the slope of the linearly fitted Levich plot. On the other hand, the diffusion coefficients were  $7.83 \times 10^{-6}$  and  $8.81 \times 10^{-6} \text{ cm}^2 \text{ s}^{-1}$  for the 1<sup>st</sup> and 2<sup>nd</sup> reduction reaction of MV, respectively. Such values are comparable or higher than those for some redox-active molecules determined in acidic solutions.<sup>30, 38, 130, 136-138</sup>

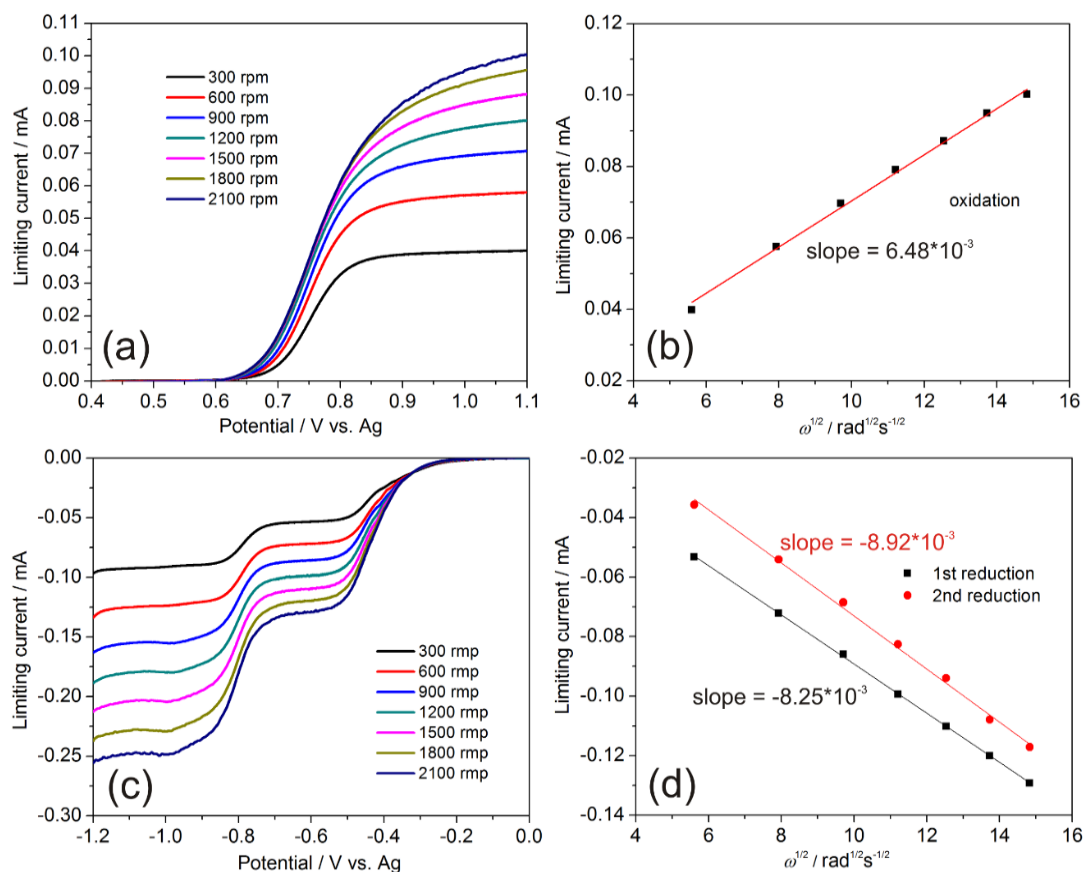


Figure 4.28 LSV curves of (a) 4-OH-TEMPO and (c) MV (1 mM in 3 m BMImCl/H<sub>2</sub>O) at a scan rate of  $5 \text{ mV s}^{-1}$ , and (b) and (d) the corresponding Levich plots, respectively. For MV, two steps of redox reactions ( $\text{MV}^{2+}/\text{MV}^{+}$  and  $\text{MV}^{+}/\text{MV}^0$ ) were identified.

#### 4.3.5 Long-term stability with multi-electron transition reaction

Catholyte and anolyte in different operating temperatures were studied, as summarized in Table 4–6. For the high-temperature measurements, the electrolytes

were heated in an oil bath and then delivered into the electrochemical cell (with an active surface area of 6 cm<sup>2</sup>), which was heated to the set temperature. A hole in the graphite bipolar plate allows the insert of a temperature sensor and to monitor the temperature in the reaction area, which was kept at 40 ± 1 °C. The electrolytes stored in the exterior tanks were pumped through the electrochemical cell using a peristaltic pump (ShenChen, China) at a flow rate of 55 mL min<sup>-1</sup>. For the room temperature measurements, the home-made flow cell with an active surface area of 4 cm<sup>2</sup> was assembled. The FAA-3-30 anion exchange membrane was utilized in all the tests.

Table 4-6 Properties of studied electrolytes for flow cell tests

	Catholyte				Anolyte		
	types of cell	concentration of redox-active materials	supporting electrolyte	volume	concentration of redox-active materials	supporting electrolyte	volume
Two-electron reaction	(i)	0.2 M 4-OH-TEMPO	3 m BMImCl/H <sub>2</sub> O	6 mL	0.1 M MV	3 m BMImCl/H <sub>2</sub> O	6 mL
Single-electron reaction	(ii)	0.6 M 4-OH-TEMPO	3 m BMImCl/H <sub>2</sub> O	6 mL	0.6 M MV	3 m BMImCl/H <sub>2</sub> O	6 mL
	(iii)	3 M 4-OH-TEMPO	3 m EMImCl/H <sub>2</sub> O	5 mL	1 M MV	3 m EMImCl/H <sub>2</sub> O	15 mL

The electrochemical performance of a flow cell that can utilize the two-electron transfer reactions of MV was studied at first. An all-organic flow cell comprising of 0.1 M MV as anolyte (with an effective electron concentration of 0.2 M) and 0.2 M 4-OH-TEMPO as catholyte, 3 m BMImCl/H<sub>2</sub>O as supporting electrolytes and a FAA-3-30 (FumaTech) anion exchange membrane was tested at 40 °C.

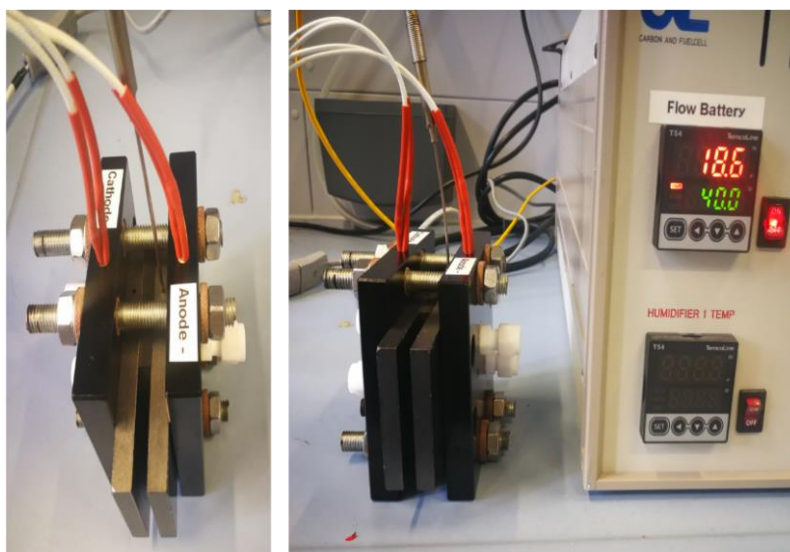


Figure 4.29 High-temperature controlled stack cell setup. Two heating rods were separately inserted into the graphite bipolar plate. A thermal sensor was inserted to detect the in-situ temperature during charge/discharge process. The left one is the top view of the reaction cell.

As shown in Figure 4.30a, from 20 to 55 mA cm<sup>-2</sup> two pairs of well-defined charge/discharge plateaus can be seen, corresponding to the oxoammonium/nitroxyl radical catholyte reaction coupled with MV<sup>2+</sup>/MV<sup>+</sup> and MV<sup>+</sup>/MV<sup>0</sup> anolyte reactions. Accordingly, the color of electrolyte reversibly changed from colorless at initial state to blue upon one-electron reduction with the formation of MV<sup>+</sup>, and then turned into colorless again after the second reduction (Figure 4.31), indicating a highly reversible process of the two-electron reactions of MV.

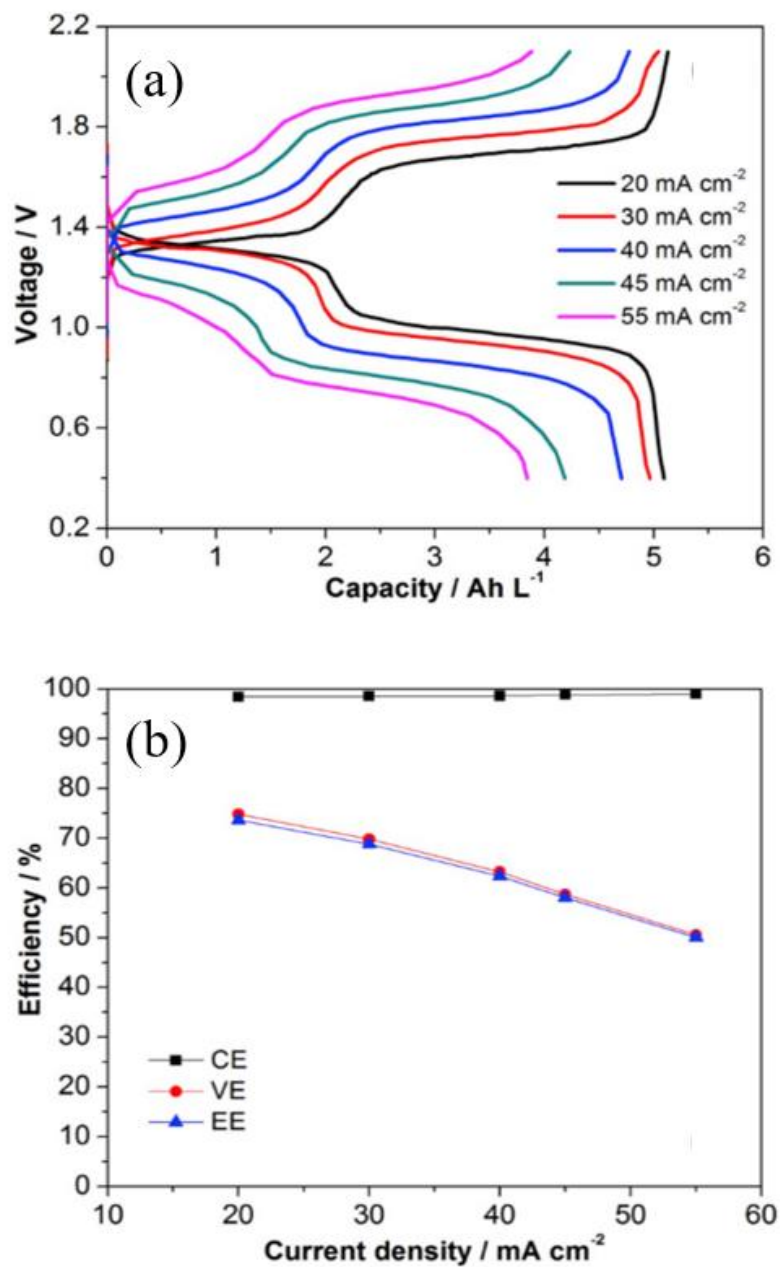


Figure 4.30 Electrochemical performance of a MV/4-OH-TEMPO flow cell (0.1 M MV in 3 m BMImCl/H<sub>2</sub>O) (a) charge and discharge curves and (b) the corresponding cycling efficiencies at different current densities.

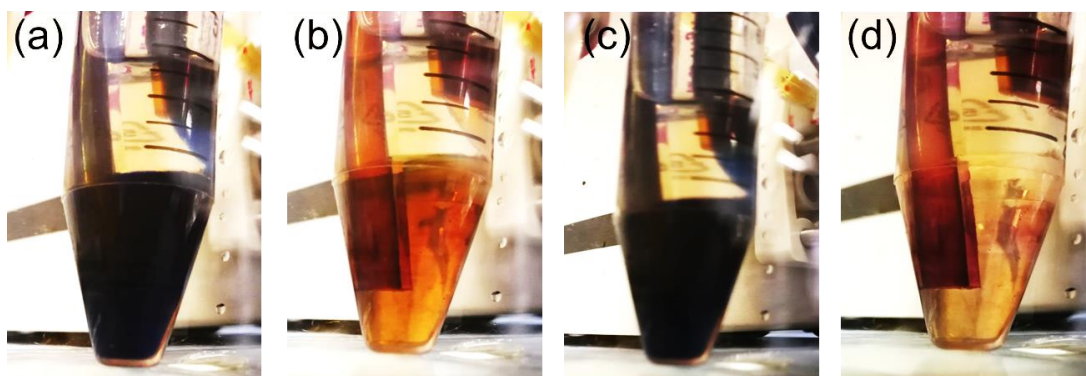


Figure 4.31 Color changes for 1 mM of MV solution during charge/discharge when coupled with 0.2 mM 4-OH-TEMPO in 3 m BMImCl/H<sub>2</sub>O. (a)  $MV^{2+} \rightarrow MV^{+}$ ; (b)  $MV^{+} \rightarrow MV^0$ ; (c)  $MV^0 \rightarrow MV^{+}$ , and (d)  $MV^{+} \rightarrow MV^{2+}$ .

At 20 mA cm<sup>-2</sup> the flow cell showed discharge plateaus with average voltages of 1.3 and 1.0 V, a CE of 99.0%, and a volumetric discharge capacity of 5.1 Ah L<sup>-1</sup>, (i.e., an energy density of 8 Wh L<sup>-1</sup>). With increasing current density, the CE remained at about 99.0%, and the voltage efficiency (VE) decreased from 75% at 20 mA cm<sup>-2</sup> to 50 % at 55 mA cm<sup>-2</sup> (Figure 4.30b). Figure 4.32 shows a stable cycling performance of the flow cell over 50 cycles at 55 mA cm<sup>-2</sup> with a discharge capacity of 3.8 Ah L<sup>-1</sup> (corresponding to an electrolyte utilization of 71%) and a steady CE of 99.0%. A capacity decay rate of 15.8% per day was observed. The charge and discharge plateau maintained well during cycling, indicating sufficient chemical stability and excellent reversibility (inset in Figure 4.32). It is considered that the chemical instability of the nitroxyl radical can be accelerated at elevated temperatures.<sup>139</sup> In addition, for the low-concentration MV analyte, its cycling stability is sensitive to the deoxygenation process.

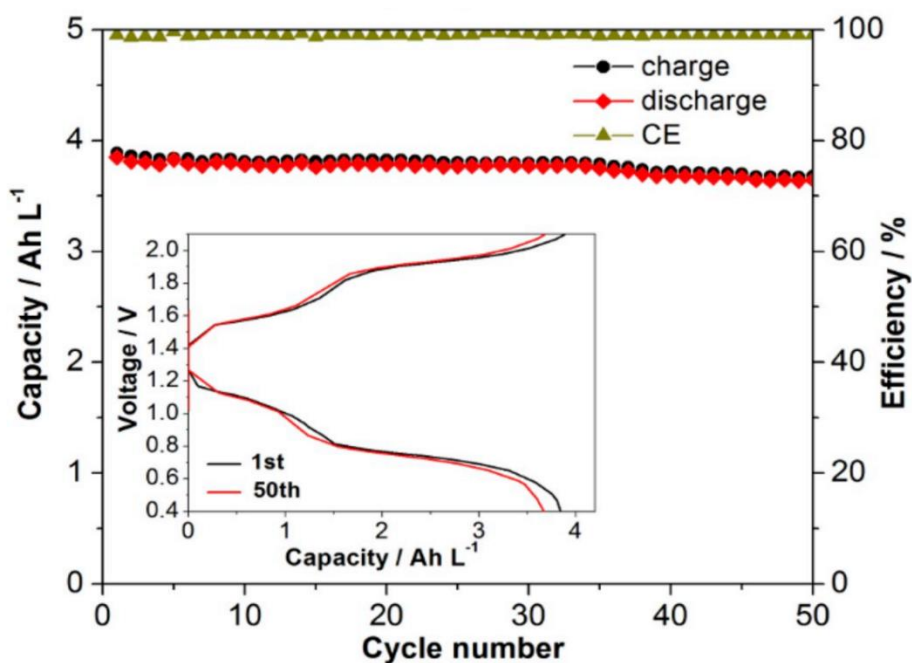


Figure 4.32 Cycling stability and CE of MV/4-OH-TEMPO flow cell (0.1 M MV in 3 m BMImCl/H<sub>2</sub>O) at 55 mA cm<sup>-2</sup> over 50 cycles. The inset shows the representative charge/discharge curve.

To trace the formation of the viologen radical species in the anolyte over cycling, ex-situ EPR spectra were recorded for the anolyte at different states of charge/discharge. At stages of “A” and “E” (namely MV<sup>2+</sup> species), as labeled in Figure 4.33a, the EPR spectra are featureless (Figure 4.33b), indicating the absence of radical species in the anolyte. After the first electron transition (stage “B”), a characteristic signal assigned to MV<sup>•+</sup> radical was observed, confirming the involvement of the MV<sup>2+</sup> → MV<sup>•+</sup> reaction. Near the end of the second charge plateau (stage “C”), an EPR signal with multiple peaks was observed, which implies the intermolecular interactions among the viologen units.<sup>140-142</sup> When discharging, the intensity of the multiple signal decreased (stage “D”, with MV<sup>•+</sup> species dominant) and finally vanished at stage “E” (MV<sup>2+</sup>). Those results confirmed the excellent two-electron reversibility of MV in the applied supporting electrolyte.

More importantly, it has been reported that the neutral state of MV<sup>0</sup> is irreversible in neutral NaCl solution.<sup>131, 143</sup> Thus, the MV is not suitable for charge-discharge

experiments with the utilization of the second electron reduction. In order to check if crystallite species and precipitates from viologen were present at stages “B” and especially “C” (with  $MV^0$  species dominant), the corresponding analytes were subjected to small-angle X-ray scattering (SAXS) measurements with a heating program from 20 to 80 °C in steps of 5 °C. The operating solutions were collected at

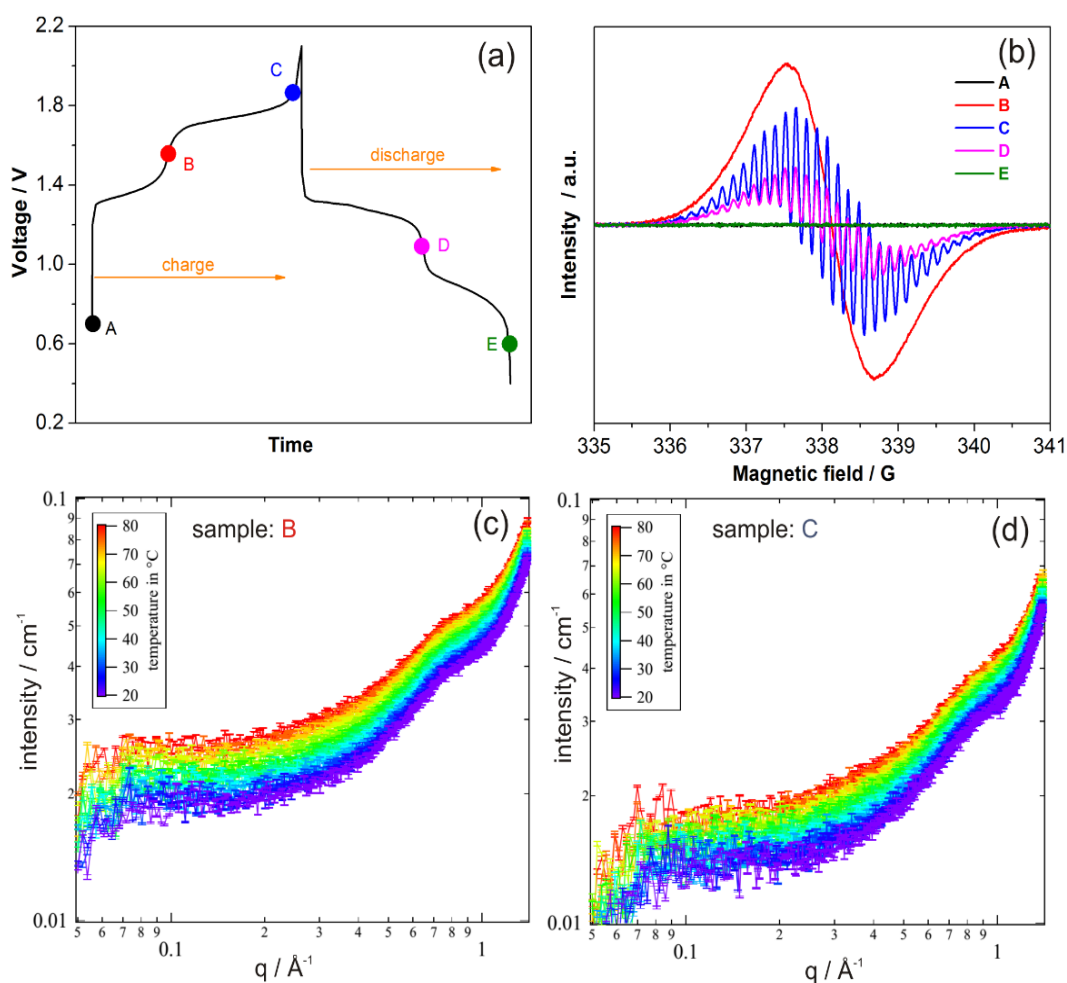


Figure 4.33 Reversible two-electron reaction of 0.1 M MV. (a) Samples collected from the analyte at different states of charge/discharge, (b) the corresponding EPR spectra. SAXS profiles with the (c) first and (d) second electron transfer reactions overheating from 20 to 80 °C.

different stages of charge in an argon-filled glove box. As shown in Figure 4.33c and d, there were no scattering peaks for both aliquots, suggesting an attractive dissolution

capability of our supporting electrolyte for the neutral  $MV^0$  species. Additionally, the scatterings of both products maintained well, and no significant crystallization peak was observed over a continuous heating measurement from R.T. to 80 °C. In contrast to phase transformations of vanadium species ( $VO_2^+$  to  $V_2O_5$ ) at temperature above 40 °C,<sup>12,20</sup> the studied samples exhibit good thermal stability of the active material and supporting electrolyte.

#### 4.3.6 Long-term stability in high concentration

To enhance the volumetric energy storage capability, electrolytes with a high concentration of active compounds are required in practice. We thus investigated the cyclability, rate performance, and cycling stability of a flow cell with 0.6 M 4-OH-TEMPO against 0.6 M MV. We found that if a high upper cutoff voltage ( $> 1.4$  V) was applied, the two-electron reactions of MV at 0.6 M formed precipitates, resulting in clogging in flow channel. Thus, the galvanostatic charge/discharge of the flow cell was performed at current densities from 20 to 75 mA cm<sup>-2</sup> and cut-off voltages between 0.6 and 1.4 V (Figure 4.34a). With a one-electron reaction of MV, the flow cell delivered capacities of 15.6, 14.2, 12.6, 11.4 and 9.2 Ah L<sup>-1</sup> at current density of 20, 30, 50, 60 and 75 mA cm<sup>-2</sup>, respectively, with a high and constant CE of 99.5% (Figure 4.34b). At 20 mA cm<sup>-2</sup>, a high electrolyte utilization of 96.8 % was observed, indicating nearly complete redox reaction of the active materials.

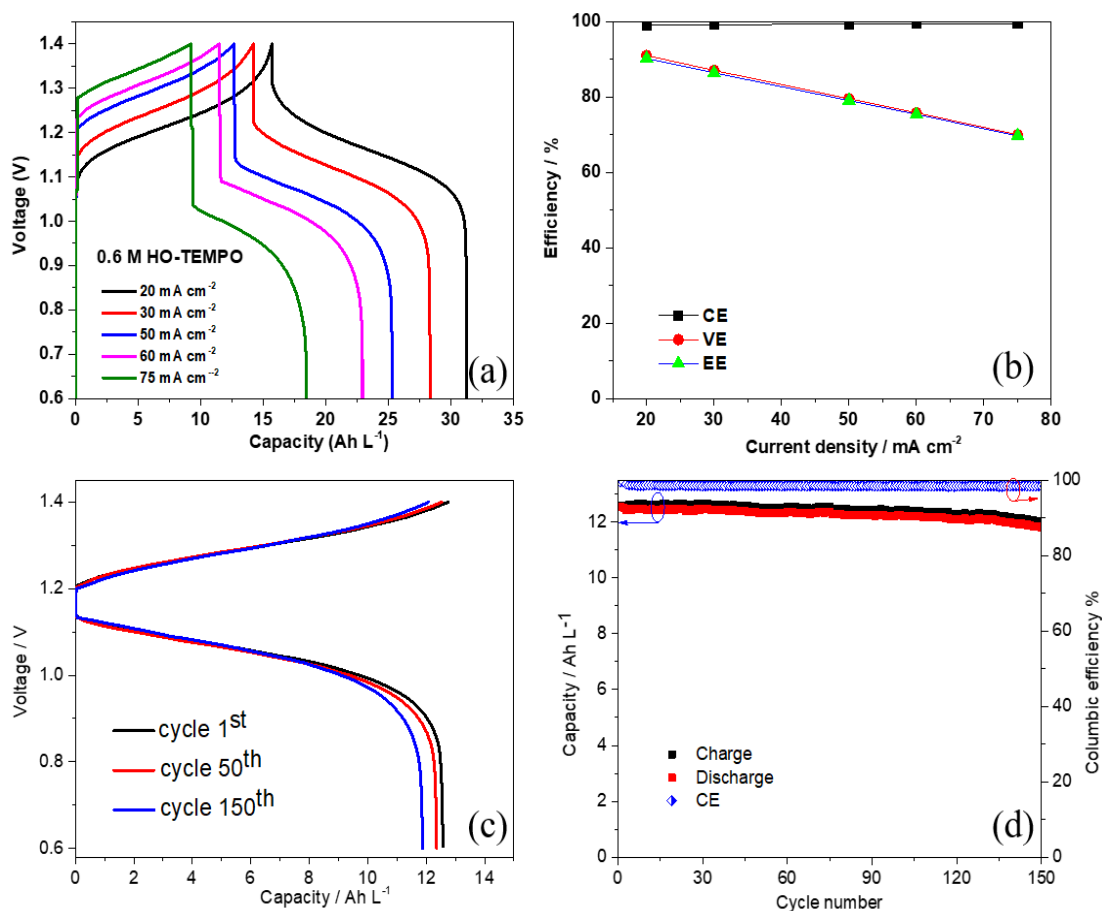


Figure 4.34 Electrochemical performance of a flow cell with 0.6 M 4-OH-TEMPO/ 0.6 M MV. (a) Voltage profiles, and (b) the corresponding efficiencies at different current densities, Cycling stability and efficiencies of the flow cell, (c) representative charge/discharge curves, and (d) cycling stability at 50 mA cm<sup>-2</sup> over 150 cycles in 3 m BMImCl/H<sub>2</sub>O.

In addition, an average discharge voltage of 1.15 V was observed, compared to 1 V for the low concentration electrolyte in Figure 4.30a at the same current density. Even at 75 mA cm<sup>-2</sup>, a high VE of 70.0% and EE of 69.7% can be still maintained, which are superior to those of previous work using TEMPO-derivatives in aqueous media ( $\leq 0.5$  M).<sup>31, 42, 134, 144-145</sup> At 50 mA cm<sup>-2</sup>, good capacity retention of 94.2% over 150 cycles was observed with nearly unchanged voltage profiles (Figure 4.34c). Afterward, anolyte and catholyte were collected for CV measurements to check if cross-mixing occurred (Figure 4.35).

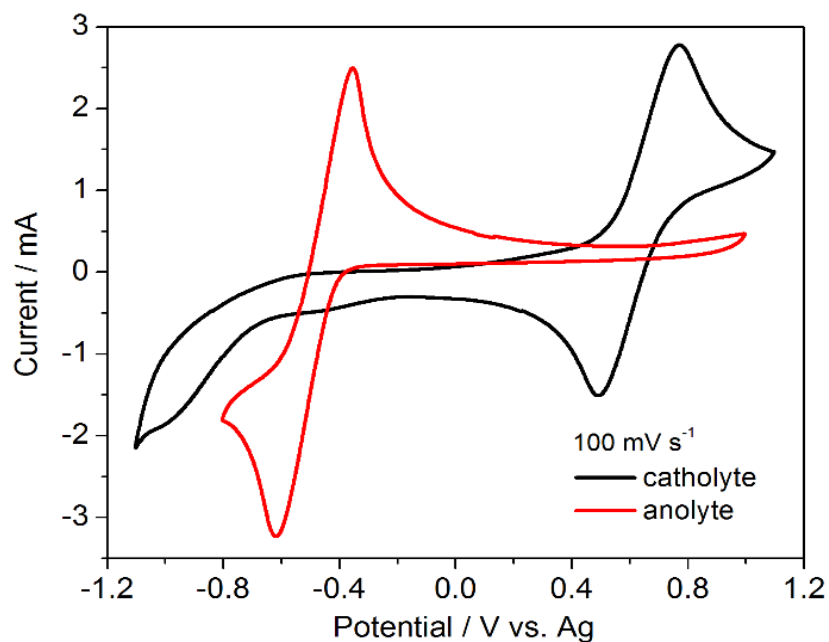


Figure 4.35 CV analysis of the 0.6 M MV and 4-OH-TEMPO electrolytes after 150 charge/discharge cycles in 3 m BMImCl/H<sub>2</sub>O supporting electrolyte at scan rate of 100 mV s<sup>-1</sup>.

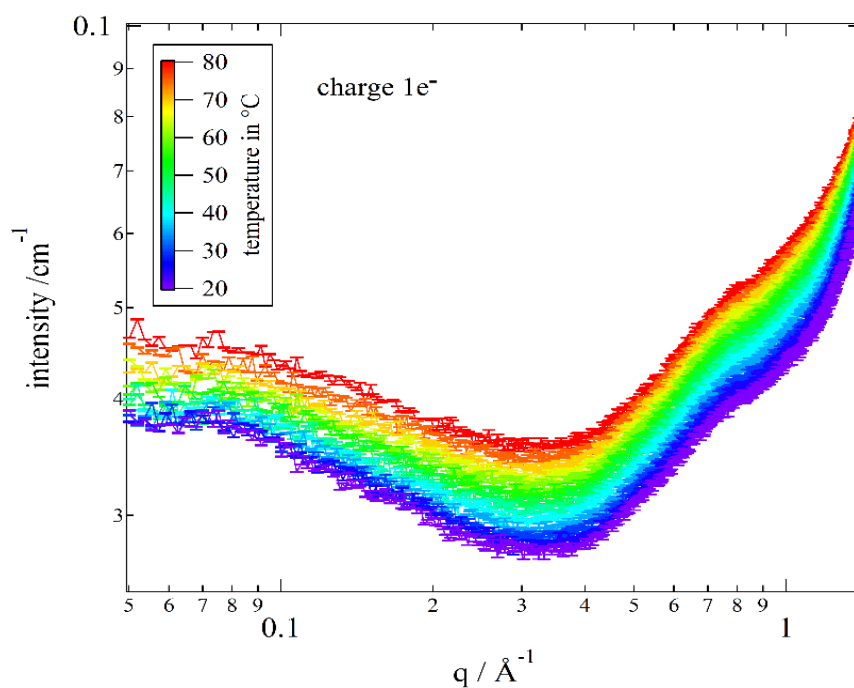


Figure 4.36 SAXS profiles of 0.6 M MV in 3 m BMImCl/H<sub>2</sub>O supporting electrolyte after the first electron transfer reaction of MV<sup>2+</sup>/MV<sup>+</sup>.

No detectable redox peaks from 4-OH-TEMPO can be seen from the anolyte, neither peaks from MV can be seen from the catholyte, confirming the low-cost anion exchange membrane is effective to avoid the cross-mixing. In addition, there were no distinct scattering peaks observed in the SAXS scattering over the wide temperature measurement (Figure 4.36), indicating that the anolyte of MV kept as a liquid feature with one-electron reaction, as expected.

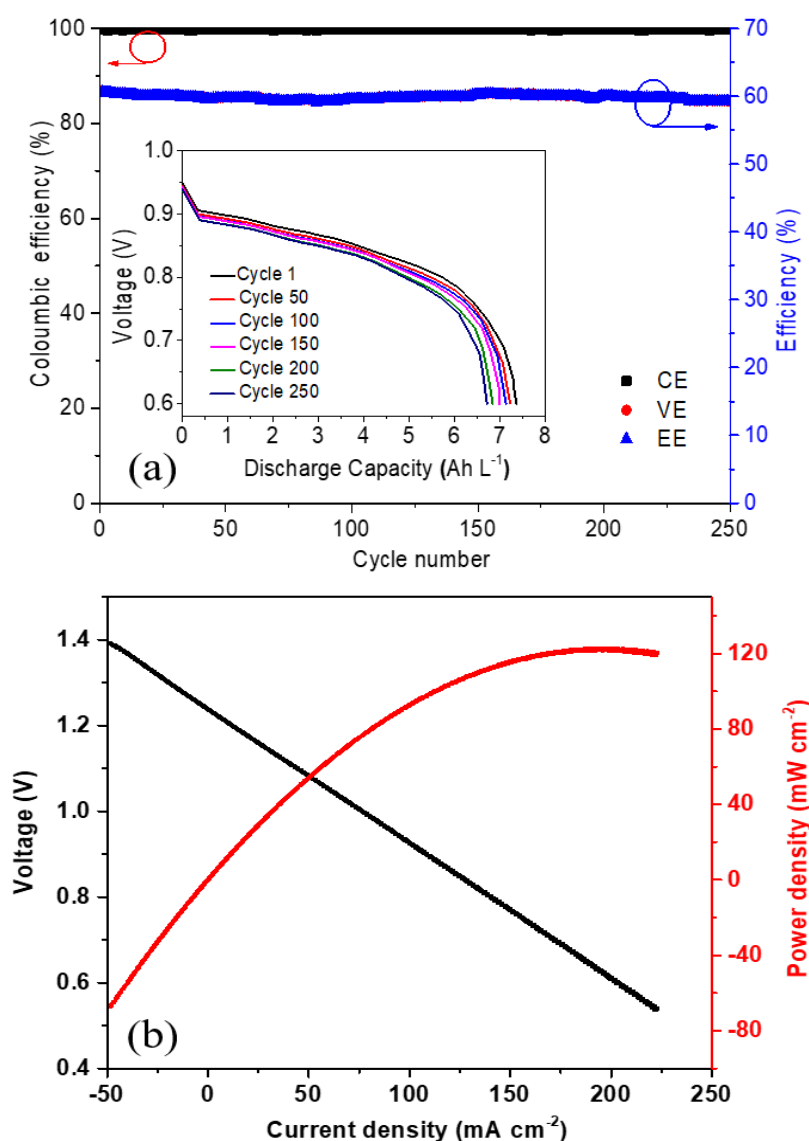


Figure 4.37 Electrochemical performance of a flow cell with 0.6 M 4-OH-TEMPO/ 0.6 M MV. (a) at 80 mA cm<sup>-2</sup> over 250 cycles in 3 m EMImCl/H<sub>2</sub>O, Inset in (A) shows the discharge curves at different cycles, (b) Polarization and power density curves of the flow cell at 100% SOC in 3 m EMImCl/H<sub>2</sub>O.

Considering that the EMImCl/H<sub>2</sub>O has a slightly lower viscosity and higher ionic conductivity compared to the BMImCl counterpart, the long-term cycling stability and rate performance of 4-OH-TEMPO/MV was also examined in the 3 m EMImCl/H<sub>2</sub>O supporting electrolyte at 80 mA cm<sup>-2</sup>.

The CE and EE remained around 99.7% and 60%, respectively, over 250 cycles with an excellent capacity retention of 91.2% (i.e., a decay of 0.035% per cycle, or 3.1% per day, Figure 4.37a). Surprisingly, such capacity retention is much better than that for 4-OH-TEMPO tested in aqueous NaCl (0.3% decay per cycle, or 12% per day,<sup>125</sup> and other aqueous Na<sub>2</sub>SO<sub>4</sub> and NaClO<sub>4</sub> (about 0.9% per cycle) against a metal anode.<sup>146</sup> It is considered that the aqueous imidazolium chloride as reaction media may inhibit the unfavorable parasitic side reactions of 4-OH-TEMPO and thus preserve the active material. In addition, previous combinations of organic materials-based electrolytes and low-cost anion exchange membranes can hardly be operated at a high current density (general < 40 mA cm<sup>-2</sup>).<sup>52</sup> Figure 4.37b shows the polarization curve of the flow cell at 100% state-of-charge, exhibiting a peak power density of 121.6 mW cm<sup>-2</sup> at 175 mA cm<sup>-2</sup>, which is comparable to the one of a previously reported viologen-based RFBs,<sup>143</sup> and among the best in neutral pH aqueous electrolytes.

Up to now, few organic materials have been demonstrated with a concentration higher than 2 M for RFBs.<sup>40, 147</sup> By using 3 m EMImCl/H<sub>2</sub>O as supporting electrolytes, 3 M 4-OH-TEMPO catholyte (5 mL) was paired with 1 M MV anolyte (15 mL). Accordingly, the capacities of catholyte and anolyte were balanced through the use of asymmetric electrolyte volume. The flow cell was able to deliver a capacity of 44 Ah L<sup>-1</sup> at 25 mA cm<sup>-2</sup> (Figure 4.38a). After the 10 cycles, the flow cell showed a lower capacity of 35 Ah L<sup>-1</sup> at 30 mA cm<sup>-2</sup>. A capacity retention of about 60 % was received over 60 cycles. The time needed to complete one charge/discharge curve was 1.5 – 2.5 h (Figure 4.38b). A relatively fast capacity fading (0.75% capacity loss per cycle, or 8.2% per day) and low electrolyte utilization were observed for the concentrated 3 M

catholyte at  $30 \text{ mA cm}^{-2}$ . The obvious capacity decay is a crucial troublesome issue with high concentrated TEMPOs due to the more serious crossover of molecules during long-term operation. The CE increased from 90% at  $25 \text{ mA cm}^{-2}$  to 94% at  $30 \text{ mA cm}^{-2}$  (Figure 4.38c). It indicates that the cross-mixing becomes severer at such a high concentration. At  $30 \text{ mA cm}^{-2}$ , steady VE and EE of 65% were observed for the flow cell using 3 M catholyte, compared to 86% in 0.6 M catholyte, due to an increased.

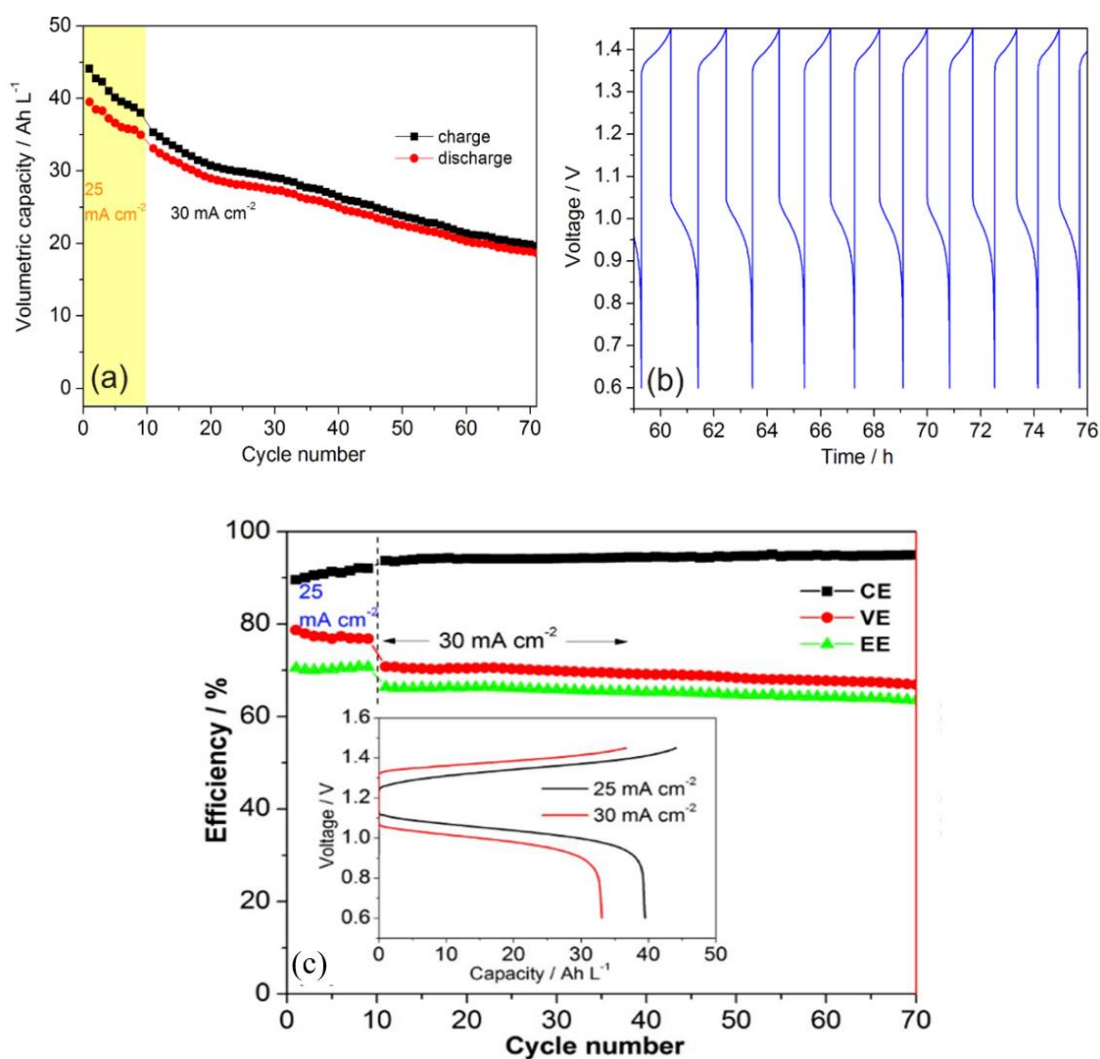


Figure 4.38 (a) Cycling stability of a flow cell with 3 M 4-OH-TEMPO catholyte at  $25 \text{ mA cm}^{-2}$  for the first 10 cycles, and  $30 \text{ mA cm}^{-2}$  for the following cycles, (b) Charge and discharge voltage profiles between the 21<sup>st</sup> and 29<sup>th</sup> cycles. (c) Cycling efficiencies of a flow cell using 3 M catholyte over 70 cycles between 0.6 and 1.45 V.

solution resistance with concentrated electrolytes. The cell resistance increased from  $1.92 \Omega \text{ cm}^2$  for 0.6 M catholyte to  $5.12 \Omega \text{ cm}^2$  for 3 M catholyte, as determined from the electrochemical impedance spectroscopy (Figure 4.39). Thus, simultaneous optimization of the chemical structure of the active materials<sup>30-31, 34, 38, 40, 42, 50, 134, 136-137, 147-149</sup> and the selection of supporting electrolytes are needed to improve the performance for concentrated electrolytes in the future.

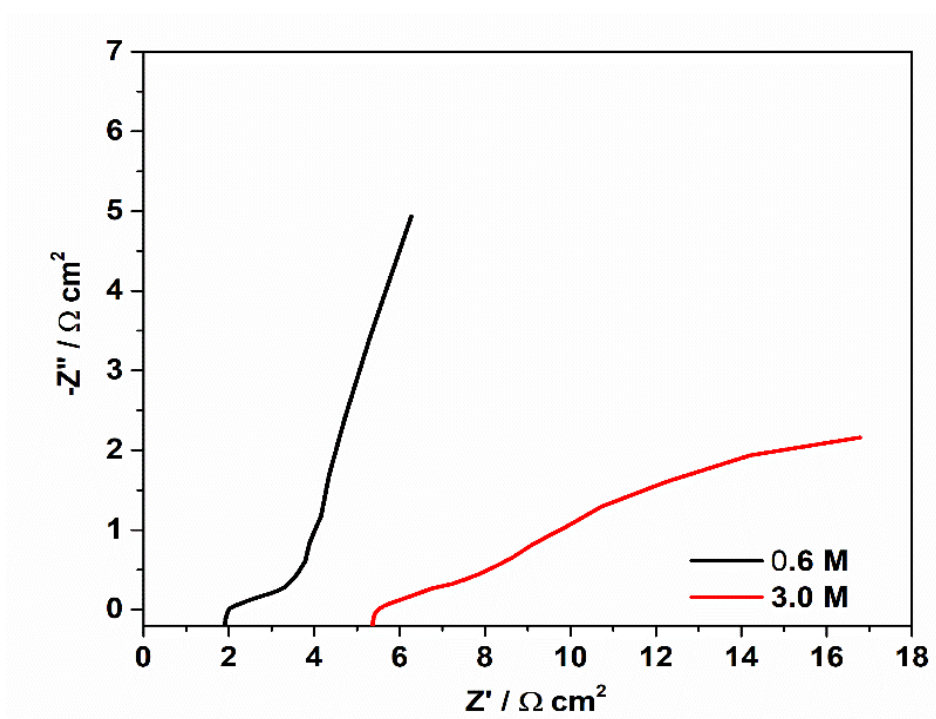


Figure 4.39 EIS of a flow cell with 0.6 M and 3.0 M catholyte, respectively.

The polarization curves obtained showed a maximum power density of  $65 \text{ mW cm}^{-2}$  (Figure 4.40a) after the first charging at  $25 \text{ mA cm}^{-2}$ . It is relatively lower than the results at 0.6 M 4-HO-TEMPO owing to the higher viscosity and lower ionic conductivity of the high concentration mixture. Figure 4.40b compares the critical performance parameters for organic materials-based aqueous RFBs in terms of concentration, cell voltage, and power density. Compared to the general chemical modification of organic materials to obtain the TEMPO-, and MV-derivatives,<sup>131, 143-144,</sup>

150-151 this work shows an alternative and promising strategy to optimize the performance of organic materials simply by choosing suitable supporting electrolytes.

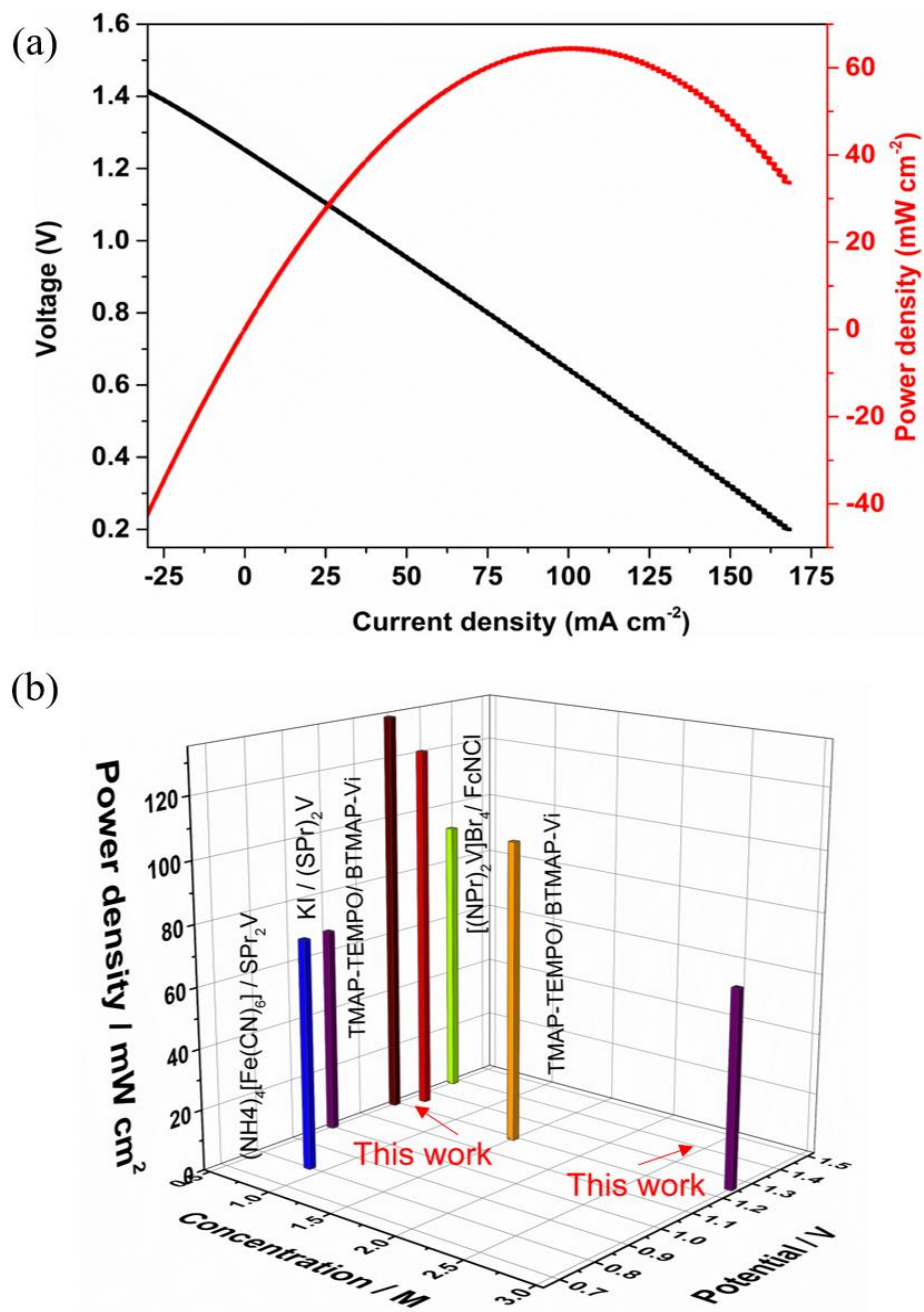


Figure 4.40 (a) Polarization and power density curves of the flow cell in 3 m EMImCl/H<sub>2</sub>O. (b) Comparison of the reported power density, concentration, and working potential: [(NPr)<sub>2</sub>V]Br<sub>4</sub>/FcNCl,<sup>151</sup> KI/(SP)<sub>2</sub>V, (NH<sub>4</sub>)<sub>4</sub>[Fe(CN)<sub>6</sub>]/(SP)<sub>2</sub>V,<sup>150</sup> and TMAP-TEMPO/BTMAP-Vi.<sup>151</sup>

---

## 4.4 Aqueous ionic liquid electrolytes for quinone-based RFB

This chapter is predominantly based on the following work:

**Z. Huang**, J. Lee, S. Kim, D. Henkensmeier, R. Hempelmann, R. Chen, Reasonable electrolytes design for electrochemical stable and concentrated quinones for redox flow batteries. *Journal of Electrochemical Society*, to be submitted.

### 4.4.1 Motivations

The quinone-based organic molecules, a class of cost-effective materials with low environmental hazards, have been intensively studied over the past years in RFBs due to their rapid reaction kinetics.<sup>152-154</sup> Nevertheless, most of the unsubstituted quinone derivatives exhibit relatively low solubility in aqueous electrolyte, making them less attractive towards high volumetric energy density.<sup>155-156</sup> Moreover, the unmodified carbon atoms in the aromatic ring are highly reactive in water and are prone to Michael reaction with water, resulting in fast capacity loss and short cycling life.<sup>157-159</sup> Different from the structural engineering of organic molecules, electrolyte optimization also indicates that it has an essential influence on the physicochemical and electrochemical properties of redox-active species. So far, an adequate capacity of functional quinone derivatives has been achieved according to the pH adjustments.<sup>160</sup> The use of appropriate supporting electrolytes may enhance the solubility of organic redox solutes dependent on “like dissolves like”<sup>42</sup> or reliable molecular interactions mechanism.<sup>161</sup>

In this chapter, a series of 2,6-dimethoxyhydroquinone (DMH<sub>2</sub>Q) and para-benzoquinone (BQ), and 2-methoxyhydroquinone (MH<sub>2</sub>Q) were studied in imidazolium chloride-based aqueous supporting electrolytes. At a different concentration of imidazolium chloride, it was found that the quinone derivatives

exhibited distinct differences in solubility, redox potential, and electrochemical reversibility. A high concentration of 7.9 M was reached for MH<sub>2</sub>Q in 10 molality aqueous electrolytes. In addition, the Michael-addition reactions influenced by water were effectively hindered due to the possible exclusion of free water in the water-in-EMIm<sup>+</sup> solution. The feasibility of flow battery pairing with vanadium anolyte and anion exchange membrane exhibited a Coulombic efficiency of 98.5% and capacity retention of 80% over 140 cycles. By properly designing the supporting electrolytes, this work is beneficial for achieving a stable, high concentration redox electrolyte.

#### 4.4.2 Solubility of quinones in aqueous ionic liquid electrolytes

In general, the concentration of active species is a predominant parameter that determines the overall energy density of RFB. Figure 4.41 shows that increasing the imidazolium content of supporting electrolytes from 3 m to 10 m leads to better solubility of each compound in general.

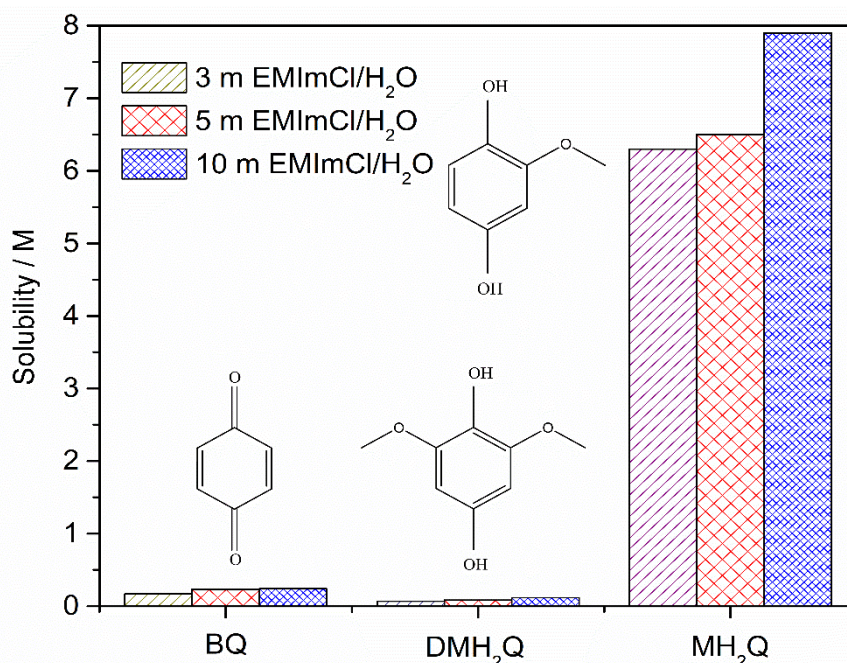


Figure 4.41 The measured solubilities of quinones derivatives: BQ, DMH<sub>2</sub>Q, and MH<sub>2</sub>Q in different concentrations of EMImCl/H<sub>2</sub>O supporting electrolytes.

This increased tendency of solubility can be explained by the suggestive intermolecular interactions between the cations and redox organic solutes.<sup>138, 161</sup> The BQ and DMH<sub>2</sub>Q showed very low solubility of about 0.24 and 0.12 M, respectively, even in 10 m EMImCl/H<sub>2</sub>O solution. In contrast, high solubility (>7.0 M) of MH<sub>2</sub>Q was obtained in the same electrolyte components. Since the molecular structure of MH<sub>2</sub>Q is less symmetric than DMH<sub>2</sub>Q, we conclude that the solubility is highly dependent on the charge distribution, as observed in previous works.<sup>138, 152, 154, 157</sup> Noticeably, the solubility of MH<sub>2</sub>Q in EMIMCl/H<sub>2</sub>O solution is 7.9 M, which is potentially around 15 times more than other derivatives in aqueous solution.<sup>38, 156</sup> It is supposed that an energy density of 423 Ah L<sup>-1</sup> could be achieved with consideration of a two-electron transition, showing the highest ever reported capacity in all kinds of redox flow batteries. As a result, the high solubility of redox-active materials shows great potential for energy-rich RFBs.

#### 4.4.3 Electrochemical properties of quinones

In order to gain a better understanding of the redox behaviors, the cyclic voltammogram (CV) measurements were applied in different concentrations of supporting electrolyte, as shown in Figure 4.42. In general, the peak current increases with the change of the imidazolium cation content from 10 m to 3 m EMImCl/H<sub>2</sub>O due to the relatively higher ionic conductivity and lower viscosity of the low content solution.<sup>161</sup> In the CV curves, BQ underwent successive one-electron reaction steps, generating two separate redox-waves (Figure 4.42a). It was observed that the first step is more reversible than the second step. Meanwhile, DMH<sub>2</sub>Q exhibited a wide peak-to-peak separation in the cyclic voltammogram (Figure 4.42b). In contrast, the second redox-peaks was negligibly observed in MH<sub>2</sub>Q (Figure 4.42c). As clearly seen from Figure 4.42d, interestingly, the position of first peaks of BQ matches the second redox peaks of MH<sub>2</sub>Q, implying the same intermediates may be involved in the redox cycle.

The voltammetric variation of DMH<sub>2</sub>Q and MH<sub>2</sub>Q might attribute to differences in the molecular structure.

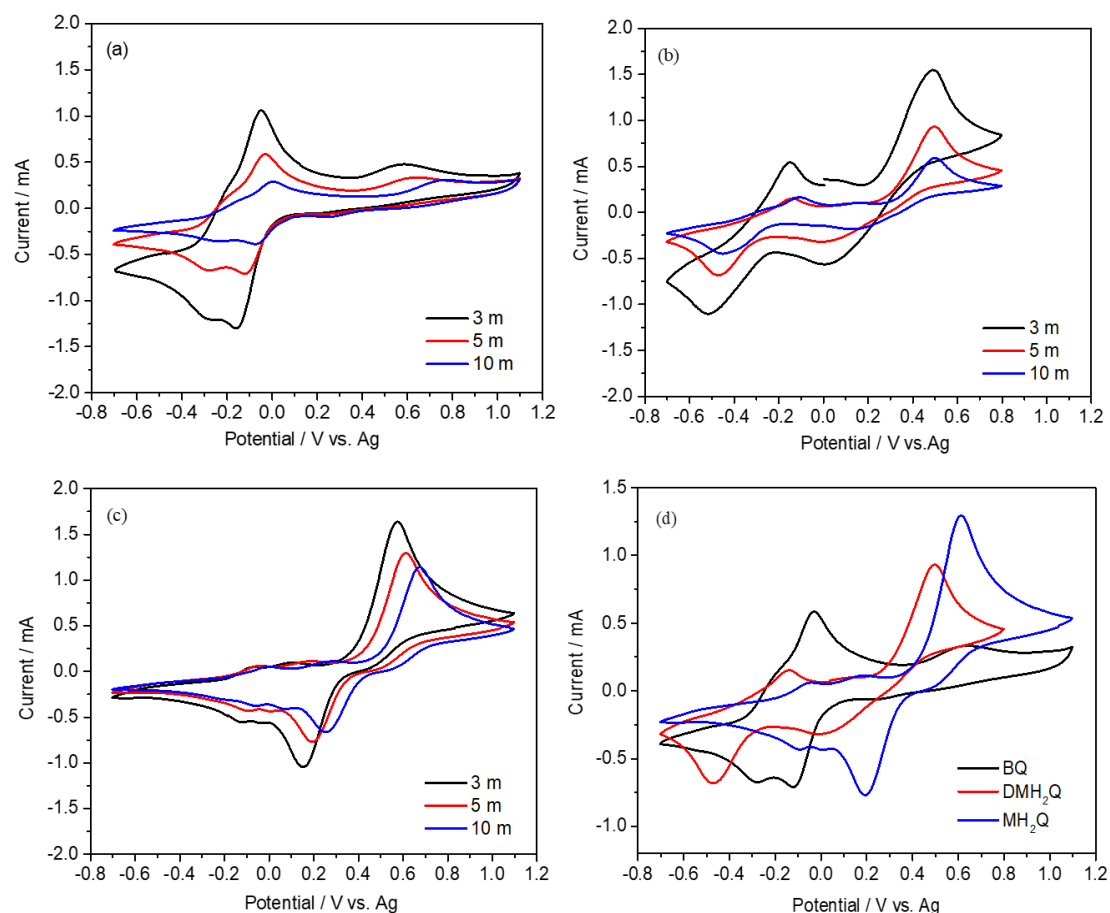
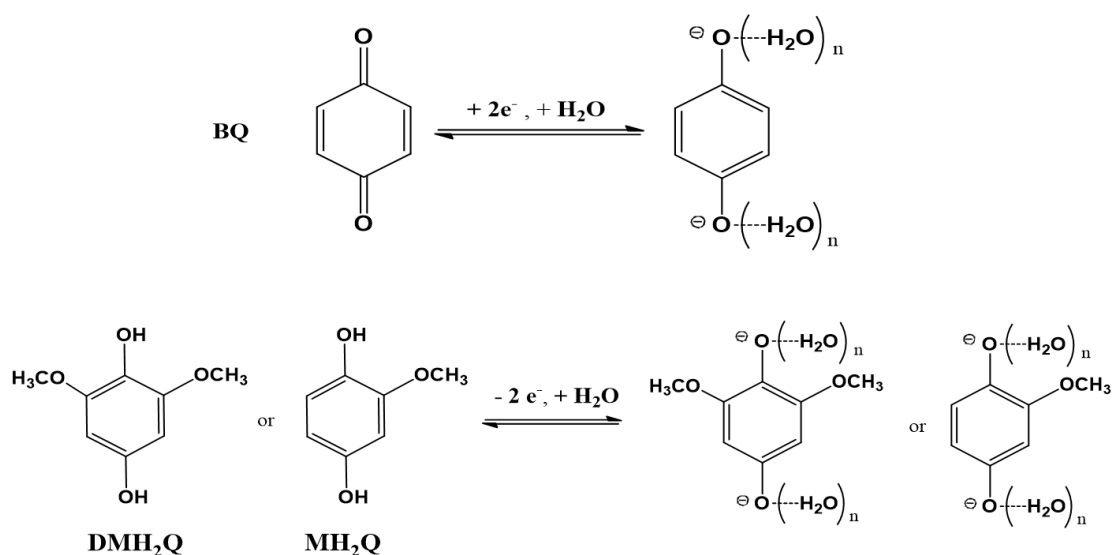


Figure 4.42 CV curves of 0.05 M quinone derivative of (a) BQ (b) DMH<sub>2</sub>Q, and (c) MH<sub>2</sub>Q in varied molalities of EMImCl/H<sub>2</sub>O solution at 50 mV s<sup>-1</sup>, and (d) Comparison of the CV results recorded in 5 m EMImCl/H<sub>2</sub>O solution.

As reported in previous works, the redox behavior of quinone derivatives is highly pH-dependent.<sup>162-163</sup> In the unbuffered pH 7.2 water solution, it has been demonstrated that BQ undergoes an overall two-electron reduction reaction.<sup>163, 166-167</sup> In the basic solution, the products existing as a mixture of Q<sup>2-</sup> and protonated anion (QH<sup>-</sup>) were stabilized by the hydrogen bonding. The pH of the used electrolytes here is in the range of 7.1-7.4. Hence, the reaction mechanism of the used quinones was proposed in

Scheme 4–1. The DMH<sub>2</sub>Q and MH<sub>2</sub>Q experienced a reverse deprotonated process. The separate redox-peak in the investigated solution was supposed to be the ion-pair effect between EMIm<sup>+</sup> cation and semiquinone radicals, which is consistent with the results observed in TBA<sup>+</sup> and semiquinone.<sup>164-165</sup> Additionally, the well-shaped CV results indicate that the Michael reaction was hindered, which might be because the concentrated EMIm<sup>+</sup> solvating shell can shield the quinones sterically against nucleophilic attack by water molecules. In order to further investigate the effect of supporting electrolytes, MH<sub>2</sub>Q was selected as candidate materials owing to its advantages in electrochemical reversibility and solubility.



Scheme 4–1 Redox reaction mechanism of quinones related to the CV results in EMImCl/H<sub>2</sub>O.

Since the electron transfer process for quinones is inherently slow, HCl solution was added to facilitate the reaction kinetics. Figure 4.43a showed that hydroquinone exhibited a single redox peak in different ionic liquid concentrations.

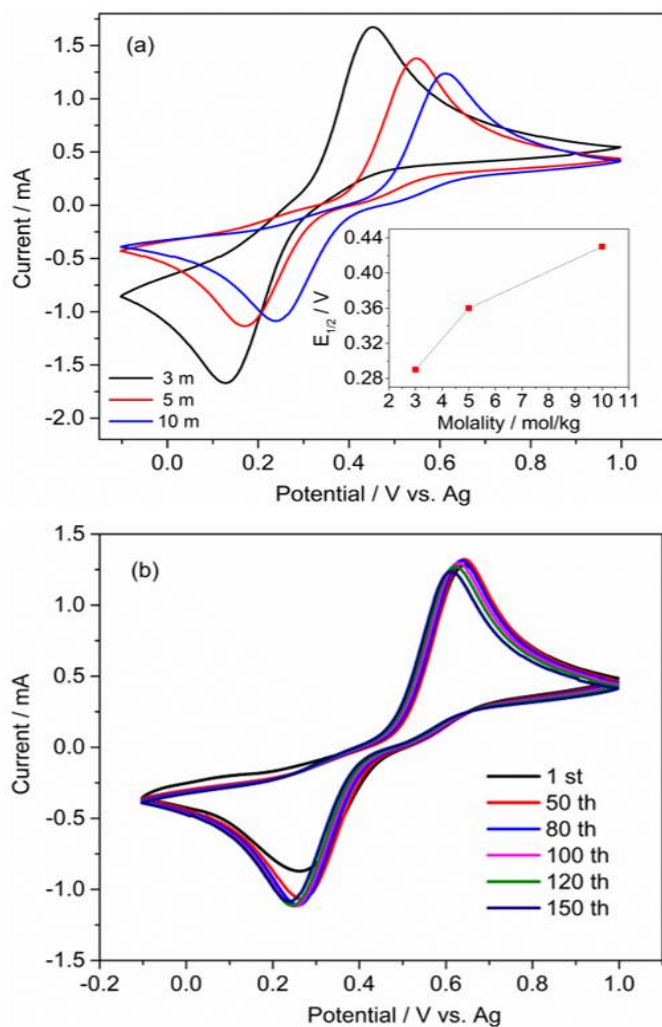
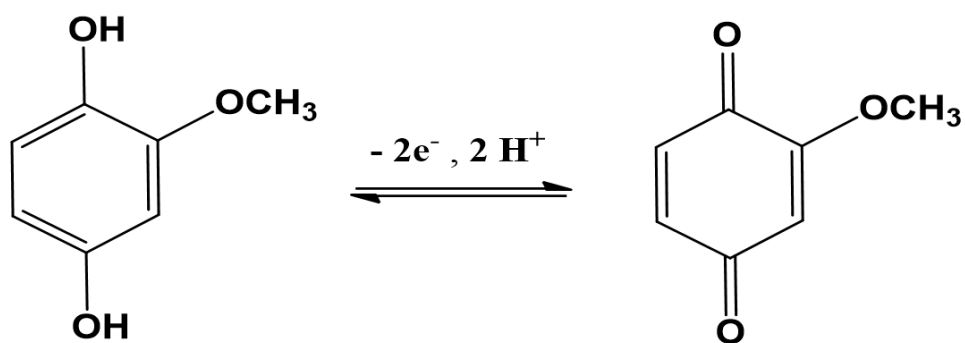


Figure 4.43 CV curves of 0.05 M MH<sub>2</sub>Q in the presence of 0.02 M HCl solution at 50 mV s<sup>-1</sup>. (a) Organic species swept in varying EMImCl/H<sub>2</sub>O concentrations. (b) Repeated scanning of redox species over 150 times in 10 m EMImCl/H<sub>2</sub>O solution.



Scheme 4-2 Reaction mechanism of MH<sub>2</sub>Q in acidic solution.

The MH<sub>2</sub>Q undergoes a two-electron two-proton reaction process from MH<sub>2</sub>Q to methoxyl benzoquinone (MBQ) in the presence of proton donors.<sup>166</sup> In the presence of HCl, the redox half potential ( $E_{1/2}$ ) had a negligible shift in comparison to the initial results in Figure 4.42c, which is consistent with the Nernst equation. The half redox potential of MH<sub>2</sub>Q increased from 0.28 V to 0.43 V vs. Ag with increasing concentration of ionic liquids (inset in Figure 4.43a). Figure 4.43b displayed a nearly overlapped redox peaks over 150 cycles, indicating high chemical and electrochemical stability. As illustrated in Scheme 4–2, two-electron, two-proton oxidation and reduction of MH<sub>2</sub>Q were interpreted as a simple two-electron transfer, giving a single redox peak.<sup>162-163</sup>

Next, the redox behavior of HCl containing electrolytes was scanned from 5 to 200 mV s<sup>-1</sup> (Figure 4.44a). The peak currents show a linear increase with the square roots of the scan rates (Figure 4.44b), revealing a diffusion-controlled process of the reaction. Therefore, the ionic diffusion coefficient ( $D_i$ ) of  $1.78 \times 10^{-6}$  cm<sup>2</sup> s<sup>-1</sup> was calculated by the *Randles-Sevcik equation* (Equation 4.2),<sup>103, 167</sup>

$$i_p = 2.69 \times 10^5 n^{\frac{3}{2}} A C D_i^{\frac{1}{2}} v^{\frac{1}{2}} \quad 4.2$$

where  $i_p$  denotes the peak current (A),  $n$  is the transferred number of electrons (2),  $A$  is the specific contacting area (0.165 cm<sup>2</sup>),  $C$  is the bulk concentration of electroactive species ( $5 \times 10^{-5}$  mol cm<sup>-3</sup>), and  $v$  is the scan rate (V s<sup>-1</sup>).

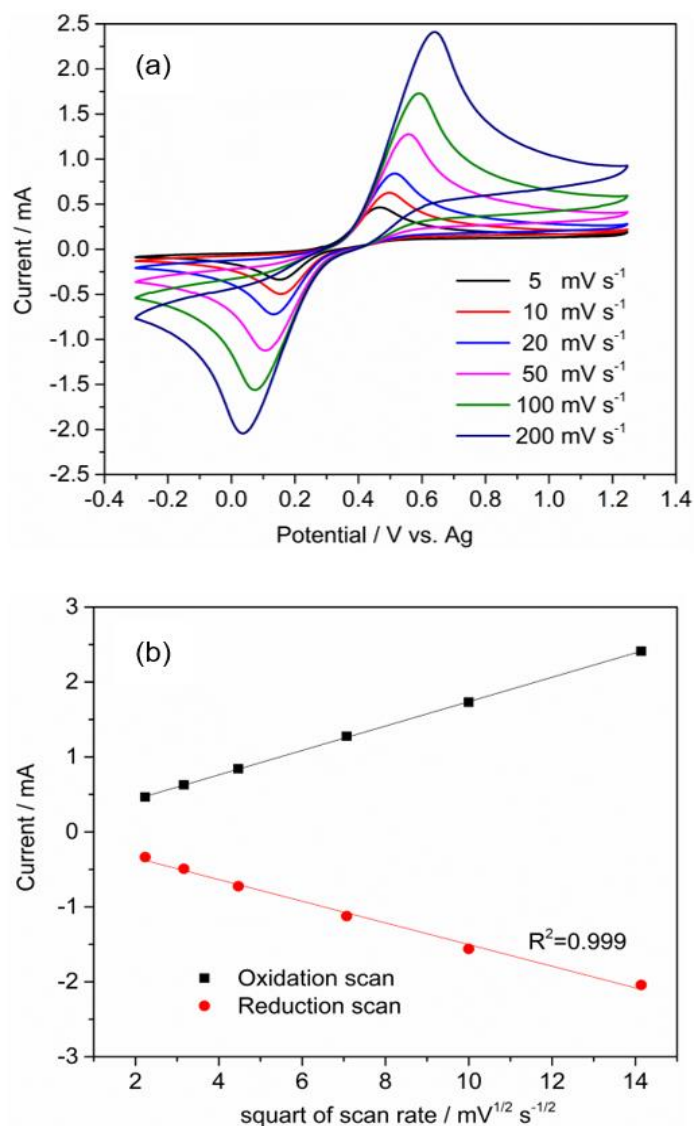


Figure 4.44 CV curves of 0.05 M MH<sub>2</sub>Q in the presence of 0.02 M HCl solution. (a) measurements at different scanning rates, and (b) the corresponding Randle-Sevcik plots in 10 m EMImCl/H<sub>2</sub>O solution.

The reaction kinetics of MH<sub>2</sub>Q were investigated by the linear sweep voltammetry (LSV) method with the RDE setup. The potentials of the rotating-electrode were swept in the range of 0.4 to 1.1 V for 1 mM 4-OH-TEMPO catholyte, and -1.2 to 0 V for 1 mM MV analyte, respectively. All of the anodic limiting diffusion current ( $i_L$ ) was gradually stabilized by the potential polarization from the equilibrium state to low overpotentials at various rotation rates from 200 to 1800 rpm (Figure 4.45a). The linear

fitting of limiting currents against the square roots of rotation rates ( $\omega^{1/2}$ ) was measured at the potential range of 0.3-1.2 V vs. Ag, as shown in Figure 4.45b. The yielded diffusion coefficient of MH<sub>2</sub>Q was calculated as  $1.87 \times 10^{-6} \text{ cm}^2 \text{ s}^{-1}$ , according to the Levich equation,<sup>103</sup> which is close to the CV results. This diffusion coefficient is comparable to that of most quinone derivatives in alkaline solution.<sup>156, 168</sup>

As seen from the LSV curve, the current is influenced both from the kinetics of the reaction (charge transfer) and the mass transport before the limiting current is established. Hence, the current of the reaction can be expressed by the *Koutecký-Levich equation* (Equation 4.3),

$$\frac{1}{i} = \frac{1}{i_k} + \frac{1}{i_l} \quad 4.3$$

where  $i_k$  and  $i_l$  are the kinetically limited and mass transport limited currents, respectively. The kinetic current  $i_k$  can be extrapolated to infinite rotation rates as shown in Figure 4.45c.

Meanwhile, the heterogeneous electron transfer rate constant ( $k_0$ ) and transfer coefficient ( $\alpha$ ) are analyzed based on the kinetically controlled region. The current was transformed into a logarithmic form to the overpotential as plotted in Figure 4.45d. Accordingly, the fitting line was expressed by the *Tafel equation* (Equation 4.4),

$$\log_{10}(i) = \log_{10}(i_0) - \frac{anF\eta}{2.303RT} \quad 4.4$$

where  $i_0$  is the exchange current. The exchange current was determined from the vertical-intercept, and the kinetic rate constant ( $k_0$ ) was calculated using Equation 4.5,

$$i_0 = nFAC_0k_0 \quad 4.5$$

where the concentration of reactants and products are meant to be the same. The electron-transfer rate constant ( $k_0$ ) was calculated to be  $9.13 \times 10^{-6} \text{ cm s}^{-1}$ , which is still higher than the vanadium redox couples of VO<sup>2+</sup>/VO<sub>2</sub><sup>+</sup> ( $2 \times 10^{-6} \text{ cm s}^{-1}$ ) in sulfuric acid solution.<sup>169</sup> This indicates that MH<sub>2</sub>Q in aqueous imidazolium chloride solution meets

the basic criteria as the positive electrode material for aqueous organic redox flow battery.

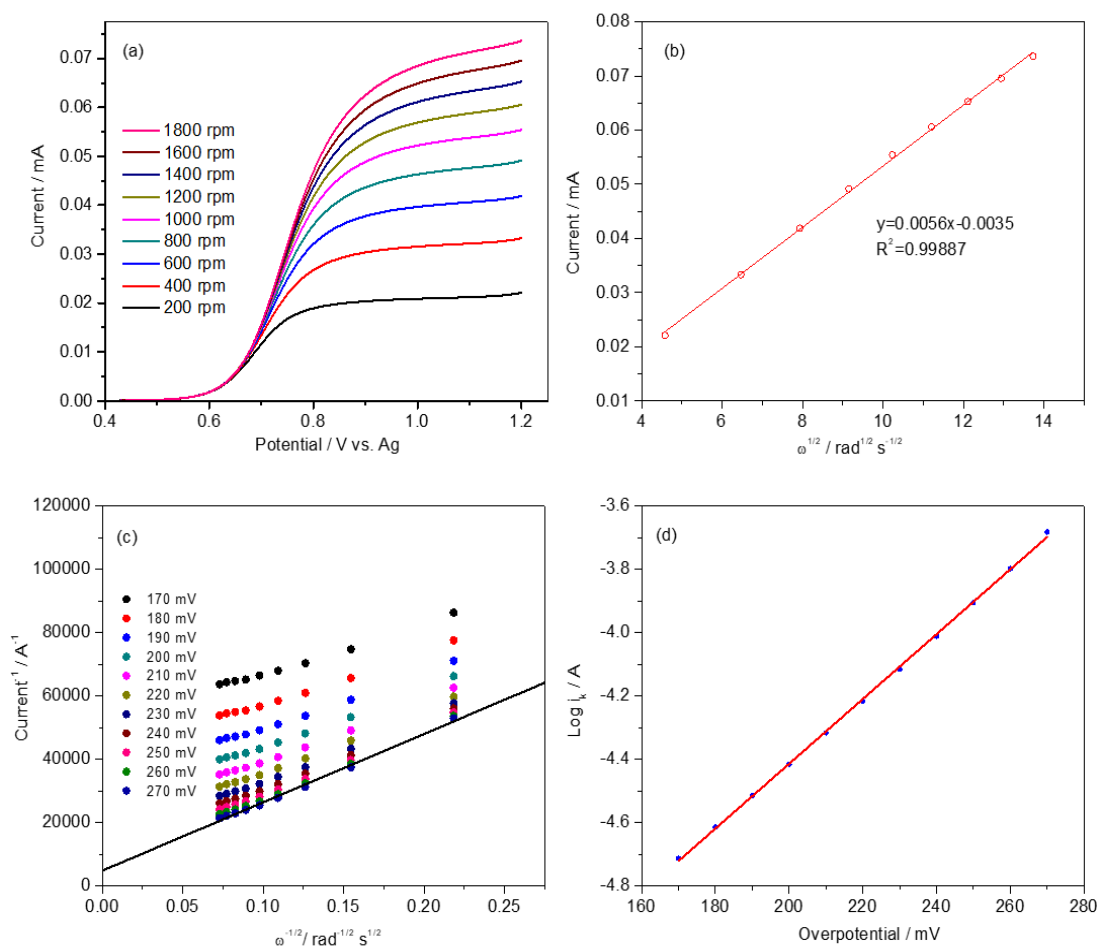


Figure 4.45 (a) RDE studies of the oxidation of 1 mM  $\text{MH}_2\text{Q}$  in 0.02 M  $\text{HCl}$  + 10 m  $\text{EMImCl}/\text{H}_2\text{O}$  on a glassy carbon electrode with a scan rate of  $5 \text{ mV s}^{-1}$  at rotation rates between 200-1800 rpm. (b) Levich plot of the limited transport current versus the square roots of rotation rates. (c) Koutecký-Levich plot derived from different overpotentials. (d) The fitting plot of the Butler-Volmer equation derived from different overpotentials.

#### 4.4.4 Long-term performance of quinone-based redox electrolytes

The catholyte uses 0.08 M  $\text{MH}_2\text{Q}$  in 1.0 M  $\text{HCl}$  of 10 m  $\text{EMImCl}/\text{H}_2\text{O}$  solutions. Vanadium electrolyte with 0.16 M  $\text{V}^{3+}$  was used as anolyte, which was obtained through electrochemical reduction of the commercial vanadium electrolyte of  $\text{V}^{3.5+}$  (1.6 M,

$\text{VO}^{2+}/\text{V}^{3+}$ , 1:1, GfE Metalle and Materialien GmbH, Germany) in a flow cell and then diluted to a suitable concentration. Saturated NaCl was added into the anolyte side to balance the osmotic pressure between the two electrolytes. Both electrolytes were circulated at a speed of  $50 \text{ mL min}^{-1}$  under a peristaltic pump (Easy pump China) at room temperature with a volume of 8.0 mL.

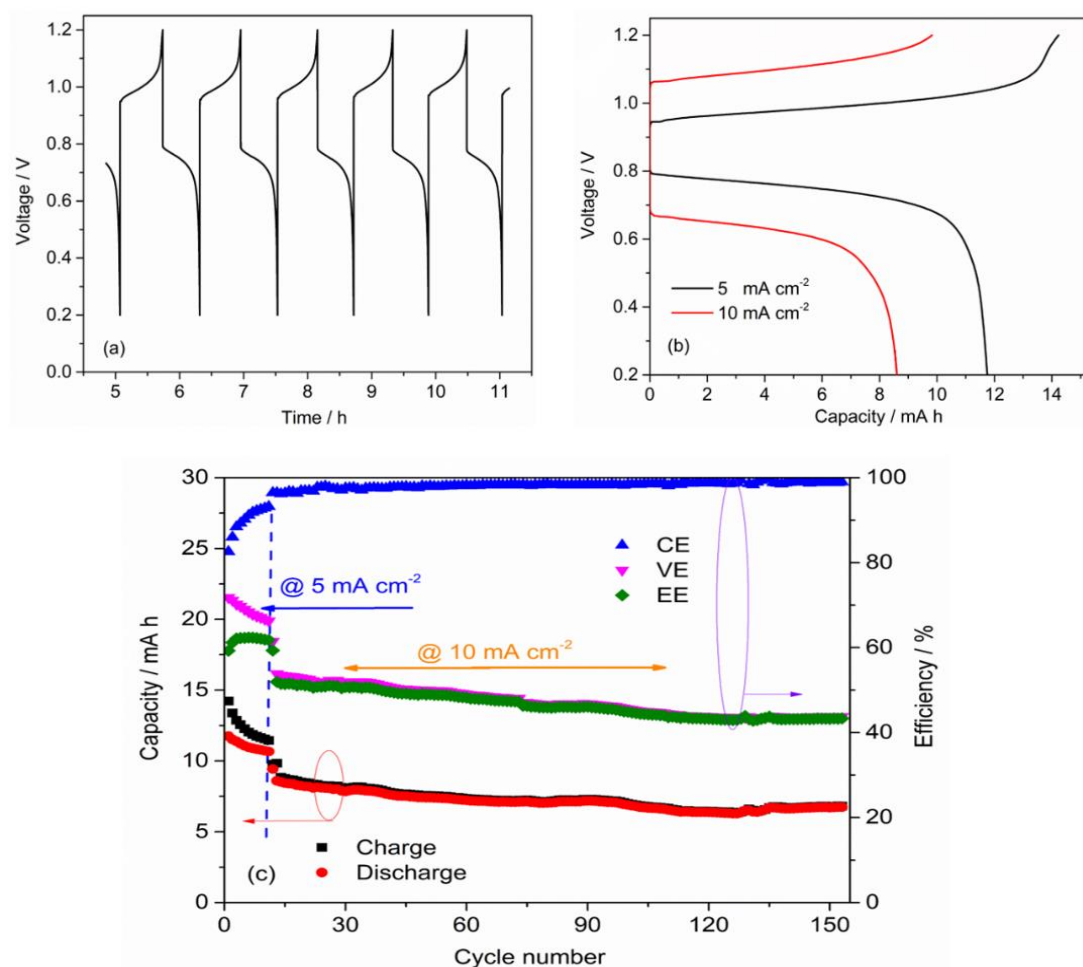


Figure 4.46 Electrochemical performance of  $\text{MH}_2\text{Q}/\text{V}^{3+}$  ARFB. (a) Voltage vs. time curves recorded between 3<sup>rd</sup> and 7<sup>th</sup> cycles at  $5 \text{ mA cm}^{-2}$ . (b) The initial charge and discharge curve at  $5 \text{ mA cm}^{-2}$  and  $10 \text{ mA cm}^{-2}$ . (c) Long-term cycling performance of the battery, the current density was increased to  $10 \text{ mA cm}^{-2}$  after 12 cycles at  $5 \text{ mA cm}^{-2}$ .

The electrochemical performance of  $\text{MH}_2\text{Q}/\text{V}^{3+}$  ARFB was tested using a cross-linked methylated polybenzimidazole (PBI) anion exchange membrane at room temperature.

The apparent charge and discharge plateau at 1.05 V and 0.75 V, respectively, were observed in Figure 4.46a. A stable charge/discharge behavior was maintained despite capacity is slightly diminished. The initial charge and discharge capacities (Figure 4.44b, black line) are 14.3 and 12.5 mA h at 5 mA cm<sup>-2</sup>, respectively. After 12 cycles, the current density was increased to 10 mA cm<sup>-2</sup>, which showed a decrease in the capacity of 10 mA h (Figure 4.46b, red line). After the initial cycles at 5 mA cm<sup>-2</sup>, the CE of the cell was gradually increased and maintained a steady value of about 98.5 % over 140 cycles at a current density of 10 mA cm<sup>-2</sup>. Note that when operating at higher current density, the ohmic polarization was increased, resulting in a lower voltage efficiency (Figure 4.46c). The capacity retention measured was about 80% over 140 cycles, and the capacity degradation rate was 1.3% per cycle.

It notes that the MH<sub>2</sub>Q is a small molecule that can permeate into the membranes, which makes the ion exchange membranes less selective. The severe capacity loss could possibly be attributed to parasitic reactions and residual oxygen in the aqueous electrolyte. Therefore, it is necessary to take measures to maintain the cycling stability of the redox-active materials. In addition, the flow cell experiments in high concentrations of electroactive species should be conducted via advanced cell design and new membrane developments.

---

## 5. Conclusion and outlook

In conclusion, this thesis highlights the possibility of using “water-in-ionic liquid” electrolytes for redox-active organic RFBs. Owing to the strong molecular interactions between the imidazolium cations and water, the aqueous-ILs showed excellent thermal stability over wide temperature ranges. In addition, the high solubility of electroactive organic materials was achieved. It was demonstrated that the aqueous-ILs electrolytes played a significant role in the electrochemical performance of suitable organic/organometallic molecules. Hence, this work provides a sustainable research direction for the development of all-weather and high energy density RFBs.

As illustrated in Chapter 4.2, our proposed aqueous-ILs electrolyte can circumvent water crystallization at subzero temperatures and hydrogen evolution under rather low negative potentials. Thermal analysis over -80 to 80 °C shows such an electrolyte to be free of transition events (e.g. icing and phase changes) under atmospheric pressure. The occurrence of phase separation of the electroactive materials is suppressed in the BMImCl/H<sub>2</sub>O solution as revealed by the structure sensitive in-situ SAXS spectrum. Significantly, the unprecedented temperature stability of the electrolytes was successfully demonstrated in RFBs between -32–65 °C. The inexpensive metal phthalocyanine anolyte displayed multi-electron transfer reactions at low negative potentials (-0.2 to -1.6 V vs. Ag) that are not accessible in common aqueous electrolytes.

Chapter 4.3 explored the potential of compatible supporting electrolytes, that can enable the solubility, electrochemical reversibility, and chemical stability well. 3 m aqueous imidazolium (BMIm<sup>+</sup> and EMIm<sup>+</sup>) chlorides supporting electrolytes

demonstrated high ionic conductivity (a maximum of  $83 \text{ mS cm}^{-1}$ ) and water-like flowability (with a minimum viscosity of  $1.8 \text{ mPa s}$ ). A record aqueous solubility of  $4.3 \text{ M}$  for the commercial 4-OH-TEMPO has been achieved, arising from enhanced intermolecular interactions as studied from EPR measurements. In addition, our supporting electrolytes permit the two-electron reactions of unmodified MV with excellent reversibility and stability, and specific solubility of neutral  $\text{MV}^0$  species as examined from SAXS experiments. This result is distinct from earlier work that  $\text{MV}^0$  forms precipitation in aqueous NaCl and shows electrochemical irreversibility. At  $0.6 \text{ M}$  of MV, only one-electron transfer reaction is possible in the liquid state. For the  $0.6 \text{ M}$  full organic flow cell, excellent cycling stability and rate performance have been observed, which is superior to those from previous work using aqueous sodium salts as supporting electrolytes. It is deduced that our proposed supporting electrolytes as new reaction media for the redox-active organic materials can preserve well their molecular structure by suppressing the side reactions. For the first time, 4-OH-TEMPO catholyte with a high concentration of  $3 \text{ M}$  was evaluated in a flow cell, which showed a high energy efficiency of  $65\%$  at  $30 \text{ mA cm}^{-2}$ .

Chapter 4.4 studied how the imidazolium-based ionic liquids affect the solubility and electrochemical properties of quinone derivatives.  $\text{MH}_2\text{Q}$  showed a high concentration of  $7.9 \text{ M}$ , with a theoretical capacity of  $423 \text{ Ah L}^{-1}$ . Because of the molecular interaction between the  $\text{EMIm}^+$  cations and  $\text{MH}_2\text{O}$ , the nucleophilic attack by water was effectively suppressed and resulted in excellent electrochemical reversibility. The reaction kinetic of  $\text{MH}_2\text{Q}$  showed comparable results in contrast to the conventional vanadium ions in sulfuric acid. Nevertheless, a noteworthy capacity loss over extended battery cycling experiments should be improved with deeper mechanism interpretation and advanced cell design.

Further studies could be performed to improve the electrochemical performance of RFBs.

- By exploring the compatible electroactive electrolytes, the critical parameters, such as electrochemical stability window, solubility, electrochemical reversibility, and chemical stability, can be further optimized.
- Desirable redox-active organic materials yielding higher cell voltage, and multi-electron transfer reactions are expected to improve the overall energy density.
- Molecular interaction mechanisms among solvents, ionic liquids, and electroactive organic materials could be elucidated by NMR, Raman, and DFT analysis.
- The cost-effective membranes with high selectivity and ionic conductivity are vital to offer high power density and reduce the capital costs of the system.
- Further studies focusing on chemical kinetics improvement can be achieved by catalyst modification of the electrode. Meanwhile, the redox potentials and solubility of organic compounds in aq-ILs electrolytes can be guided by theoretical calculations.

---

## Materials and chemicals

---

Description	CAS No.	Molecular formula or Abbreviation	Molecular Weight / g mol <sup>-1</sup>	Grade	Supplier
1-butyl-3-methylimidazolium chloride	79917-90-1	BMIImCl	174.67	98.0%	Sigma-Aldrich
1-ethyl-3-methylimidazolium chloride	65039-09-0	EMIImCl	146.62	97.0%	Acros Organics
Nickel(II) phthalocyanine-tetrasulfonic acid tetrasodium salt	27835-99-0	NiTsPc	979.4	98.0%	Sigma-Aldrich
Copper(II) phthalocyanine-tetrasulfonic acid tetrasodium salt	123439-80-5	CuTsPc	896.3	98.0%	Sigma-Aldrich
Ferrous chloride tetrahydrate	13478-10-9	FeCl <sub>2</sub> ·4 H <sub>2</sub> O	198.81	99.0%	Fluka
Nickel(II) phthalocyanine	237-893-3	NiPc	571.2	85%	Sigma-Aldrich

---

Materials and chemicals

Sodium chloride	7647-14-5	NaCl	58.44	99.0%	Sigma-Aldrich
Potassium hydroxide	1310-58-3	KOH	56.106	86.7%	VWR Chemicals
<i>p</i> -Toluenesulfonyl chloride acid	98-59-9	<i>p</i> TsOH	190.65	98.0%	Alfa Aesar
Sulphuric acid	7664-93-9	H <sub>2</sub> SO <sub>4</sub>	98.08	98.0%	Merck
Hydrochloric acid	7647-01-0	HCl	36.46	37%	VWR
4-Hydroxy-2,2,6,6-tetramethylpiperidine 1-oxyl	222-96-2	4-OH-TEMPO	172.24	97.0%	Sigma-Aldrich
Methyl viologen dichloride hydrate	75365-73-0	MV	257.16	98.0%	Sigma-Aldrich
2-methoxyhydroquinone	824-46-4	MH <sub>2</sub> Q	140.14	98.0%	Alfa Aesar
Para-benzoquinone	106-51-4	BQ	108.09	98.0%	Sigma-Aldrich
2,6-dimethoxyhydroquinone	15233-65-5	DMH <sub>2</sub> Q	170.16	97.0%	Sigma-Aldrich

# Abbreviations

Abbreviation	Description		
RFBs	Redox flow batteries	$i_{pc}$	Cathodic peak current
VRFB	Vanadium redox flow battery	$i_{pa}$	Anodic peak current
EES	Electrochemical energy storage	$i_l$	Limiting current
ILs	Ionic liquids	$k_0$	Kinetic reaction rate constant
Aq-ILs	Water-in-ionic liquids	$n$	Number of transfer electrons
DEEs	Deep eutectic electrolytes	$\eta$	Overpotential
SHE	Standard Hydrogen electrode	$R_s$	Solution resistance
WE	Working electrode	$R_{ct}$	Charge-transfer resistance
CE	Counter electrode	$D_i$	Diffusion coefficient
Ref	Reference electrode	$Z'$	Real part of resistance
OCV	Open circuit voltage	$-Z''$	Imaginary part of resistance
SOC	State of charge	$Z_w$	Warburg impedance
ESW	Electrochemical stability window	CE	Coulombic efficiency
CV	Cyclic voltammetry	VE	Voltage efficiency
LSV	Linear sweep voltammetry	EE	Energy efficiency
RDE	Rotating disk electrode	AEM	Anion exchange membrane

## Abbreviations

---

$A$	Electrode surface area	CEM	Cation exchange membrane
$E_{pc}$	Peak cathodic potential	EIS	Electrochemical impedance spectroscopy
$E_{pa}$	Peak anodic potential	DSC	Differential scanning calorimetry
$\Delta E$	Peak separation	SAXS	Small-angle X-ray scattering
$F$	Faraday constant	EPR	Electron paramagnetic resonance

---

## Publications and conferences

### Patent

R. Chen (35%), **Z. Huang** (35%), S. Kim (15%), and R. Hempelmann (15%), Electrolyte comprising eutectic mixture, in preparation, 2020.

### Book Chapter

R. Chen, **Z. Huang**, R. Hempelmann, D. Henkensmeier, S. Kim, Vanadium Redox Flow Batteries (*volume Ed. S. Passerini*), *Encyclopedia of Electrochemistry*, 2020.

### Publications

1. **Z. Huang**, J. Lee, S. Kim, D. Henkensmeier, R. Hempelmann, R. Chen, A highly concentrated quinones enabled by aqueous ionic liquids electrolytes for redox flow batteries. *J. Electrochem. Soc.*, to be submitted, 2020.
2. **Z. Huang**, C. Kay, B. Kuttich, D. Rauber, T. Kraus, H. Li, S. Kim, R. Chen, An “interaction-mediating” strategy towards enhanced solubility and redox properties of organics for aqueous flow batteries. *Nano Energy*, 69, 104464 (2020), DOI: 10.1016/j.nanoen.2020.104464.
3. **Z. Huang**, P. Zhang, X. Gao, D. Henkensmeier, S. Passerini, R. Chen, Unlocking Simultaneously the Temperature and Electrochemical Windows of Aqueous Phthalocyanine Electrolytes, *ACS Appl. Energy Mater.* 2, 3773-3779 (2019), DOI:10.1021/acsaem.9b00467.

4. Tatlisu, **Z. Huang**, R. Chen, High-Voltage and Low-Temperature Aqueous Supercapacitor Enabled by “Water-in-Imidazolium Chloride” Electrolytes, *ChemSusChem*, 11, 3899-3904 (2018), DOI: 10.1002/cssc.201802046.
5. R. Ye, D. Henkensmeier, S. Yoon, **Z. Huang**, D. Kim, Z. Chang, S. Kim, R. Chen, Redox Flow Batteries for Energy Storage: A Technology Review. *J. Electrochem. En. Conv. Stor.*, 15, 010801 (2018).

### Conferences

1. **Z. Huang**, R. Chen, R. Hempelmann, Unlocking the temperature and solubility properties of aqueous redox flow batteries, *Doktorandentag, Poster*, November 2019, Saarbrücken, Germany.
2. R. Chen, **Z. Huang**, P. Zhang, D. Henkensmeier, R. Hempelmann, Ionic liquids-promoted utilization of redox-active organic materials for flow batteries, *Meeting Abstracts*, ECS meeting. 5, 242-242, 2019.
3. **Z. Huang**, R. Hempelmann, R. Chen, Aqueous electrolyte with concurrent electrochemical and temperature stability window for redox flow battery, *118th General Assembly of the German Bunsen Society for Physical Chemistry (DBG), Poster*, 2019, Jena, Germany.
4. **Z. Huang**, R. Hempelmann, R. Chen, TEMPO impregnated suspension for redox flow battery, *117th General Assembly of the German Bunsen Society for Physical Chemistry (DBG), Poster*, 2018, Hannover, Germany.
5. **Z. Huang**, R. Hempelmann, R. Chen, Anion intercalation electrode for high-voltage redox flow battery, *116th General Assembly of the German Bunsen Society for Physical Chemistry (DBG), Poster*, 2017, Kaiserslautern, Germany

---

# Erklärung

Ich versichere hiermit, dass ich die Arbeit selbständig angefertigt habe und keine anderen als die angegebenen Quellen und Hilfsmittel benutzt sowie die wörtlich oder inhaltlich übernommenen Stellen als solche kenntlich gemacht habe.

Saarbrücken, den 31.05.2020

Zhifeng Huang

scan of signature



Vorname Nachname / Unterschrift

---

## Bibliography

1. Armand, M.; Tarascon, J.-M., Building Better Batteries. *Nature* **2008**, *451*, 652-657.
2. Yang, Z.; Zhang, J.; Kintner-Meyer, M. C.; Lu, X.; Choi, D.; Lemmon, J. P.; Liu, J., Electrochemical Energy Storage for Green Grid. *Chem. Rev.* **2011**, *111*, 3577-3613.
3. Vazquez, S.; Lukic, S. M.; Galvan, E.; Franquelo, L. G.; Carrasco, J. M., Energy Storage Systems for Transport and Grid Applications. *IEEE Trans. Ind. Electron.* **2010**, *57*, 3881-3895.
4. Dunn, B.; Kamath, H.; Tarascon, J.-M., Electrical Energy Storage for the Grid: A Battery of Choices. *Science* **2011**, *334*, 928-935.
5. Chen, H.; Cong, T. N.; Yang, W.; Tan, C.; Li, Y.; Ding, Y., Progress in Electrical Energy Storage System: A Critical Review. *Prog. Nat. Sci.* **2009**, *19*, 291-312.
6. Poizot, P.; Dolhem, F., Clean Energy New Deal for a Sustainable World: From Non-CO<sub>2</sub> Generating Energy Sources to Greener Electrochemical Storage Devices. *Energy Environ. Sci.* **2011**, *4*, 2003-2019.
7. Thackeray, M. M.; Wolverton, C.; Isaacs, E. D., Electrical Energy Storage for Transportation—Approaching the Limits of, and Going Beyond, Lithium-Ion Batteries. *Energy Environ. Sci.* **2012**, *5*, 7854-7863.
8. Nobel Prize in Chemistry. **2019**, <https://www.nobelprize.org/prizes/chemistry/2019/summary/>.
9. Tarascon, J.-M.; Armand, M., Issues and Challenges Facing Rechargeable Lithium Batteries. *Nature* **2001**, *414*, 359-367.
10. Xu, J.; Ma, J.; Fan, Q.; Guo, S.; Dou, S., Recent Progress in the Design of Advanced Cathode Materials and Battery Models for High-Performance Lithium-X (X= O<sub>2</sub>, S, Se, Te, I<sub>2</sub>, Br<sub>2</sub>) Batteries. *Adv. Mater.* **2017**, *29*, 1604054.
11. Soloveichik, G. L., Flow Batteries: Current Status and Trends. *Chem. Rev.* **2015**, *115*, 11533-11558.

12. Skyllas-Kazacos, M.; Cao, L.; Kazacos, M.; Kausar, N.; Mousa, A., Vanadium Electrolyte Studies for the Vanadium Redox Battery-a Review. *ChemSusChem* **2016**, *9*, 1521-1543.
13. Larcher, D.; Tarascon, J.-M., Towards Greener and More Sustainable Batteries for Electrical Energy Storage. *Nat. Chem.* **2015**, *7*, 19-29.
14. Winsberg, J.; Hagemann, T.; Janoschka, T.; Hager, M. D.; Schubert, U. S., Redox-Flow Batteries: From Metals to Organic Redox-Active Materials. *Angew. Chem. Int. Ed.* **2017**, *56*, 686-711.
15. Kangro, W.; Pieper, H., Zur Frage Der Speicherung Von Elektrischer Energie in Flüssigkeiten. *Electrochim. Acta* **1962**, *7*, 435-448.
16. Hagedorn, N. H. NASA Redox Storage System Development Project. Final Report, *National Aeronautics and Space Administration, Cleveland, OH (USA)*. Lewis, **1984**.
17. Wang, W.; Nie, Z.; Chen, B.; Chen, F.; Luo, Q.; Wei, X.; Xia, G. G.; Skyllas-Kazacos, M.; Li, L.; Yang, Z., A New Fe/V Redox Flow Battery Using a Sulfuric/Chloric Mixed-Acid Supporting Electrolyte. *Adv. Energy Mater.* **2012**, *2*, 487-493.
18. Lim, H.; Lackner, A.; Knechtli, R., Zinc-Bromine Secondary Battery. *J. Electrochem. Soc.* **1977**, *124*, 1154.
19. Davies, T. J.; Tummino, J. J., High-Performance Vanadium Redox Flow Batteries with Graphite Felt Electrodes. *C. J. Carbon Res.* **2018**, *4*, 8.
20. Sum, E.; Rychcik, M.; Skyllas-Kazacos, M., Investigation of the V(V)/V(IV) System for Use in the Positive Half-Cell of a Redox Battery. *J. Power Sources* **1985**, *16*, 85-95.
21. Sum, E.; Skyllas-Kazacos, M., A Study of the V(II)/V(III) Redox for Redox Flow Cell Applications. *J. Power Sources* **1985**, *15*, 179-190.
22. Rychcik, M.; Skyllas-Kazacos, M., Characteristics of a New All-Vanadium Redox Flow Battery. *J. Power Sources* **1988**, *22*, 59-67.
23. Skyllas-Kazacos, M.; Menictas, C.; Kazacos, M., Thermal Stability of Concentrated V(V) Electrolytes in the Vanadium Redox Cell. *J. Electrochem. Soc.* **1996**, *143*, L86-L88.
24. Kausar, N.; Howe, R.; Skyllas-Kazacos, M., Raman Spectroscopy Studies of Concentrated Vanadium Redox Battery Positive Electrolytes. *J. Appl. Electrochem.*

- 2001**, *31*, 1327-1332.
25. Kazacos, M.; Kazacos, M. S., High Energy Density Vanadium Electrolyte Solutions, Methods of Preparation Thereof and All-Vanadium Redox Cells and Batteries Containing High Energy Vanadium Electrolyte Solutions. *World Patents*, **2002**, *WO1996035239A1*.
  26. Wang, W.; Luo, Q.; Li, B.; Wei, X.; Li, L.; Yang, Z., Recent Progress in Redox Flow Battery Research and Development. *Adv. Funct. Mater.* **2013**, *23*, 970-986.
  27. Crawford, A.; Viswanathan, V.; Stephenson, D.; Wang, W.; Thomsen, E.; Reed, D.; Li, B.; Balducci, P.; Kintner-Meyer, M.; Sprenkle, V., Comparative Analysis for Various Redox Flow Batteries Chemistries Using a Cost Performance Model. *J. Power Sources* **2015**, *293*, 388-399.
  28. Dmello, R.; Milshtein, J. D.; Brushett, F. R.; Smith, K. C., Cost-Driven Materials Selection Criteria for Redox Flow Battery Electrolytes. *J. Power Sources* **2016**, *330*, 261-272.
  29. Chen, H.; Cong, G.; Lu, Y.-C., Recent Progress in Organic Redox Flow Batteries: Active Materials, Electrolytes and Membranes. *J. Energy. Chem.* **2018**, *27*, 1304-1325.
  30. Huskinson, B.; Marshak, M. P.; Suh, C.; Er, S.; Gerhardt, M. R.; Galvin, C. J.; Chen, X.; Aspuru-Guzik, A.; Gordon, R. G.; Aziz, M. J., A Metal-Free Organic-Inorganic Aqueous Flow Battery. *Nature* **2014**, *505*, 195-198.
  31. Liu, T.; Wei, X.; Nie, Z.; Sprenkle, V.; Wang, W., A Total Organic Aqueous Redox Flow Battery Employing a Low Cost and Sustainable Methyl Viologen Anolyte and 4-HO-TEMPO Catholyte. *Adv. Energy Mater.* **2016**, *6*, 1501449.
  32. Storage, E., Program Planning Document. *US Department of Energy: Office of Electricity Delivery and Energy Reliability*, **2011**.
  33. Hu, B.; DeBruler, C.; Rhodes, Z.; Liu, T. L., Long-Cycling Aqueous Organic Redox Flow Battery (AORFB) toward Sustainable and Safe Energy Storage. *J. Am. Chem. Soc.* **2017**, *139*, 1207-1214.
  34. Hollas, A.; Wei, X.; Murugesan, V.; Nie, Z.; Li, B.; Reed, D.; Liu, J.; Sprenkle, V.; Wang, W., A Biomimetic High-Capacity Phenazine-Based Anolyte for Aqueous Organic Redox Flow Batteries. *Nat. Energy* **2018**, *3*, 508.
  35. Lin, K.; Gómez-Bombarelli, R.; Beh, E. S.; Tong, L.; Chen, Q.; Valle, A.; Aspuru-Guzik, A.; Aziz, M. J.; Gordon, R. G., A Redox-Flow Battery with an Alloxazine-Based Organic Electrolyte. *Nat. Energy* **2016**, *1*, 16102.
  36. Janoschka, T.; Martin, N.; Martin, U.; Friebe, C.; Morgenstern, S.; Hiller, H.;

- Hager, M. D.; Schubert, U. S., An Aqueous, Polymer-Based Redox-Flow Battery Using Non-Corrosive, Safe, and Low-Cost Materials. *Nature* **2015**, *527*, 78-81.
37. Ding, Y.; Zhang, C.; Zhang, L.; Zhou, Y.; Yu, G., Molecular Engineering of Organic Electroactive Materials for Redox Flow Batteries. *Chem. Soc. Rev.* **2018**, *47*, 69-103.
38. Lin, K.; Chen, Q.; Gerhardt, M. R.; Tong, L.; Kim, S. B.; Eisenach, L.; Valle, A. W.; Hardee, D.; Gordon, R. G.; Aziz, M. J., Alkaline Quinone Flow Battery. *Science* **2015**, *349*, 1529-1532.
39. Wei, X.; Xu, W.; Vijayakumar, M.; Cosimbescu, L.; Liu, T.; Sprenkle, V.; Wang, W., TEMPO-Based Catholyte for High-Energy Density Nonaqueous Redox Flow Batteries. *Adv. Mater.* **2014**, *26*, 7649-7653.
40. Janoschka, T.; Martin, N.; Hager, M. D.; Schubert, U. S., An Aqueous Redox-Flow Battery with High Capacity and Power: The TEMPTMA/MV System. *Angew. Chem. Int. Ed.* **2016**, *55*, 14427-14430.
41. Ding, Y.; Zhao, Y.; Yu, G., A Membrane-Free Ferrocene-Based High-Rate Semiliquid Battery. *Nano Lett.* **2015**, *15*, 4108-4113.
42. Wei, X.; Cosimbescu, L.; Xu, W.; Hu, J. Z.; Vijayakumar, M.; Feng, J.; Hu, M. Y.; Deng, X.; Xiao, J.; Liu, J., Towards High-Performance Nonaqueous Redox Flow Electrolyte Via Ionic Modification of Active Species. *Adv. Energy Mater.* **2015**, *5*, 1400678.
43. Ding, Y.; Zhao, Y.; Li, Y.; Goodenough, J. B.; Yu, G., A High-Performance All-Metallocene-Based, Non-Aqueous Redox Flow Battery. *Energy Environ. Sci.* **2017**, *10*, 491-497.
44. Gong, K.; Fang, Q.; Gu, S.; Li, S. F. Y.; Yan, Y., Nonaqueous Redox-Flow Batteries: Organic Solvents, Supporting Electrolytes, and Redox Pairs. *Energy Environ. Sci.* **2015**, *8*, 3515-3530.
45. Singh, P., Application of Non-Aqueous Solvents to Batteries. *J. Power Sources* **1984**, *11*, 135-142.
46. Matsuda, Y.; Tanaka, K.; Okada, M.; Takasu, Y.; Morita, M.; Matsumura-Inoue, T., A Rechargeable Redox Battery Utilizing Ruthenium Complexes with Non-Aqueous Organic Electrolyte. *J. Appl. Electrochem.* **1988**, *18*, 909-914.
47. Liu, Q.; Shinkle, A. A.; Li, Y.; Monroe, C. W.; Thompson, L. T.; Sleightholme, A. E., Non-Aqueous Chromium Acetylacetonate Electrolyte for Redox Flow Batteries. *Electrochem. Commun.* **2010**, *12*, 1634-1637.

48. Guo, X.; Zhang, L.; Ding, Y.; Goodenough, J. B.; Yu, G., Room-Temperature Liquid Metal and Alloy Systems for Energy Storage Applications. *Energy Environ. Sci.* **2019**, *12*, 2609-2615.
49. Zhao, Y.; Ding, Y.; Li, Y.; Peng, L.; Byon, H. R.; Goodenough, J. B.; Yu, G., A Chemistry and Material Perspective on Lithium Redox Flow Batteries Towards High-Density Electrical Energy Storage. *Chem. Soc. Rev.* **2015**, *44*, 7968-7996.
50. Winsberg, J.; Stolze, C.; Schwenke, A.; Muench, S.; Hager, M. D.; Schubert, U. S., Aqueous 2, 2, 6, 6-Tetramethylpiperidine-N-Oxyl Catholytes for a High-Capacity and High Current Density Oxygen-Insensitive Hybrid-Flow Battery. *ACS Energy Lett.* **2017**, *2*, 411-416.
51. Wang, W.; Xu, W.; Cosimbescu, L.; Choi, D.; Li, L.; Yang, Z., Anthraquinone with Tailored Structure for a Nonaqueous Metal–Organic Redox Flow Battery. *Chem. Commun.* **2012**, *48*, 6669-6671.
52. Chen, R., Toward High-Voltage, Energy-Dense, and Durable Aqueous Organic Redox Flow Batteries: Role of the Supporting Electrolytes. *ChemElectroChem* **2019**, *6*, 603-612.
53. Orita, A.; Verde, M. G.; Sakai, M.; Meng, Y. S., A Biomimetic Redox Flow Battery Based on Flavin Mononucleotide. *Nat. Commun.* **2016**, *7*, 13230.
54. Li, Z.; Li, S.; Liu, S.; Huang, K.; Fang, D.; Wang, F.; Peng, S., Electrochemical Properties of an All-Organic Redox Flow Battery Using 2, 2, 6, 6-Tetramethyl-1-Piperidinyloxy and N-Methylphthalimide. *Electrochem. Sol. Stat. Lett.* **2011**, *14*, A171.
55. Kwon, G.; Lee, S.; Hwang, J.; Shim, H.-S.; Lee, B.; Lee, M. H.; Ko, Y.; Jung, S.-K.; Ku, K.; Hong, J., Multi-Redox Molecule for High-Energy Redox Flow Batteries. *Joule* **2018**, *2*, 1771-1782.
56. Wei, X.; Xu, W.; Huang, J.; Zhang, L.; Walter, E.; Lawrence, C.; Vijayakumar, M.; Henderson, W. A.; Liu, T.; Cosimbescu, L., Radical Compatibility with Nonaqueous Electrolytes and Its Impact on an All-Organic Redox Flow Battery. *Angew. Chem. Int. Ed.* **2015**, *54*, 8684-8687.
57. Wang, N.; Kähkönen, A.; Damlin, P.; Ääritalo, T.; Kankare, J.; Kvarnström, C., Electrochemical Synthesis and Characterization of Branched Viologen Derivatives. *Electrochim. Acta* **2015**, *154*, 361-369.
58. Duduta, M.; Ho, B.; Wood, V. C.; Limthongkul, P.; Brunini, V. E.; Carter, W. C.; Chiang, Y. M., Semi-Solid Lithium Rechargeable Flow Battery. *Adv. Energy Mater.* **2011**, *1*, 511-516.

59. Zhang, L.; Zhang, C.; Ding, Y.; Ramirez-Meyers, K.; Yu, G., A Low-Cost and High-Energy Hybrid Iron-Aluminum Liquid Battery Achieved by Deep Eutectic Solvents. *Joule* **2017**, *1*, 623-633.
60. Brushett, F. R.; Vaughey, J. T.; Jansen, A. N., An All-Organic Non-Aqueous Lithium-Ion Redox Flow Battery. *Adv. Energy Mater.* **2012**, *2*, 1390-1396.
61. Ge, S.; Wang, C.-Y., In Situ Imaging of Liquid Water and Ice Formation in an Operating PEFC During Cold Start. *Electrochem. Sol. Stat. Lett.* **2006**, *9*, A499-A503.
62. Li, L.; Kim, S.; Wang, W.; Vijayakumar, M.; Nie, Z.; Chen, B.; Zhang, J.; Xia, G.; Hu, J.; Graff, G., A Stable Vanadium Redox-Flow Battery with High Energy Density for Large-Scale Energy Storage. *Adv. Energy Mater.* **2011**, *1*, 394-400.
63. Rosenfeld, D.; Woodley, W. L., Deep Convective Clouds with Sustained Supercooled Liquid Water down to -37.5 °C. *Nature* **2000**, *405*, 440-442.
64. Bodnar, R., Revised Equation and Table for Determining the Freezing Point Depression of H<sub>2</sub>O-NaCl Solutions. *Geochim. Cosmochim. Acta* **1993**, *57*, 683-684.
65. Mousa, A.; Skyllas-Kazacos, M., Effect of Additives on the Low-Temperature Stability of Vanadium Redox Flow Battery Negative Half-Cell Electrolyte. *ChemElectroChem* **2015**, *2*, 1742-1751.
66. Kausar, N.; Mousa, A.; Skyllas-Kazacos, M., The Effect of Additives on the High-Temperature Stability of the Vanadium Redox Flow Battery Positive Electrolytes. *ChemElectroChem* **2016**, *3*, 276-282.
67. Zhang, J.; Li, L.; Nie, Z.; Chen, B.; Vijayakumar, M.; Kim, S.; Wang, W.; Schwenzer, B.; Liu, J.; Yang, Z., Effects of Additives on the Stability of Electrolytes for All-Vanadium Redox Flow Batteries. *J. Appl. Electrochem.* **2011**, *41*, 1215-1221.
68. Ohtake, T., Freezing Points of H<sub>2</sub>SO<sub>4</sub> Aqueous Solutions and Formation of Stratospheric Ice Clouds. *Tellus B* **1993**, *45*, 138-144.
69. Zhao, Y.; Liu, L.; Qiu, X.; Xi, J., Revealing Sulfuric Acid Concentration Impact on Comprehensive Performance of Vanadium Electrolytes and Flow Batteries. *Electrochim. Acta* **2019**, *303*, 21-31.
70. Dong, X.; Guo, Z.; Guo, Z.; Wang, Y.; Xia, Y., Organic Batteries Operated at -70 °C. *Joule* **2018**, *2*, 902-913.

71. Dong, X.; Lin, Y.; Li, P.; Ma, Y.; Huang, J.; Bin, D.; Wang, Y.; Qi, Y.; Xia, Y., High-Energy Rechargeable Metallic Lithium Battery at  $-70$  °C Enabled by a Cosolvent Electrolyte. *Angew. Chem. Int. Ed.* **2019**, *131*, 5679-5683.
72. Ma, T.; Pan, Z.; Miao, L.; Chen, C.; Han, M.; Shang, Z.; Chen, J., Porphyrin-Based Symmetric Redox-Flow Batteries Towards Cold-Climate Energy Storage. *Angew. Chem. Int. Ed.* **2018**, *130*, 3212-3216.
73. Takechi, K.; Kato, Y.; Hase, Y., A Highly Concentrated Catholyte Based on a Solvate Ionic Liquid for Rechargeable Flow Batteries. *Adv. Mater.* **2015**, *27*, 2501-2506.
74. Smith, E. L.; Abbott, A. P.; Ryder, K. S., Deep Eutectic Solvents (DESS) and Their Applications. *Chem. Rev.* **2014**, *114*, 11060-11082.
75. Zhang, C.; Niu, Z.; Ding, Y.; Zhang, L.; Zhou, Y.; Guo, X.; Zhang, X.; Zhao, Y.; Yu, G., Highly Concentrated Phthalimide-Based Anolytes for Organic Redox Flow Batteries with Enhanced Reversibility. *Chem* **2018**, *4*, 2814-2825.
76. Amarasekara, A. S., Acidic Ionic Liquids. *Chem. Rev.* **2016**, *116*, 6133-6183.
77. Zhang, Z.; Song, J.; Han, B., Catalytic Transformation of Lignocellulose into Chemicals and Fuel Products in Ionic Liquids. *Chem. Rev.* **2017**, *117*, 6834-6880.
78. Zhang, J.; Wu, J.; Yu, J.; Zhang, X.; He, J.; Zhang, J., Application of Ionic Liquids for Dissolving Cellulose and Fabricating Cellulose-Based Materials: State of the Art and Future Trends. *Mater. Chem. Front.* **2017**, *1*, 1273-1290.
79. Galiński, M.; Lewandowski, A.; Stępnik, I., Ionic Liquids as Electrolytes. *Electrochim. Acta* **2006**, *51*, 5567-5580.
80. Watanabe, M.; Thomas, M. L.; Zhang, S.; Ueno, K.; Yasuda, T.; Dokko, K., Application of Ionic Liquids to Energy Storage and Conversion Materials and Devices. *Chem. Rev.* **2017**, *117*, 7190-7239.
81. Ohno, H., *Electrochemical Aspects of Ionic Liquids*. John Wiley & Sons, Inc. **2005**.
82. Armand, M.; Endres, F.; MacFarlane, D. R.; Ohno, H.; Scrosati, B., Ionic-Liquid Materials for the Electrochemical Challenges of the Future. *Nat. Mater.* **2009**, *8*, 621-629.
83. Tatlisu, A.; Huang, Z.; Chen, R., High-Voltage and Low-Temperature Aqueous Supercapacitor Enabled by “Water-in-Imidazolium Chloride” Electrolytes. *ChemSusChem* **2018**, *11*, 3899-3904.
84. Li, M.; Wang, C.; Chen, Z.; Xu, K.; Lu, J., New Concepts in Electrolytes. *Chem. Rev.* **2020**. doi.org/10.1021/acs.chemrev.9b00531.

85. Welton, T., Ionic Liquids: A Brief History. *Biophys. Rev.* **2018**, *10*, 691-706.
86. Chakrabarti, M. H.; Mjalli, F. S.; AlNashef, I. M.; Hashim, M. A.; Hussain, M. A.; Bahadori, L.; Low, C. T. J., Prospects of Applying Ionic Liquids and Deep Eutectic Solvents for Renewable Energy Storage by Means of Redox Flow Batteries. *Renew. Sust. Energ. Rev.* **2014**, *30*, 254-270.
87. Mourad, E.; Coustan, L.; Lannelongue, P.; Zigah, D.; Mehdi, A.; Vioux, A.; Freunberger, S. A.; Favier, F.; Fontaine, O., Biredox Ionic Liquids with Solid-Like Redox Density in the Liquid State for High-Energy Supercapacitors. *Nat. Mater.* **2009**, *16*, 446-453.
88. Hernández, G.; Işik, M.; Mantione, D.; Pendashteh, A.; Navalpotro, P.; Shanmukaraj, D.; Marcilla, R.; Mecerreyes, D., Redox-Active Poly (Ionic Liquid) S as Active Materials for Energy Storage Applications. *J. Mater. Chem. A* **2017**, *5*, 16231-16240.
89. Chen, R.; Hempelmann, R., Ionic Liquid-Mediated Aqueous Redox Flow Batteries for High Voltage Applications. *Electrochem. Commun.* **2016**, *70*, 56-59.
90. MacFarlane, D. R.; Tachikawa, N.; Forsyth, M.; Pringle, J. M.; Howlett, P. C.; Elliott, G. D.; Davis, J. H.; Watanabe, M.; Simon, P.; Angell, C. A., Energy Applications of Ionic Liquids. *Energy Environ. Sci.* **2014**, *7*, 232-250.
91. Navalpotro, P.; Sierra, N.; Trujillo, C.; Montes, I.; Palma, J.; Marcilla, R., Exploring the Versatility of Membrane-Free Battery Concept Using Different Combinations of Immiscible Redox Electrolytes. *ACS Appl. Mater. Interfaces* **2018**, *10*, 41246-41256.
92. Navalpotro, P.; Neves, C. M.; Palma, J.; Freire, M. G.; Coutinho, J. A.; Marcilla, R., Pioneering Use of Ionic Liquid-Based Aqueous Biphasic Systems as Membrane-Free Batteries. *Adv. Sci.* **2018**, *5*, 1800576.
93. Navalpotro, P.; Palma, J.; Anderson, M.; Marcilla, R., A Membrane-Free Redox Flow Battery with Two Immiscible Redox Electrolytes. *Angew. Chem. Int. Ed.* **2017**, *129*, 12634-12639.
94. Xu, P.; Xie, C.; Wang, C.; Lai, Q.; Wang, W.; Zhang, H.; Li, X., A Membrane-Free Interfacial Battery with High Energy Density. *Chem. Commun.* **2018**, *54*, 11626-11629.
95. Mantz, R. A.; Trulove, P.; *Viscosity and Density of Ionic Liquids, Ionic Liquids in Synthesis*, John Wiley & Sons, Inc., **2002**.
96. Wasserscheid, P.; Welton, T., *Ionic Liquids in Synthesis, 2nd ed.*; John Wiley &

- Sons, Inc.* **2008**.
97. Suo, L.; Borodin, O.; Gao, T.; Olguin, M.; Ho, J.; Fan, X.; Luo, C.; Wang, C.; Xu, K., "Water-in-Salt" Electrolyte Enables High-Voltage Aqueous Lithium-Ion Chemistries. *Science* **2015**, *350*, 938-943.
  98. Kühnel, R.-S.; Reber, D.; Battaglia, C., A High-Voltage Aqueous Electrolyte for Sodium-Ion Batteries. *ACS Energy Lett.* **2017**, *2*, 2005-2006.
  99. Suo, L.; Borodin, O.; Sun, W.; Fan, X.; Yang, C.; Wang, F.; Gao, T.; Ma, Z.; Schroeder, M.; von Cresce, A., Advanced High-Voltage Aqueous Lithium-Ion Battery Enabled by "Water-in-Bisalt" Electrolyte. *Angew. Chem. Int. Ed.* **2016**, *55*, 7136-7141.
  100. Hardacre, C.; Holbrey, J. D.; Nieuwenhuyzen, M.; Youngs, T. G., Structure and Solvation in Ionic Liquids. *Acc. Chem. Res.* **2007**, *40*, 1146-1155.
  101. Fredlake, C. P.; Crosthwaite, J. M.; Hert, D. G.; Aki, S. N.; Brennecke, J. F., Thermophysical Properties of Imidazolium-Based Ionic Liquids. *J. Chem. Eng. Data* **2004**, *49*, 954-964.
  102. König, A.; Stepanski, M.; Kuszlik, A.; Keil, P.; Weller, C., Ultra-Purification of Ionic Liquids by Melt Crystallization. *Chem. Eng. Res. Des.* **2008**, *86*, 775-780.
  103. Bard, A. J.; Faulkner, L. R.; Leddy, J.; Zoski, C. G., Electrochemical Methods: Fundamentals and Applications, *2nd ed.*; John Wiley & Sons, New York, **2001**, 2.
  104. Krumrey, M., Small Angle X-Ray Scattering (SAXS). In Characterization of Nanoparticles, *Elsevier*, **2020**, 173-183.
  105. Brustolon, M.; Giamello, E., Electron Paramagnetic Resonance: A Practitioners Toolkit, *John Wiley & Sons*, **2009**.
  106. Lund, A.; Shiotani, M.; Shimada, S., Principles and Applications of ESR Spectroscopy, *Springer Science & Business Media*, **2011**.
  107. Mei, B.-A.; Lau, J.; Lin, T.; Tolbert, S. H.; Dunn, B. S.; Pilon, L., Physical Interpretations of Electrochemical Impedance Spectroscopy of Redox Active Electrodes for Electrical Energy Storage. *J. Phys. Chem. C* **2018**, *122*, 24499-24511.
  108. Jacquemin, J.; Husson, P.; Padua, A. A.; Majer, V., Density and Viscosity of Several Pure and Water-Saturated Ionic Liquids. *Green Chem.* **2006**, *8*, 172-180.
  109. Fannin Jr, A. A.; Floreani, D. A.; King, L. A.; Landers, J. S.; Piersma, B. J.; Stech, D. J.; Vaughn, R. L.; Wilkes, J. S.; Williams, J. L., Properties of 1, 3-Dialkylimidazolium Chloride-Aluminum Chloride Ionic Liquids. 2. Phase

- Transitions, Densities, Electrical Conductivities, and Viscosities. *J. Phys. Chem.* **1984**, *88*, 2614-2621.
110. Huddleston, J. G.; Visser, A. E.; Reichert, W. M.; Willauer, H. D.; Broker, G. A.; Rogers, R. D., Characterization and Comparison of Hydrophilic and Hydrophobic Room Temperature Ionic Liquids Incorporating the Imidazolium Cation. *Green Chem.* **2001**, *3*, 156-164.
111. Stoppa, A.; Hunger, J.; Buchner, R., Conductivities of Binary Mixtures of Ionic Liquids with Polar Solvents. *J. Chem. Eng. Data* **2009**, *54*, 472-479.
112. Abramczyk, H.; Brożek-Płuska, B.; Kurczewski, K.; Kurczewska, M.; Szymczyk, I.; Krzyczmonik, P.; Błaszczak, T.; Scholl, H.; Czajkowski, W., Femtosecond Transient Absorption, Raman, and Electrochemistry Studies of Tetrasulfonated Copper Phthalocyanine in Water Solutions. *J. Phys. Chem. A* **2006**, *110*, 8627-8636.
113. Rauber, D.; Zhang, P.; Huch, V.; Kraus, T.; Hempelmann, R., Lamellar Structures in Fluorinated Phosphonium Ionic Liquids: The Roles of Fluorination and Chain Length. *Phys. Chem. Chem. Phys.* **2017**, *19*, 27251-27258.
114. Wang, Y.; Dai, X.; Jiang, W.; Wu, F.; Xie, A., The Hybrid of SnO<sub>2</sub> Nanoparticle and Polypyrrole Aerogel: An Excellent Electromagnetic Wave Absorbing Materials. *Mater. Res. Expr.* **2016**, *3*, 075023.
115. El-Nahass, M.; Farag, A.; El-Rahman, K. A.; Darwish, A., Dispersion Studies and Electronic Transitions in Nickel Phthalocyanine Thin Films. *Opt. Laser Technol.* **2005**, *37*, 513-523.
116. Kobayashi, Y.; Kitazawa, Y.; Hashimoto, K.; Ueki, T.; Kokubo, H.; Watanabe, M., Thermosensitive Phase Separation Behavior of Poly (Benzyl Methacrylate)/Solvate Ionic Liquid Solutions. *Langmuir* **2017**, *33*, 14105-14114.
117. Aguilera, L.; Xiong, S.; Scheers, J.; Matic, A., A Structural Study of LiTFSI–Tetraglyme Mixtures: From Diluted Solutions to Solvated Ionic Liquids. *J. Mol. Liq.* **2015**, *210*, 238-242.
118. Araque, J. C.; Hettige, J. J.; Margulis, C. J., Modern Room Temperature Ionic Liquids, a Simple Guide to Understanding Their Structure and How It May Relate to Dynamics. *J. Phys. Chem. B* **2015**, *119*, 12727-12740.
119. Ramanujapuram, A.; Yushin, G., Understanding the Exceptional Performance of Lithium-Ion Battery Cathodes in Aqueous Electrolytes at Subzero Temperatures. *Adv. Energy Mater.* **2018**, *8*, 1802624.

120. Smart, M.; Ratnakumar, B.; Surampudi, S., Electrolytes for Low-Temperature Lithium Batteries Based on Ternary Mixtures of Aliphatic Carbonates. *J. Electrochem. Soc.* **1999**, *146*, 486-492.
121. Iwama, E.; Taberna, P.-L.; Azais, P.; Brégeon, L.; Simon, P., Characterization of Commercial Supercapacitors for Low Temperature Applications. *J. Power Sources* **2012**, *219*, 235-239.
122. Wang, C.-Y.; Zhang, G.; Ge, S.; Xu, T.; Ji, Y.; Yang, X.-G.; Leng, Y., Lithium-Ion Battery Structure That Self-Heats at Low Temperatures. *Nature* **2016**, *529*, 515.
123. Aguilera, L.; Scheers, J.; Matic, A., Enhanced Low-Temperature Ionic Conductivity via Different Li<sup>+</sup> Solvated Clusters in Organic Solvent/Ionic Liquid Mixed Electrolytes. *Phys. Chem. Chem. Phys.* **2016**, *18*, 25458-25464.
124. Kamau, G. N.; Rusling, J. F., Enhanced Rates of Organic Dehalogenations in a Microemulsion Using Adsorbed Metal Phthalocyanines on Electrodes. *Langmuir* **1996**, *12*, 2645-2649.
125. Chang, Z.; Henkensmeier, D.; Chen, R., One-Step Cationic Grafting of 4-Hydroxy-TEMPO and Its Application in a Hybrid Redox Flow Battery with a Crosslinked PBI Membrane. *ChemSusChem* **2017**, *10*, 3193-3197.
126. Xie, C.; Duan, Y.; Xu, W.; Zhang, H.; Li, X., A Low-Cost Neutral Zinc–Iron Flow Battery with High Energy Density for Stationary Energy Storage. *Angew. Chem. Int. Ed.* **2017**, *56*, 14953-14957.
127. Chen, R.; Henkensmeier, D.; Kim, S.; Yoon, S. J.; Zinkevich, T.; Indris, S., Improved All-Vanadium Redox Flow Batteries Using Catholyte Additive and a Cross-Linked Methylated Polybenzimidazole Membrane. *ACS Appl. Energy Mater.* **2018**, *1*, 6047-6055.
128. Liao, M.-S.; Scheiner, S., Electronic Structure and Bonding in Metal Phthalocyanines, Metal= Fe, Co, Ni, Cu, Zn, Mg. *J. Chem. Phys.* **2001**, *114*, 9780-9791.
129. Huang, Z.; Zhang, P.; Gao, X.; Henkensmeier, D.; Passerini, S.; Chen, R., Unlocking Simultaneously the Temperature and Electrochemical Windows of Aqueous Phthalocyanine Electrolytes. *ACS Appl. Energy Mater.* **2019**, *2*, 3773-3779.
130. Liu, W.; Liu, Y.; Zhang, H.; Xie, C.; Shi, L.; Zhou, Y.-G.; Li, X., A Highly Stable Neutral Viologen/Bromine Aqueous Flow Battery with High Energy and Power Density. *Chem. Commun.* **2019**, *55*, 4801-4804.
131. DeBruler, C.; Hu, B.; Moss, J.; Liu, X.; Luo, J.; Sun, Y.; Liu, T. L., Designer Two-

- Electron Storage Viologen Anolyte Materials for Neutral Aqueous Organic Redox Flow Batteries. *Chem* **2017**, *3*, 961-978.
132. Jin, S.; Jing, Y.; Kwabi, D. G.; Ji, Y.; Tong, L.; De Porcellinis, D.; Goulet, M.-A.; Pollack, D. A.; Gordon, R. G.; Aziz, M. J., A Water-Miscible Quinone Flow Battery with High Volumetric Capacity and Energy Density. *ACS Energy Lett.* **2019**, *4*, 1342-1348.
133. Eugene S. Beh, D. D. P., Rebecca L. Gracia, Kay T. Xia, Roy G. Gordon, Michael J. Aziz, A Neutral pH Aqueous Organic–Organometallic Redox Flow Battery with Extremely High Capacity Retention. *ACS Energy Lett.* **2017**, *2*, 639-644.
134. Luo, J.; Hu, B.; Hu, M.; Zhao, Y.; Liu, T. L., Status and Prospects of Organic Redox Flow Batteries Towards Sustainable Energy Storage. *ACS Energy Lett.* **2019**, *4*, 2220-2240.
135. Goulet, M.-A.; Tong, L.; Pollack, D. A.; Tabor, D. P.; Kwan, E. E.; Aspuru-Guzik, A.; Gordon, R. G.; Aziz, M. J., Extending the Lifetime of Organic Flow Batteries via Redox State Management. *J. Am. Chem. Soc.* **2019**, *141*, 8014-8019.
136. Gerhardt, M. R.; Tong, L.; Gómez-Bombarelli, R.; Chen, Q.; Marshak, M. P.; Galvin, C. J.; Aspuru-Guzik, A.; Gordon, R. G.; Aziz, M. J., Anthraquinone Derivatives in Aqueous Flow Batteries. *Adv. Energy Mater.* **2017**, *7*, 1601488.
137. Yang, Z.; Tong, L.; Tabor, D. P.; Beh, E. S.; Goulet, M. A.; De Porcellinis, D.; Aspuru-Guzik, A.; Gordon, R. G.; Aziz, M. J., Alkaline Benzoquinone Aqueous Flow Battery for Large-Scale Storage of Electrical Energy. *Adv. Energy Mater.* **2018**, *8*, 1702056.
138. Zhang, C.; Niu, Z.; Peng, S.; Ding, Y.; Zhang, L.; Guo, X.; Zhao, Y.; Yu, G., Phenothiazine-Based Organic Catholyte for High-Capacity and Long-Life Aqueous Redox Flow Batteries. *Adv. Mater.* **2019**, *31*, 1901052.
139. Ciriano, M. V.; Korth, H.-G.; Van Scheppingen, W. B.; Mulder, P., Thermal Stability of 2, 2, 6, 6-Tetramethylpiperidine-1-Oxyl (TEMPO) and Related N-Alkoxyamines. *J. Am. Chem. Soc.* **1999**, *121*, 6375-6381.
140. Geraskina, M. R.; Dutton, A. S.; Juetten, M. J.; Wood, S. A.; Winter, A. H., The Viologen Cation Radical Pimer: A Case of Dispersion-Driven Bonding. *Angew. Chem. Int. Ed.* **2017**, *129*, 9563-9567.
141. Clarke, D. E.; Olesińska, M.; Mönch, T.; Schoenaers, B.; Stesmans, A.; Scherman, O. A., Aryl-Viologen Pentapeptide Self-Assembled Conductive Nanofibers. *Chem. Commun.* **2019**, *55*, 7354-7357.

142. Buck, A. T.; Paletta, J. T.; Khindurangala, S. A.; Beck, C. L.; Winter, A. H., A Noncovalently Reversible Paramagnetic Switch in Water. *J. Am. Chem. Soc.* **2013**, *135*, 10594-10597.
143. Hu, B.; Tang, Y.; Luo, J.; Grove, G.; Guo, Y.; Liu, T. L., Improved Radical Stability of Viologen Anolytes in Aqueous Organic Redox Flow Batteries. *Chem. Commun.* **2018**, *54*, 6871-6874.
144. DeBruler, C.; Hu, B.; Moss, J.; Luo, J.; Liu, T. L., A Sulfonate-Functionalized Viologen Enabling Neutral Cation Exchange, Aqueous Organic Redox Flow Batteries toward Renewable Energy Storage. *ACS Energy Lett.* **2018**, *3*, 663-668.
145. Luo, J.; Hu, B.; Debruler, C.; Liu, T. L., A  $\pi$ -Conjugation Extended Viologen as a Two-Electron Storage Anolyte for Total Organic Aqueous Redox Flow Batteries. *Angew. Chem. Int. Ed.* **2018**, *57*, 231-235.
146. Orita, A.; Verde, M.; Sakai, M.; Meng, Y., The Impact of pH on Side Reactions for Aqueous Redox Flow Batteries Based on Nitroxyl Radical Compounds. *J. Power Sources* **2016**, *321*, 126-134.
147. Chang, Z.; Henkensmeier, D.; Chen, R., Shifting Redox Potential of Nitroxyl Radical by Introducing an Imidazolium Substituent and Its Use in Aqueous Flow Batteries. *J. Power Sources* **2019**, *418*, 11-16.
148. Zhang, J.; Yang, Z.; Shkrob, I. A.; Assary, R. S.; Tung, S. o.; Silcox, B.; Duan, W.; Zhang, J.; Su, C. C.; Hu, B., Annulated Dialkoxybenzenes as Catholyte Materials for Non-Aqueous Redox Flow Batteries: Achieving High Chemical Stability through Bicyclic Substitution. *Adv. Energy Mater.* **2017**, *7*, 1701272.
149. Huang, J.; Su, L.; Kowalski, J. A.; Barton, J. L.; Ferrandon, M.; Burrell, A. K.; Brushett, F. R.; Zhang, L., A Subtractive Approach to Molecular Engineering of Dimethoxybenzene-Based Redox Materials for Non-Aqueous Flow Batteries. *J. Mater. Chem. A* **2015**, *3*, 14971-14976.
150. Luo, J.; Hu, B.; Debruler, C.; Bi, Y.; Zhao, Y.; Yuan, B.; Hu, M.; Wu, W.; Liu, T. L., Unprecedented Capacity and Stability of Ammonium Ferrocyanide Catholyte in pH Neutral Aqueous Redox Flow Batteries. *Joule* **2018**, *3*, 149-163.
151. Liu, Y.; Goulet, M.-A.; Tong, L.; Liu, Y.; Ji, Y.; Wu, L.; Gordon, R. G.; Aziz, M. J.; Yang, Z.; Xu, T., A Long Lifetime All-Organic Aqueous Flow Battery Utilizing TMAP-TEMPO Radical. *Chem* **2019**, *5*, 1861-1870.
152. Er, S.; Suh, C.; Marshak, M. P.; Aspuru-Guzik, A., Computational Design of Molecules for an All-Quinone Redox Flow Battery. *Chem. Sci.* **2015**, *6*, 885-893.
153. Wei, X.; Duan, W.; Huang, J.; Zhang, L.; Li, B.; Reed, D.; Xu, W.; Sprenkle, V.;

- Wang, W., A High-Current, Stable Nonaqueous Organic Redox Flow Battery. *ACS Energy Lett.* **2016**, *1*, 705-711.
154. Ding, Y.; Li, Y.; Yu, G., Exploring Bio-Inspired Quinone-Based Organic Redox Flow Batteries: A Combined Experimental and Computational Study. *Chem* **2016**, *1*, 790-801.
155. Hu, B.; Luo, J.; Hu, M.; Yuan, B.; Liu, T. L., A pH-Neutral, Metal-Free Aqueous Organic Redox Flow Battery Employing an Ammonium Anthraquinone Anolyte. *Angew. Chem. Int. Ed.* **2019**, *58*, 16629-16636.
156. Kwabi, D. G.; Lin, K.; Ji, Y.; Kerr, E. F.; Goulet, M.-A.; De Porcellinis, D.; Tabor, D. P.; Pollack, D. A.; Aspuru-Guzik, A.; Gordon, R. G., Alkaline Quinone Flow Battery with Long Lifetime at pH 12. *Joule* **2018**, *2*, 1894-1906.
157. Hooper-Burkhardt, L.; Krishnamoorthy, S.; Yang, B.; Murali, A.; Nirmalchandar, A.; Prakash, G. S.; Narayanan, S., A New Michael-Reaction-Resistant Benzoquinone for Aqueous Organic Redox Flow Batteries. *J. Electrochem. Soc.* **2017**, *164*, A600-A607.
158. Yang, B.; Hooper-Burkhardt, L.; Krishnamoorthy, S.; Murali, A.; Prakash, G. S.; Narayanan, S., High-Performance Aqueous Organic Flow Battery with Quinone-Based Redox Couples at Both Electrodes. *J. Electrochem. Soc.* **2016**, *163*, A1442-A1449.
159. Yang, B.; Hooper-Burkhardt, L.; Wang, F.; Prakash, G. S.; Narayanan, S., An Inexpensive Aqueous Flow Battery for Large-Scale Electrical Energy Storage Based on Water-Soluble Organic Redox Couples. *J. Electrochem. Soc.* **2014**, *161*, A1371-A1380.
160. Khataee, A.; Wedege, K.; Dražević, E.; Bonten, A., Differential pH as a Method for Increasing Cell Potential in Organic Aqueous Flow Batteries. *J. Mater. Chem. A* **2017**, *5*, 21875-21882.
161. Huang, Z.; Kay, C. W.; Kuttich, B.; Rauber, D.; Kraus, T.; Li, H.; Kim, S.; Chen, R., An "Interaction-Mediating" Strategy Towards Enhanced Solubility and Redox Properties of Organics for Aqueous Flow Batteries. *Nano Energy* **2020**, *69*, 104464.
162. Guin, P. S.; Das, S.; Mandal, P., Electrochemical Reduction of Quinones in Different Media: A Review. *Inter. J. Electrochem.* **2011**.
163. Quan, M.; Sanchez, D.; Wasylkiw, M. F.; Smith, D. K., Voltammetry of Quinones in Unbuffered Aqueous Solution: Reassessing the Roles of Proton Transfer and Hydrogen Bonding in the Aqueous Electrochemistry of Quinones. *J. Am. Chem.*

- Soc.* **2007**, *129*, 12847-12856.
164. Li, Q.; Batchelor-McAuley, C.; Lawrence, N. S.; Hartshorne, R. S.; Compton, R. G., Electrolyte Tuning of Electrode Potentials: The One Electron vs. Two Electron Reduction of Anthraquinone-2-Sulfonate in Aqueous Media. *Chem. Commun.* **2011**, *47*, 11426-11428.
165. Kim, Y.-R.; Kim, R. S.; Kang, S. K.; Choi, M. G.; Kim, H. Y.; Cho, D.; Lee, J. Y.; Chang, S.-K.; Chung, T. D., Modulation of Quinone PCET Reaction by  $\text{Ca}^{2+}$  Ion Captured by Calix [4] Quinone in Water. *J. Am. Chem. Soc.* **2013**, *135*, 18957-18967.
166. Wedege, K.; Dražević, E.; Konya, D.; Bonten, A., Organic Redox Species in Aqueous Flow Batteries: Redox Potentials, Chemical Stability and Solubility. *Sci. Rep.* **2016**, *6*, 39101.
167. Nicholson, R. S., Theory and Application of Cyclic Voltammetry for Measurement of Electrode Reaction Kinetics. *Anal. Chem.* **1965**, *37*, 1351-1355.
168. Ji, Y.; Goulet, M. A.; Pollack, D. A.; Kwabi, D. G.; Jin, S.; De Porcellinis, D.; Kerr, E. F.; Gordon, R. G.; Aziz, M. J., A Phosphonate-Functionalized Quinone Redox Flow Battery at near-Neutral pH with Record Capacity Retention Rate. *Adv. Energy Mater.* **2019**, *9*, 1900039.
169. Yamamura, T.; Watanabe, N.; Yano, T.; Shiokawa, Y., Electron-Transfer Kinetics of  $\text{Np}^{3+}/\text{Np}^{4+}$ ,  $\text{NpO}^{2+}/\text{NpO}_2^{2+}$ ,  $\text{V}^{2+}/\text{V}^{3+}$ , and  $\text{VO}^{2+}/\text{VO}_2^+$  at Carbon Electrodes. *J. Electrochem. Soc.* **2005**, *152*, A830-A836.